A measurement of the cross sections for $e^+e^- \to e^+e^-$ and $e^+e^- \to e^+e^-\gamma$ at high energy.

John Illingworth, Wolfson College, Oxford

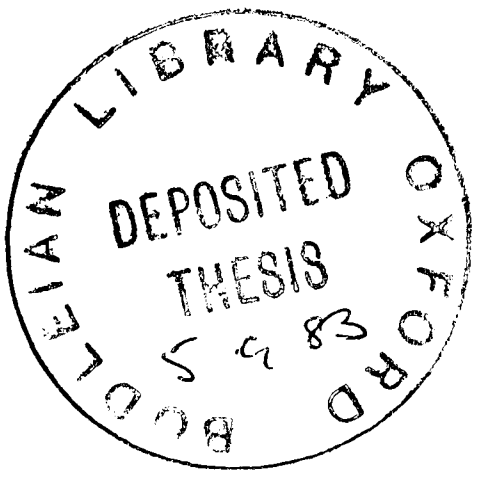

A thesis submitted for the degree of Doctor of Philosophy
at the University of Oxford.

April 1983

A measurement of the cross sections for $e^+e^- \to e^+e^-$ and $e^+e^- \to e^+e^-\gamma$ at high energy

John Illingworth

Wolfson College

Thesis submitted for the degree of Doctor of Philosophy in the University of Oxford.

April 1983

ABSTRACT

Data from the TASSO experiment at the PETRA e^+e^- storage ring has been analysed to investigate the cross section for the QED reactions

(a) $e^+ + e^- \to e^+ + e^-$ Bhabha scattering

and

(b) $e^+ + e^- \to e^+ + e^- + \gamma$

Details of the TASSO detector and a detailed description of an array of lead/scintillator sandwich electromagnetic shower counters, used in the analysis of reaction (b), is given.

For beam energies greater than 10 Gev the ratio of the measured total Bhabha scattering cross section to the QED prediction was found to be 0.949 ±0.013 (statistical) ±0.06(systematic). It was shown, by fitting the measured angular cross section, that QED is a point like theory down to distances of 2×10^{-18}m. The predictions of models of electroweak unification have been compared to the data and parameters of these theories have been found to agree with, but not strongly constrain, these theories. Significant limits are placed on electroweak theories which predict more than 1 neutral weak gauge boson.

The number of events with two charged tracks and one photon has been measured and compared to the QED cross section predictions for reaction (b). 21 such events were selected and this agrees well with the predicted number of 25±2.6. The agreement of these numbers has been used to determine that the mass of an excited electron state, e^*, (which would contribute events to this experimental signature by its radiative decay) must be greater than 34 Gev (95% confidence limit), if it has normal couplings.

To my parents for all their hard work and love.

Acknowledgements

The work of my research degree has been enriched by the advice and company of many talented people.

I would like to thank my supervisor Dr Graeme Salmon. He has listened patiently and carefully and offered guidance and criticism which was always well considered and constructive.

A great debt of thanks is owed to my fellow collaborators Roger Cashmore, Robin Devenish and Mike Bowler. They have provided many useful discussions and much practical assistence.

My meagre knowledge of computers and programming has been helped considerably by John Macallister, Gino Saitta and Willy Black. They were always eager to listen and provided many utility programs to make life considerably easier.

Fellow students who, I hope, have become lifelong friends include John McNicholas, Richard Batley, Steve Yarker, Mike Villers and Ken Bell.

I would like to thank all the friends who I have met through my association with Wolfson College, particularly Michelle Hicks, Noel Blatchford and Carolyn Hartley.

I gratefully acknowledge financial assistance from the Science and Engineering Research Council and the Clarendon Laboratory.

CONTENTS

CHAPTER 3

HADRON ARM SHOWER COUNTERS (HASC)

CHAPTER 4

DATA ACQUISITION AND REDUCTION

CHAPTER 5

DETERMINATION OF THE BHABHA CROSS SECTION

CHAPTER 6

ANALYSIS OF THE $e^+ e^- \rightarrow e^+ e^- \gamma$ FINAL STATE

CHAPTER 1

Bhabha Scattering

1.1 Introduction

The subject of this thesis is the experimental study of the reaction $e^+ e^- \rightarrow e^+ e^-$, Bhabha scattering, and an investigation of hard photon bremsstrahlung in the Bhabha reaction. The later study can be used as a direct method to search for the existence of an excited electron state e^*, as its principal decay mode is expected to be radiative decay, $e^* \rightarrow e + \gamma$. The data used was collected by the TASSO (Two Arm Spectrometer SOlenoid) experiment which was situated at the PETRA (Positron Electron Tandem Ring Accelerator) storage ring facility at the DESY (Deutsches Elektronen-Synchrotron) accelerator complex in Hamburg, West Germany. During the data period covered by this thesis PETRA achieved energies approximately 5 times greater than those of any previous e^+e^- storage ring. This meant that the available momentum transfers ($Q^2 > 1000$ Gev^2) for QED and weak interaction processes were an order of magnitude greater than had been studied in neutrino scattering experiments. This chapter introduces the Bhabha reaction as a test of QED (Quantum Electrodynamics) at high momentum transfers and the parameterisations used to quantify deviations from QED predictions. The possible effects which might be expected from electroweak unification models are then discussed. These effects are from interference terms in the cross section and increase with

centre of mass energy. At the highest energies accessible to this study they may be used to impose limits on the parameters of the electroweak models. They can also be used as a unique test of models which predict more exotic gauge boson spectra. The final part of the Chapter discusses some aspects related to the calculation of the hard photon bremsstrahlung cross sections from QED and includes the theory appropriate to the production and detection of a possible e^* state.

1.2 Bhabha Scattering and QED (Quantum Electrodynamics)

Quantum ElectroDynamics is a theory of the interactions of electrons and photons. It accounts for the force between them via the exchange of virtual electrons and photons. The coupling parameter, $\alpha=\frac{1}{137}$, which expresses the characteristic strength of the electromagnetic interaction is sufficiently small to permit the use of perturbation expansion methods in the calculation of physical quantities. The diagrammatic representation of terms in the expansion series is embodied in Feynman diagrams[1]. Vertex and particle propagator terms can be associated with parts of each diagram and cross sections can be evaluated by considering all possible diagrams which contribute to a given order. Technical difficulties occur in diagrams which contain internal loops due to the occurrence of infinities in integrals over the loop momenta. However these can be overcome using renormalisation techniques and it can be shown that physically measureable quantities remain finite and unambiguous.

1.2.1 Lowest Order Prediction

Using the methods of perturbative QED the lowest order diagrams for Bhabha scattering are those shown in Figure 1.1(a). Upon evaluation the differential angular cross section $\frac{d\sigma_0}{d\Omega}$ is (assumming no polarisation and in an ultra-relativistic approximation)

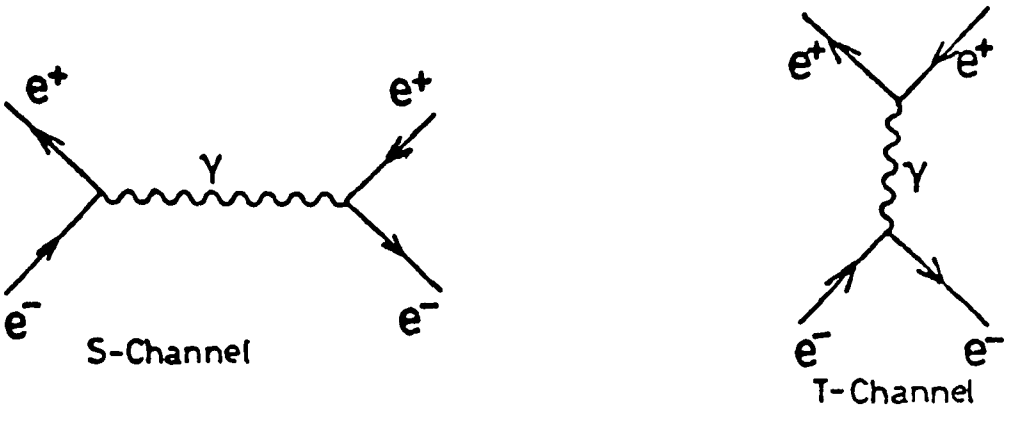

(a) Lowest order diagrams

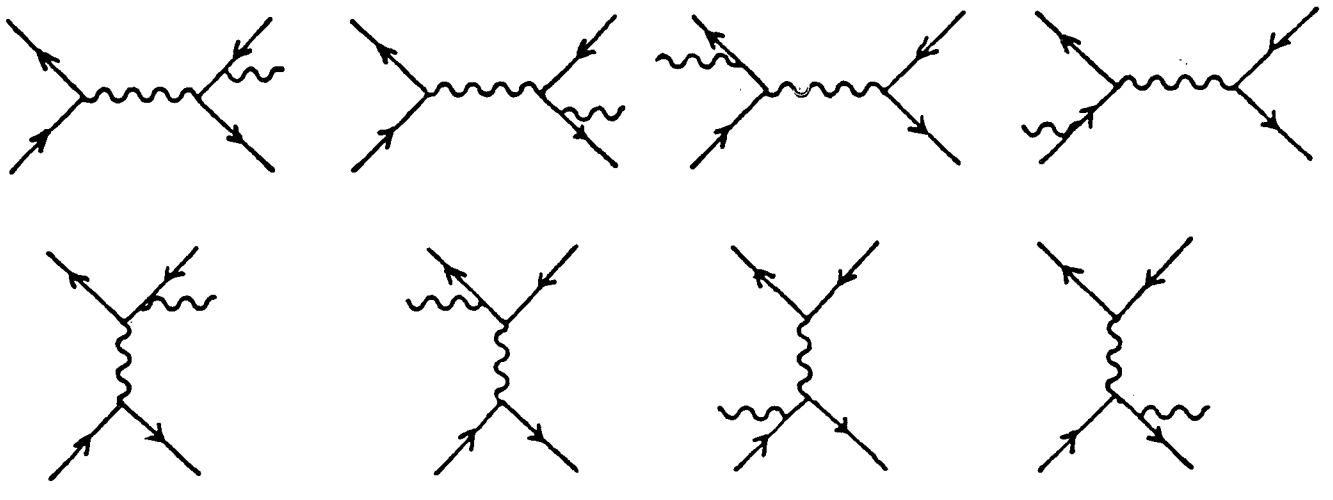

(b) Bremsstrahlung diagrams

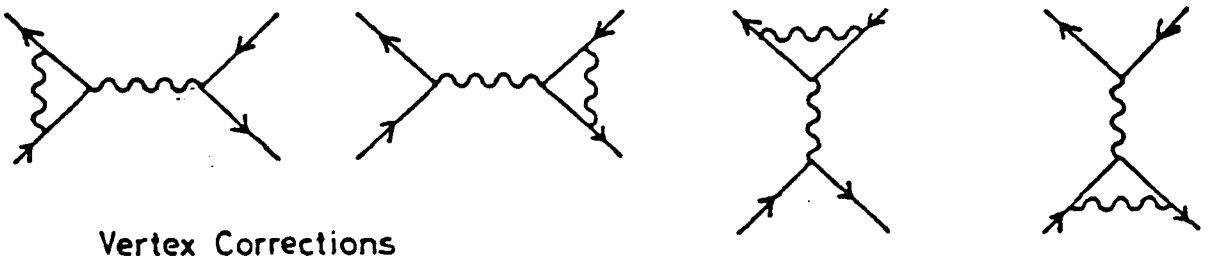

Vertex Corrections

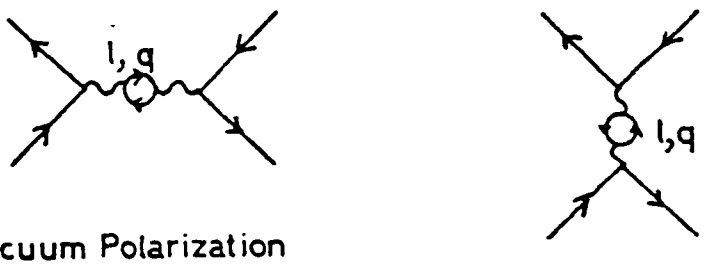

Vacuum Polarization

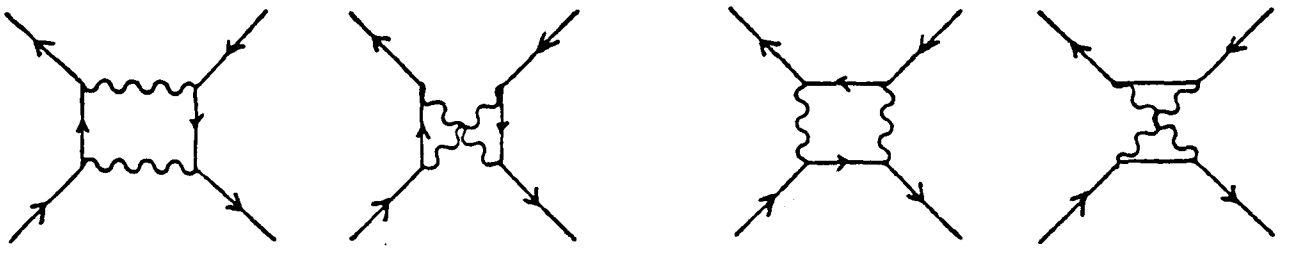

(c) Virtual diagrams

Figure 1.1 Feynman diagrams for Bhabha scattering to order α^3.

$$\frac{d\sigma_0}{d\Omega} = 2\pi \frac{d\sigma_0}{d\cos(\theta)} = \frac{\alpha^2}{4s}\left(\frac{10 + 4x + 2x^2}{(1-x)^2} - \frac{2(1+x)^2}{1-x} + (1+x^2) \right) \quad (1.1)$$

$$\frac{d\sigma_0}{d\Omega} = \frac{\alpha^2}{4s}\left(\frac{3 + x^2}{1 - x}\right)^2 \quad (1.2)$$

where $\sqrt{s}$ is the centre of mass energy of the 2 equal energy colliding particles and $x=\cos(\theta)$ where θ is the scattering angle of the e^-. Figure 1.2 shows this scattering angle together with a plot of the cross section formula of equation (1.1). The first term of (1.1) can be associated with the cross section of the scattering or t channel diagram of Figure 1.1(a). It is similar to the Rutherford formula for the scattering of point-like objects. The contribution of this term is sharply peaked at forward scattering angles corresponding to low values of the momentum transfer $t=-\frac{s}{2}(1-x)$. The third term is from the annihilation or s channel diagram 1(b) and has the characteristic $1+\cos^2(\theta)$ dependence for the production of spin $\frac{1}{2}$ particles from a virtual photon. The second term is the interference term of the 2 diagrams. To lowest order the cross section varies as $\frac{1}{s}$. It is often most convenient to factor out this dependence and present the scaled cross section $s\frac{d\sigma}{d\Omega}$.

1.2.2 Higher order QED contributions to Bhabha scattering [2]

Figure 1.1(b) shows the higher order QED diagrams which contribute to the Bhabha cross section, up to order α^3. Typically the sum of contributions from this order is expected to be a few percent of that of the lowest order diagrams discussed above. The diagrams can be grouped into virtual diagrams of order α^4 and bremsstrahlung diagrams of order α^3. The virtual diagrams contribute to order α^3 by their interference term with the lowest order diagrams, which are of order α^2. The virtual diagrams produce events which are indistinguishable from lowest order events but some of the bremsstrahlung diagrams lead to events in which hard photons are emitted at large angles with respect to the charged

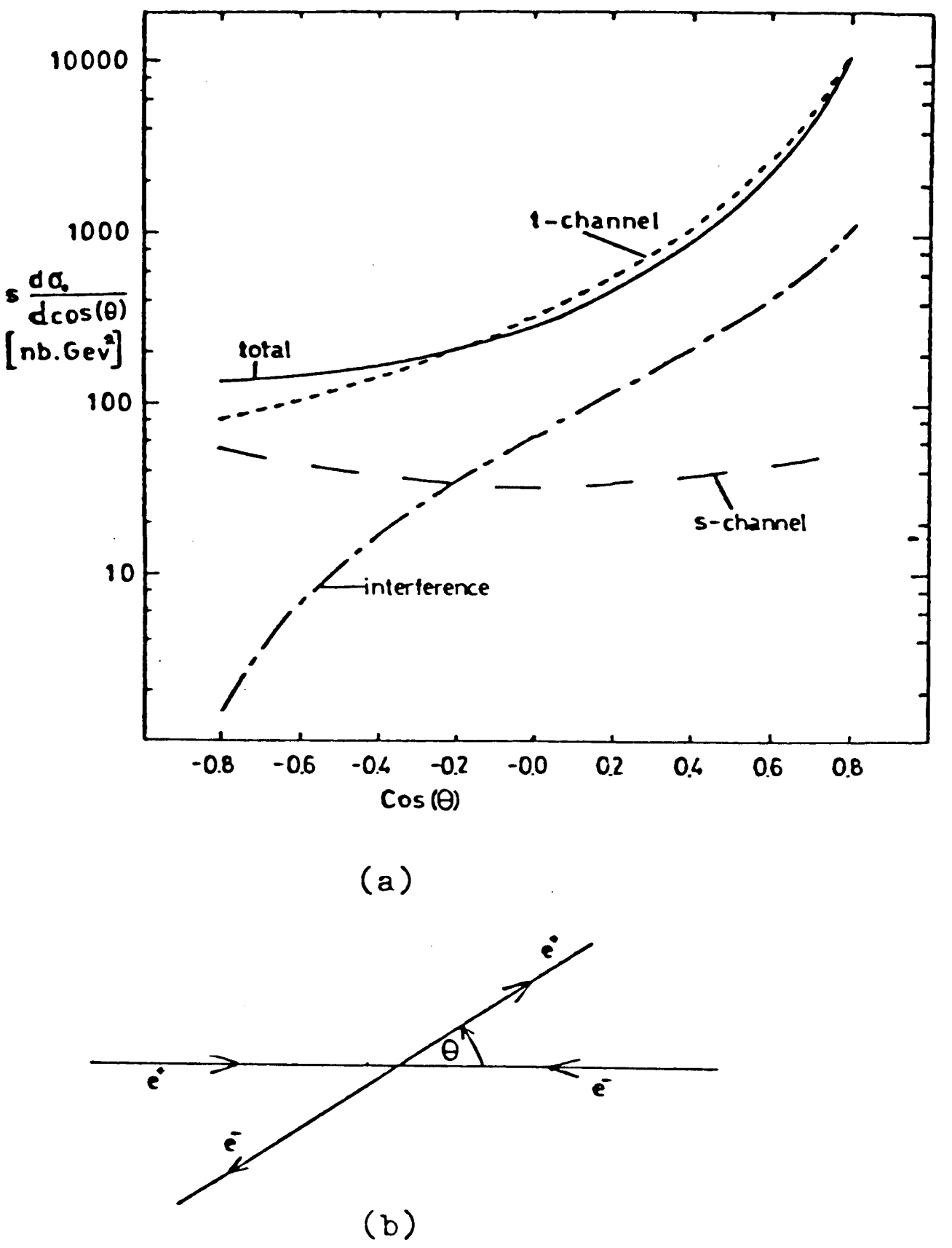

Figure 1.2 Plot of lowest order cross section for Bhabha scattering and definition of scattering angle, θ.

particles. These events can be isolated and removed from an experimental sample or their contribution can be calculated and they can be classified as Bhabha events. Their contribution to a particular experimental situation will depend upon the resolution and properties of the detecting apparatus and the event selection criteria used. The conventional practise is to calculate the contribution of all the higher order diagrams, taking into account the specific experimental situation and selection criteria, and to correct the observed data numbers to present the cross section contribution of the lowest order alone. This is a number which is comparable for all experimental groups. Generally we can write

$$\frac{d\sigma}{d\Omega} = \frac{d\sigma_0}{d\Omega}(1 + \delta_{tot}) \qquad (1.3)$$

where $\frac{d\sigma}{d\Omega}$ is the cross section involving higher orders and δ_{tot} is called the radiative correction. δ_{tot} can be reduced to

$$\delta_{tot} = \delta_{virtual} + \delta_{bremsstrahlung} \qquad (1.4)$$

and

$$\delta_{bremsstrahlung} = \delta_{soft} + \delta_{hard} \qquad (1.5)$$

where hard and soft refer to the energy of the emmitted bremsstrahlung photons.

The calculation of $\delta_{virtual}$ involves terms from self-energy, vertex and vacuum polarisation diagrams. They are all calculable from standard QED except for the vacuum polarisation from quark loops. However this term can be related by a dispersion relation to the experimentally accessible cross section for hadron production via single photon

annihilation.

The soft part of the bremsstrahlung calculation suffers from the problem that it is infra-red divergent. However parts of the calculation of the virtual terms suffer the same problem and it is possible to show that the infinities from the two cancel to yield a finite result for the overall cross section.

Features of the calculation of the hard part of the bremsstrahlung calculation are discussed in section 1.4.

1.2.3 Parameterisations of Deviations from QED

One of the fundamental assumptions in deriving the zeroth order QED cross section formula of equation (1.1) is that the particles and couplings of the interactions are pointlike. In this case the form of the photon propagator leads to the $\frac{1}{s}$ dependence of the cross section. We can modify the theory and allow the occurrence of form factor like terms[3],[4]:

$$F_s(t) = 1 \pm \frac{t}{t - \Lambda_{\pm,s}^2} \qquad (1.6)$$

$$F_t(s) = 1 \pm \frac{s}{s - \Lambda_{\pm,t}^2} \qquad (1.7)$$

This will lead to a general form for the zeroth order cross section of

$$\frac{d\sigma_0}{d\Omega} = \frac{\alpha^2}{4s}\left(\frac{10+4x+2x^2}{(1-x)^2}|F_s|^2 - \frac{2(1+x)^2}{(1-x)}\mathrm{Re}(F_s F_t^*) + (1+x^2)|F_t|^2\right) \qquad (1.8)$$

The Λ parameters of this modified formula quantify the agreement of the observed cross section with that of pure QED. The modified formula agrees with the QED formula as $\Lambda \to \infty$. Figure 1.3 shows the ratio of the

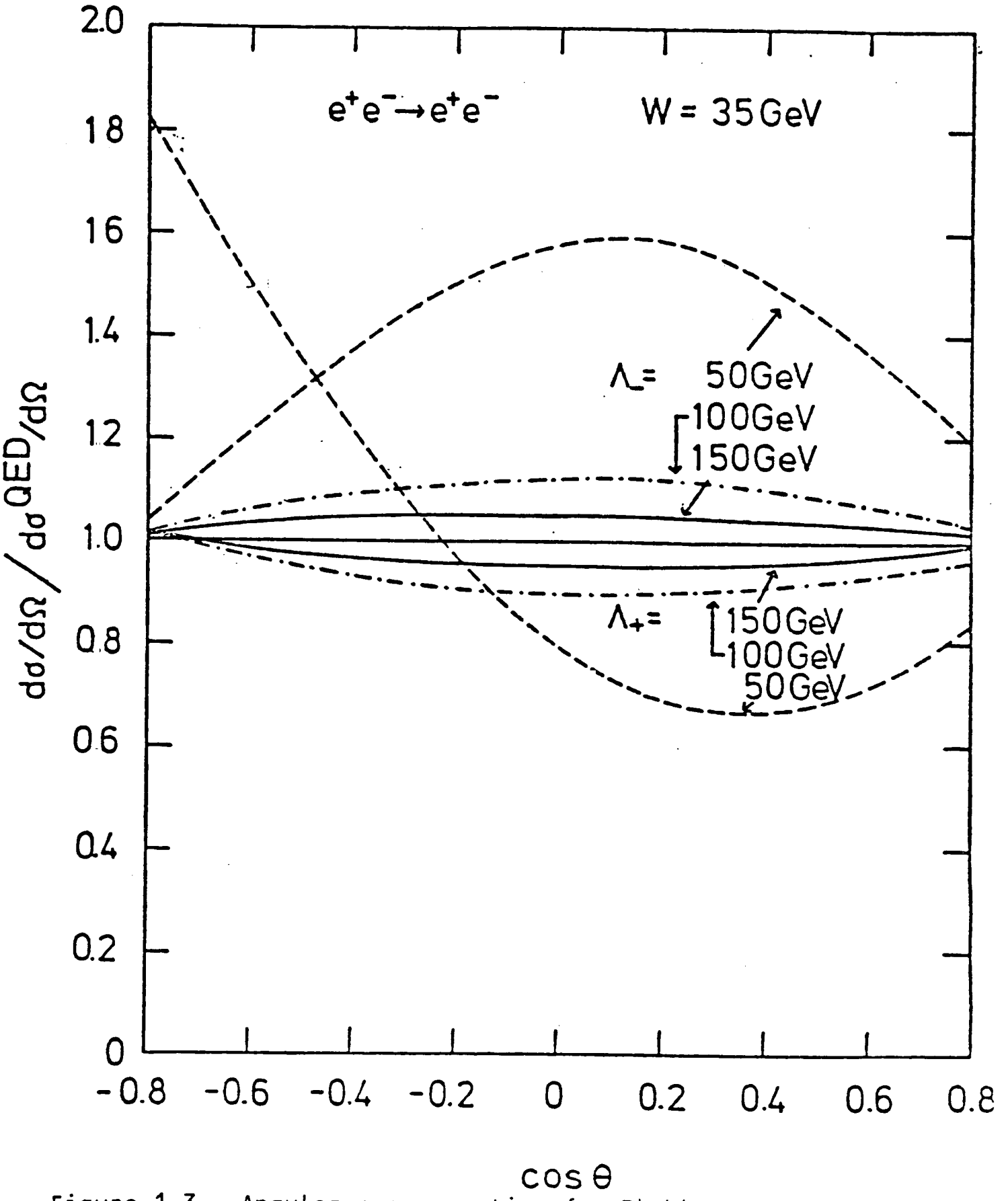

Figure 1.3 Angular cross section for Bhabha scattering with Λ parameter modification divided by the lowest order QED prediction.

modified cross section value compared to QED for several trial values of Λ ($\Lambda_s=\Lambda_t$). In terms of a space-time picture, the Coulomb potential is modified at small distances to give:

$$\frac{1}{R} \rightarrow \frac{1}{R}\left(1 \pm \exp(-\Lambda_{\pm} R) \right) \qquad (1.9)$$

Thus lambda parameters measure the limiting distance L down to which QED is valid ($L=\frac{\hbar c}{\Lambda}$).

Yanagisawa[5] discusses in further detail possible interpretations of these Λ parameters. Λ_+ can be interpreted as measuring the effect of an extra vector-boson resonance while Λ_- can be interpreted as the squared mass of a heavy photon.

Marshall[6] has criticised the use of Λ parameters because experimentally they fail to distinguish between precise and imprecise experiments and because theoretically they do not characterise the deviations from QED which are expected from the electroweak theories discussed below.

1.3 Electroweak Gauge Theories

The first sucessful theory of the weak interactions was the point like coupling theory of Fermi, which described weak currents of V-A structure. This theory was known to produce unphysical results at high energies. This was associated with the point like coupling assumption of the theory. Modern gauge theories of the weak interaction envisage the weak force as being due to the exchange of vector bosons, in analogy with the electromagnetic interaction being mediated by virtual photon or electron exchanges. The similarity can be carried further as the properties of both weak and electromagnetic currents can be embodied in a group representation and these groups can be embedded as elements in a larger unifying group. The disparity of the 2 interactions at low energies is a consequence of a complicated phenomenon known as spontaneous symmetry breaking. This mechanism introduces a scalar particle, the Higgs, of undefined mass, into the theory. The effect is to mix the massless elements of the primordial group to produce the physical boson states seen in nature. A consequence is that the boson mediating electromagnetic exchanges is massless making the force of infinite range whereas the weak bosons acquire mass and hence are short range forces. The exact number and masses of bosons is dependent on the gauge group chosen to represent the interaction. If the extra bosons have masses much greater than the centre of mass energy under study they will not affect the predictions of QED.

1.3.1 Standard Model or Glashow Weinberg-Salam (GWS) Theory[7]

Most models of the electroweak interaction require the existence of 1 or more neutral weak bosons. The experimental discovery of weak neutral currents in neutrino scattering experiments at CERN confirmed their existence. It is these neutral bosons which are of interest to the study of the Bhabha scattering process as they allow the interaction to proceed via the virtual exchange of these weak bosons as well as via the QED

photon exchange. The successful explanation of low energy data by the point coupling weak interaction theory of Fermi leads to an estimate of about 100 Gev for the mass scale of the weak bosons. At centre of mass energies of 35 Gev the direct effects of the virtual exchange of the Z_0 are negligible. However it is expected that interference terms between the weak and electromagnetic exchanges (proportional to $\alpha^*\alpha_w$) will be of the order of a few percent and therfore measureable.

Using the formalism of Bundy[8] a general form of the electroweak differential cross section for Bhabha scattering is:

$$\frac{8s}{\alpha^2}\frac{d\sigma}{d\Omega} = 4B_1 + (B_3 + B_2)(1 + x^2) + 2(B_3 - B_2)x \qquad (1.10)$$

$$B_1 = (\frac{s}{t})^2 \left|1+(g_v{}^2 - g_a{}^2)Q\right|^2 \qquad (1.11)$$

$$B_2 = \left|1+(g_v{}^2 - g_a{}^2)R\right|^2 \qquad (1.12)$$

$$2B_3 = \left|(1+\frac{s}{t}+(g_v+g_a)^2)(\frac{s}{t}Q+R)\right|^2 + \left|(1+\frac{s}{t}+(g_v-g_a)^2)(\frac{s}{t}Q+R)\right|^2 \qquad (1.13)$$

where g_v and g_a are the vector and axial vector couplings of the weak current. Generally the factors Q and R are arbitary but for a model with a single neutral boson of mass M_z and width Γ they are given by

$$Q = \frac{G_F M_Z{}^2}{2\pi\alpha\sqrt{2}}\frac{t}{t-M_Z{}^2+iM_Z\Gamma} \qquad (1.14)$$

$$R = \frac{G_F M_Z{}^2}{2\pi\alpha\sqrt{2}}\frac{s}{s-M_Z{}^2+iM_Z\Gamma} \qquad (1.15)$$

with Fermis' constant, $G_F = \frac{1}{293}$ Gev^2 and $e^2 = 4\pi\alpha$.

The simplest and so far most successful candidate model for the electroweak interaction is based on the SU(2)×U(1) gauge group. This is the Glashow-Weinberg-Salam model. This predicts 2 charged weak bosons and

a neutral weak boson with vector and axial vectors couplings given by

$$g_v = -\frac{(1 - 4\sin^2(\theta_w))}{2} \tag{1.16}$$

$$g_a = -\frac{1}{2} \tag{1.17}$$

The masses, in Gev, of the bosons are related to g_v and g_a via

$$M_{Z_0} = \frac{74.6}{\sin(2\theta_w)} \tag{1.18}$$

$$M_{W\pm} = \frac{(37.3)}{\sin(\theta_w)} \tag{1.19}$$

At PETRA energies the GWS cross section can be written as

$$\frac{d\sigma}{d\Omega} = \frac{\alpha^2}{4s}\left\{ \left(\frac{3+x^2}{1-x}\right)^2 - \frac{Re(R(s))}{e^2\,(1-x)}\left(2(1+x)^3(g_v^2+g_a^2) + (8-(1-x)^3)(g_v^2-g_a^2) \right) \right\} \tag{1.20}$$

where we have used $M_Z >> s$, $M_Z >> t$, $M_Z > \Gamma$ and thus $Q = -\frac{(1-x)}{2}R$.

Figure 1.4 shows the ratio of the GWS cross section to that of QED for several trial values of $\sin^2(\theta_w)$, the one parameter of the theory.

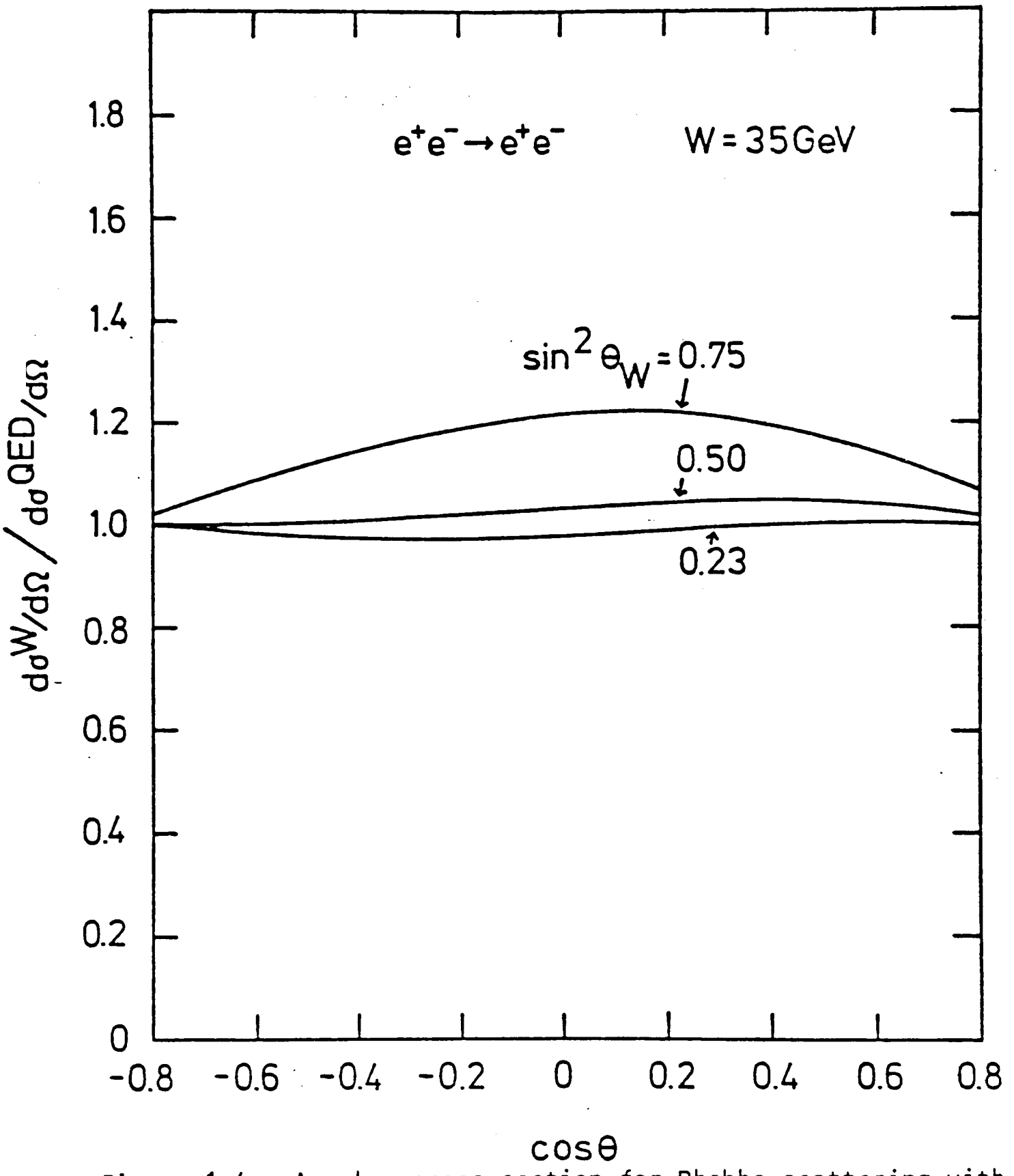

Figure 1.4---Angular cross section for Bhabha scattering with GWS electroweak prediction divided by the lowest order QED prediction.

1.3.2 Multi Neutral Boson Theories[9]

Several models of the electroweak interaction have a richer boson structure than SU(2)×U(1) while giving essentially similar low energy predictions. The effect of these models is to add a term of the form $C\, j_{em}^{\,2}$ to the Lagrangian of standard QED to give an effective neutral current Lagrangian of :

$$L_{eff} = \frac{4G_F}{\sqrt{2}} \{ (j_3 - \sin^2(\theta_w) j_{em})^2 + C j_{em}^{\,2} \} \qquad (1.21)$$

where j_3 is the third component of the weak isospin current and j_{em} is the electromagnetic current.

The coefficient C can be regarded as a parameterisation of the deviation from a single boson situation for a whole class of candidate models and as such is an important experimental figure.

The consequences of these models can best be explored in $e^+ e^-$ collisons for 2 reasons[10] :

1./ The extra term couples to the electromagnetic current and therefore cannot be detected in weak neutral current neutrino experiments.

2./ The electromagnetic term is parity conserving and will produce no asymmetry in electron deuteron scattering experiments which also measure electroweak interference effects.

Two specific models are of particular interest in this category.

1) SU(2)×U(1)×U(1) model of de Groot et al[11]. This predicts 2 neutral bosons and 2 charged bosons. The charged bosons have the masses of the standard $W^{\pm}$.

2) SU(2)×U(1)×SU(2) model of Barger et al[12] . This predicts 2 neutral bosons and 4 charged bosons.

Both of the above models predict a neutral boson spectrum with 1 boson having a mass greater than the Z_0 boson of the SU(2)×U(1) model and the other a mass less than the Z_0 of SU(2)×U(1). This is a consequence of the spontaneous symmetry breaking mechanism used to generate the masses.

For these 2 models C can be related to the masses of the 2 neutral bosons using

$$C = \cos^4(\theta_w)\,\frac{(m_2^2 - M_z^2)\,(M_z^2 - m_1^2)}{m_1^2\, m_2^2} \quad \text{De Groot et al} \qquad (1.22)$$

$$C = \sin^4(\theta_w)\,\frac{(m_2^2 - M_z^2)\,(M_z^2 - m_1^2)}{m_1^2\, m_2^2} \quad \text{Barger et al} \qquad (1.23)$$

This shows that the coupling of the model of de Groot will produce sizeable effects if a low mass Z_0 exists.

1.4 Hard Photon Bremsstrahlung in Bhabha scattering

The study of hard photon production in Bhabha scattering can be an important test of the higher order predictions of standard QED[13] and of the production and subsequent decay of an excited electron state, e^*.

The calculation of the cross section for the production of photons in the QED Bhabha reaction, to order α^3, involves the evaluation of the eight diagrams of Figure 1.1(b). The contribution of these graphs can become relatively large because when a photon of energy k is emitted the remaining center of mass energy of the colliding $e^+ e^-$ is $s' = s\,(1-\frac{k}{E_B})$. At this lower energy zeroth order cross sections are enhanced by a factor

of s / s'. For a beam energy E_B of 15 Gev and a photon energy of 14 Gev this enhancement factor is as large as 15[14].

The first exact calculation of the eight bremsstrahlung graphs was performed by Vortruba. His results are extremely complicated. Swanson[15] evaluated the formula using computer algebra techniques for the trace calculations and numerical integration methods for the integrals over phase space. The calculation had of the order of 1000 terms in the traces and he calculated the phase space factor to better than 1% over most of the phase space. He concluded, as had been previously discovered by Alterelli at al[16], that for forward angles only the t channels graphs are important. This effectively reduces the problem to the calculation of 2 diagrams. Swanson showed that except for very large photon energies, where the initial state s channel diagrams dominate, the small angle formula could be empirically modified to agree with the exact formula.

Most recently Berends et al[17] have treated the phase space integration of the calculation in a symmetric way with respect to the 2 charged particles by utilising an 'average' scattering angle. This angle is defined as that between the incident beam axis and the momentum difference vector of the 2 charged particles, see Figure 1.5. For elastic scattering events in which no photon is emitted this 'average' angle is the same as the angle of scattering of either charged particle. Berends et al have derived elegant and surprisingly simple formula in the relativistic limit. They have incorporated their results in a Monte Carlo program for the generation of Bhabha events[18]. This has become the standard generator for use in Bhabha scattering studies and is utilised heavily in the work of this thesis.

1.5 Excited electron states

If a heavy excited electron state exists it can be produced and detected in $e^+ e^-$ collisions either in pairs or singly[19] i.e.

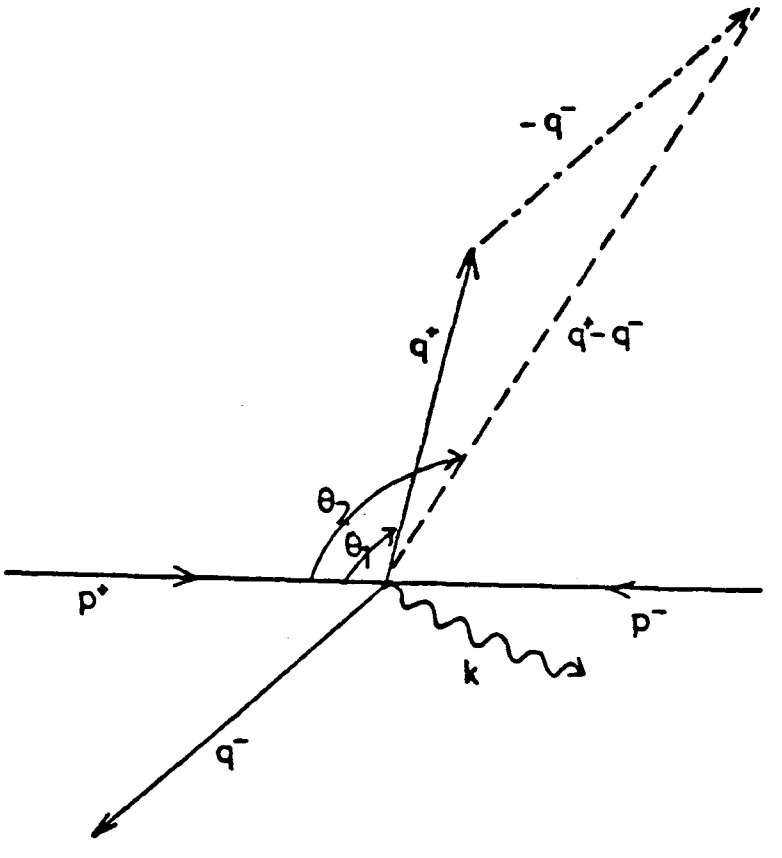

Figure 1.5 Definition of the 'average' scattering angle, θ_2 used by Berends in the calculation of bremsstrahlung. θ_1 is the conventional scattering angle.

$$a) \quad e^+ + e^- \rightarrow e^{+*} + e^{-*} \tag{1.24}$$

$$b) \quad e^+ + e^- \rightarrow e^{+*} + e^- \tag{1.25}$$

The e^* is expected to decay in an unmeasurable short time to an electron (or positron) and a photon. The single e^* production process is expected to be most sensitive to the existence of such a state because:

1) process (a) can only produce e^* states with a mass, M, up to the energy of the beam, while the single production mechanism can give e^* states with masses up to $2\times E_B$.

2) The cross section of process (b) is larger because it involves a magnetic coupling

$$j^\mu = \bar{u} \ \frac{e\lambda}{M} \sigma^{\mu\nu} q_\nu \ u \tag{1.26}$$

with $\sigma^{\mu\nu} = \frac{1}{2}(\gamma^\mu\gamma^\nu - \gamma^\nu\gamma^\mu)$, and $\frac{\lambda}{M}$ the coupling strength of the e^* to the photon.

The more usual electromagnetic coupling is

$$j^\mu = \bar{u} \ \gamma^\mu \ u \tag{1.27}$$

but this coupling is forbidden as it would violate current conservation because there are different mass particles in the final state. The magnetic coupling of equation (1.26) contributes to the calculation of the anomalous magnetic moment of leptons. However in the present context it produces a non renormalisable coupling.

The lowest order Feynman diagrams for e^* production and subsequent decay are shown in Figure 1.6. The differential cross section for the single production of an e^*, of mass M, has been evaluated to be[20]

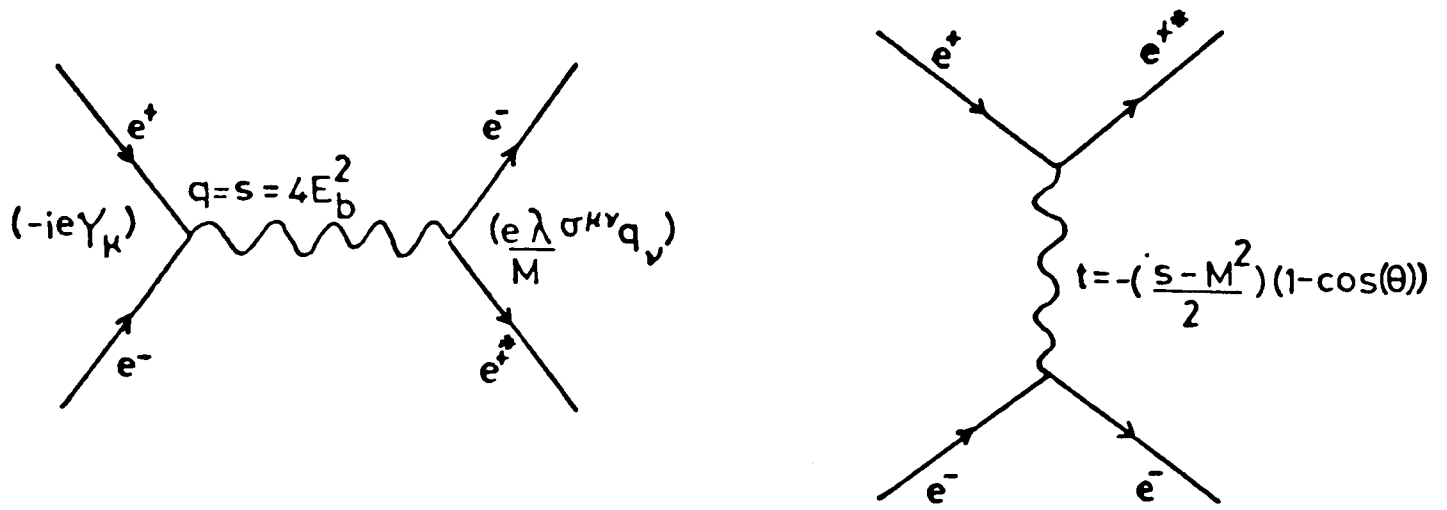

(a) Production diagrams

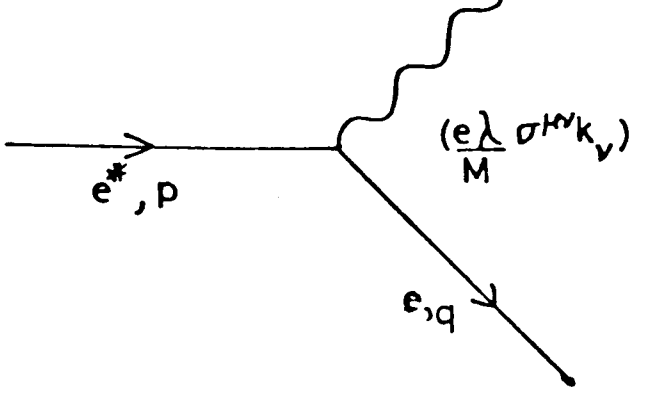

(b) Decay diagram

Figure 1.6 Lowest order Feynman diagrams for excited electron production and decay using a magnetic interaction.

$$\frac{d\sigma}{dt} = -\frac{2\pi\alpha^2\lambda^2}{M^2s^2}\left(\frac{t^2+(t-M^2)^2}{s} + \frac{s^2+(s-M^2)^2}{t}\right) \qquad (1.28)$$

where λ is the strength of its electromagnetic coupling and $t=-\frac{s}{2}(\frac{s-M^2}{s})(1-\cos(\theta))$, the momentum transfer in the t channel.

Limits on the existence of an e^* can be inferred from three other experimental measurements. The reaction

$$e^+ + e^- \rightarrow \gamma + \gamma$$

which occurs via the exchange of a virtual electron. If a massive e^* exists this will contribute an extra exchange channel and the angular cross section for the process will be modified. Current PETRA experiments limit the mass of a virtual e^* to greater than 40 to 50 Gev[21].

A second possibilty is the effect of an excited electron state on direct e γ collisions. Renard [22] discusses both the virtual effects of the exchange of an excited electron and the resonant production of such an object. He claims that for a high mass e^* the limits obtained from the Compton process should be comparable with those from the $e^+e^-\rightarrow\gamma\ \gamma$ process.

A third indirect measurement is the comparison of the experimental and theoretical values of the anomalous magnetic moment of the electron, $(g-2)_e$. Goldberg[23] has used the uncertainty in these values to argue that they place severe limits on any possible substructure of the electron and therefore rule out e^* states with masses less than a few Tev. However Kovesi-Domokos et al[24] consider models of excited lepton states in which the constituents have masses on the scale of Tev but the observed bound states are in the mass range 20-60 Gev. Therefore from a theoretical point of view the question remains open to dispute. It is probably best

resolved by as direct an experimental investigation as is possible.

CHAPTER 2

Experimental Apparatus

2.1 Introduction

This Chapter describes the apparatus used in the data collection for this thesis. The TASSO collaboration involved physicists from institutes in England,Germany,Israel and the USA. Appendix 1 lists the members of the collaboration during the years 1979 and 1980. The TASSO detector was situated in the south east experimental hall of PETRA at DESY.

2.2 DESY

The layout of the DESY accelerator site is shown in Figure 2.1. Several of the older accelerators at DESY were used in the production and acceleration of electrons and positrons for the PETRA storage ring. 50 Mev electrons were produced by a LINAC (Linear Accelerator). They were then passed to the DESY storage ring where they were accelerated to 6.5 Gev prior to direct injection into the PETRA ring. The production of large positron currents was initially more laborious. Firstly 400 Mev positrons were produced by a LINAC and these were accelerated to 2.2 Gev in the DESY ring. Bunches of positrons were then fed into the DORIS storage ring and accumulated before transferring large currents back to DESY for acceleration and injection to PETRA at 6.5 Gev. In the summer of 1979 a new machine called PIA (Positron Intensity Accumulator) was built.

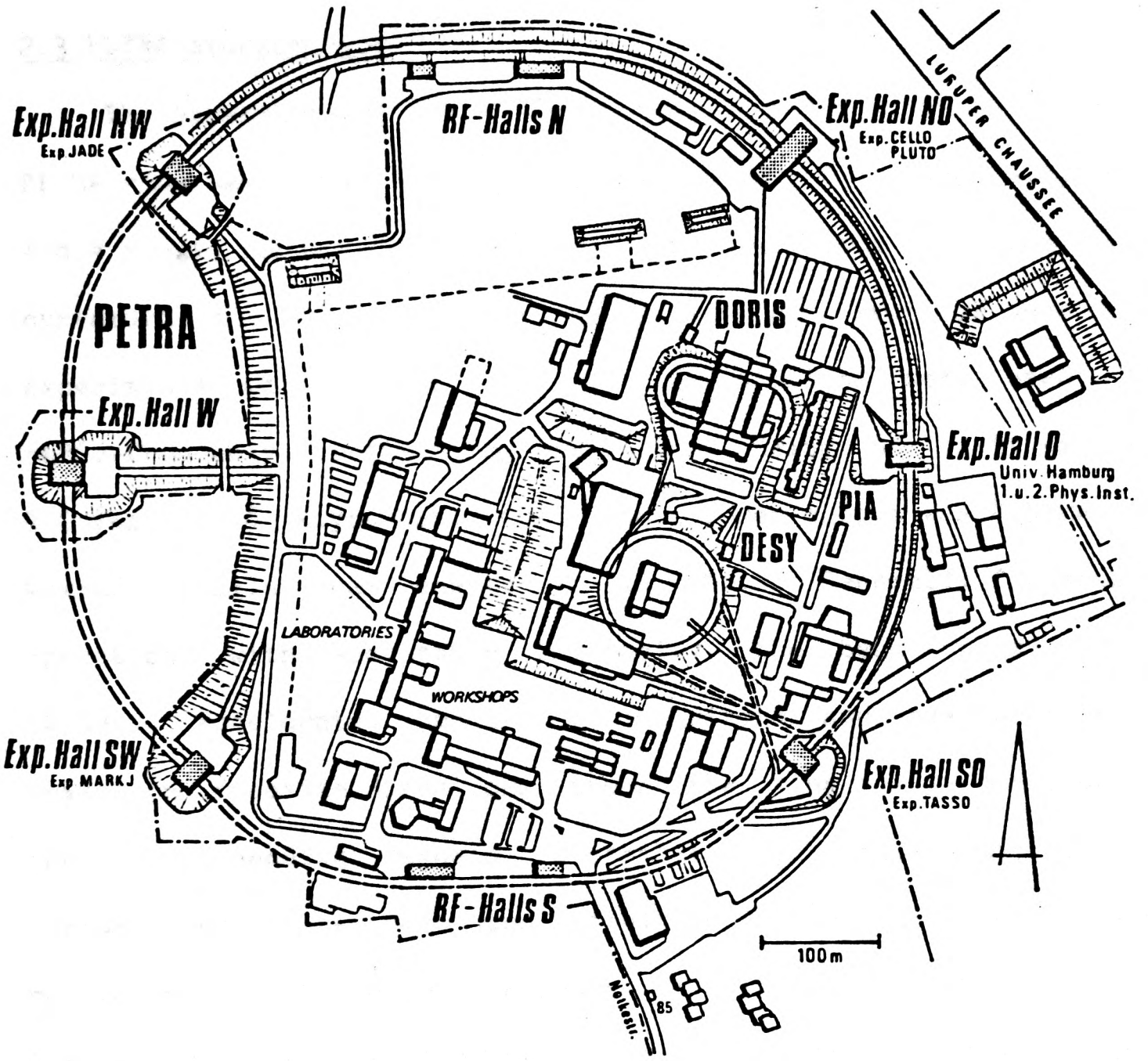

Figure 2.1 Layout of the DESY accelerator complex.

This produced large currents of positrons and therefore it was no longer necessary to accumulate them in DORIS. They followed the same injection scheme as electrons. This scheme allowed DORIS to return to a physics program involving the study of the upsilon resonances.

2.3 PETRA Storage Ring[25],[26]

The parameters of the PETRA storage ring are given in Table 2.1. The PETRA ring was 2.3 km in circumference and had 8 straight sections, 4 long and 4 short, connected by 8 bending magnet sections which had a radius of curvature of 256 m. The 4 short straight sections were occupied by experiments while 2 of the 4 long sections were used to house radio-frequency accelerating cavities. Using 64 cavities driven at 500 Mhz by 8 klystrons, the total power output was 4.5 MW allowing a maximum single beam energy of 18.3 Gev. Generally for stable 2 beam operation, with acceptable luminosity, the beam energy was less than 18 Gev. Accelerated bunches of electrons and positrons were made to travel in opposite directions around the ring being confined in stable orbit by bending magnets distributed uniformly around the whole circumference. The beam pipe within which the particles travelled was maintained at a vacuum pressure of less than 5×10^{-9} Torr. This was limited by outgassing of surface molecules in the beam pipe. The quality of the vacuum was important in determining both the beam lifetime and the rate of background processes at the experimental regions. The beams were brought together to collide by vertical electrostatic deflectors positioned either side of the experimental regions.

The beam energy spread was controlled by sextupole magnets but was eventually limited to 10 Mev at 15 Gev by synchrotron radiation losses emitted as the beams were accelerated or deflected.

The rate of events from a particular processes is directly related to the cross section for the process by a quantity called the luminosity.

	Design	Achieved	
Beam Energy	5 - 19	6 - 18.36	Gev
Maximum luminosity per interaction point	1.05×10^{32}	1.3×10^{31}	$cm^{-2}\ sec^{-1}$
Beam current	80	12	mA
Number of bunches per beam	1 - 4	2	
Number of interaction points	6 (8)	4	
Free length for experiments	10 - 20		m
Circumference	2304.0		m
Bending radius	192.05		m
Rf power	4.8		MW
Rf frequency	500		MHz
Length of accelerating structures	96		m
Injection energy	6.5		Gev

Table 2.1 Parameters of the PETRA storage ring.

$$\text{event rate} = \text{luminosity} \times \text{cross section} \qquad (2.1)$$

Simple theory relates the luminosity to machine operating parameters via [27]

$$L = \frac{(I^+ \times I^-)}{(g \times b \times f)} \qquad (2.2)$$

where $I^-(I^+)$ are the values of the electron (positron) currents stored, b is the number of stored bunches, f is the geometrical area of overlap of the bunches and g is the rotational frequency of the bunches. In practice, luminosity is limited at low energies by beam-beam interactions and at high energies by synchrotron radiation losses. During 1979 and 1980 PETRA was operated with 2 positron bunches colliding with 2 electron bunches and achieved a peak luminosity of $3\times10^{31}cm^{-2}s^{-1}$ at beam energies around 15 Gev with beam currents of 5×10^{-6} A. Over a typical 4 hour beam fill the luminosity averaged $1.5\times10^{31}cm^{-2}s^{-1}$ and thus an integrated luminosity of 100 nb^{-1} was collected each day.

2.4 The TASSO Experiment [28]

The TASSO detector is shown in Figure 2.2. In all figures directions are referred to a right-handed coordinate system having the +z coordinate defined by the direction of motion of the circulating positron beam and with the +x axis in the plane of the PETRA ring and pointing towards the centre of that ring. The variables r,Θ and ϕ are the conventional polar coordinate variables used in such a coordinate system.

In e^+e^- collisions, processes of physics interest occur with small cross sections and, as the centre of mass frame (CM frame) generally coincides with the laboratory frame, products emerge over a wide angular range. Therefore the TASSO detector was designed to cover as large a solid angle as possible and was equipped with an integrated modular detector system

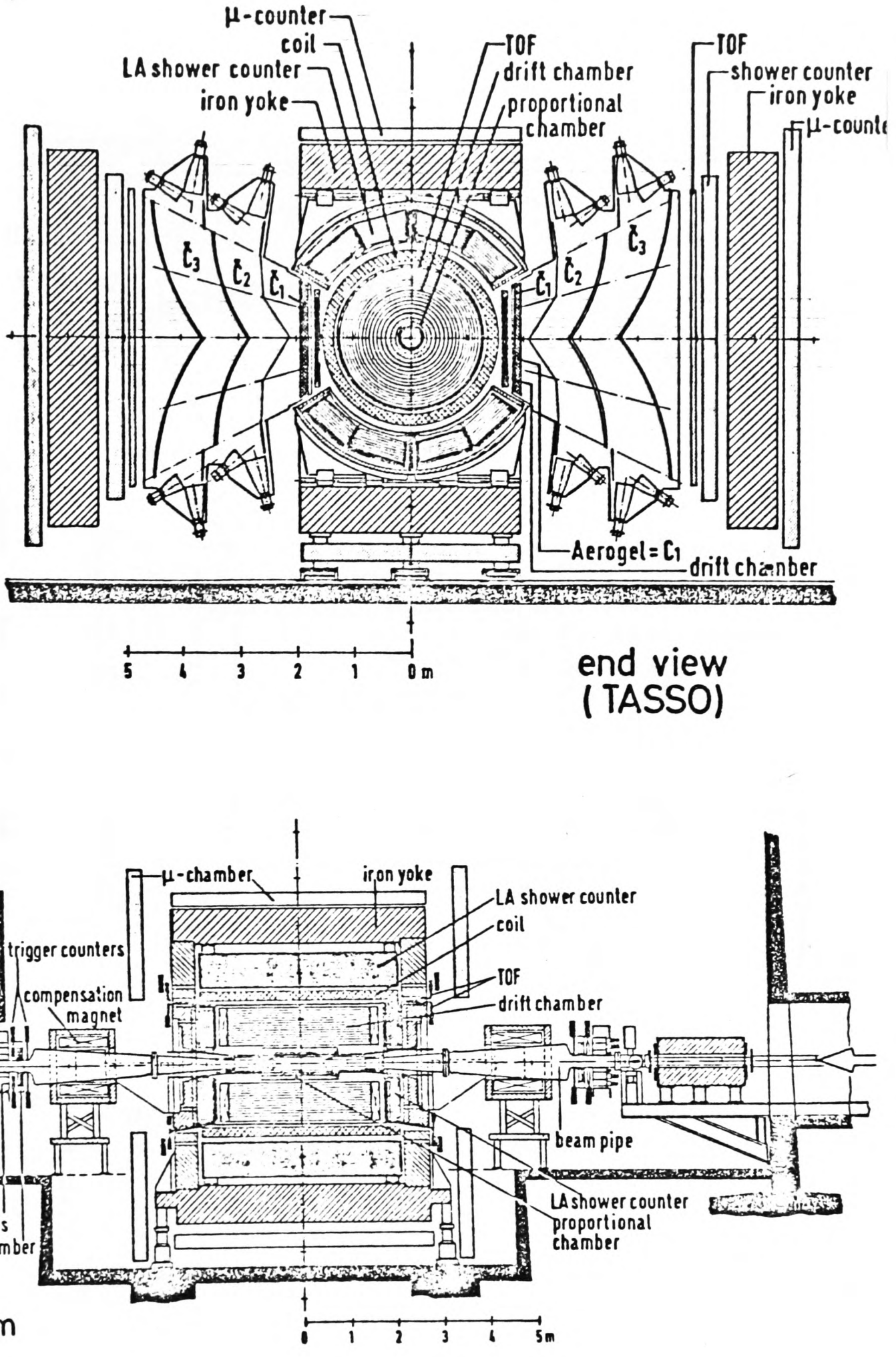

Figure 2.2 Views of the TASSO experiment.

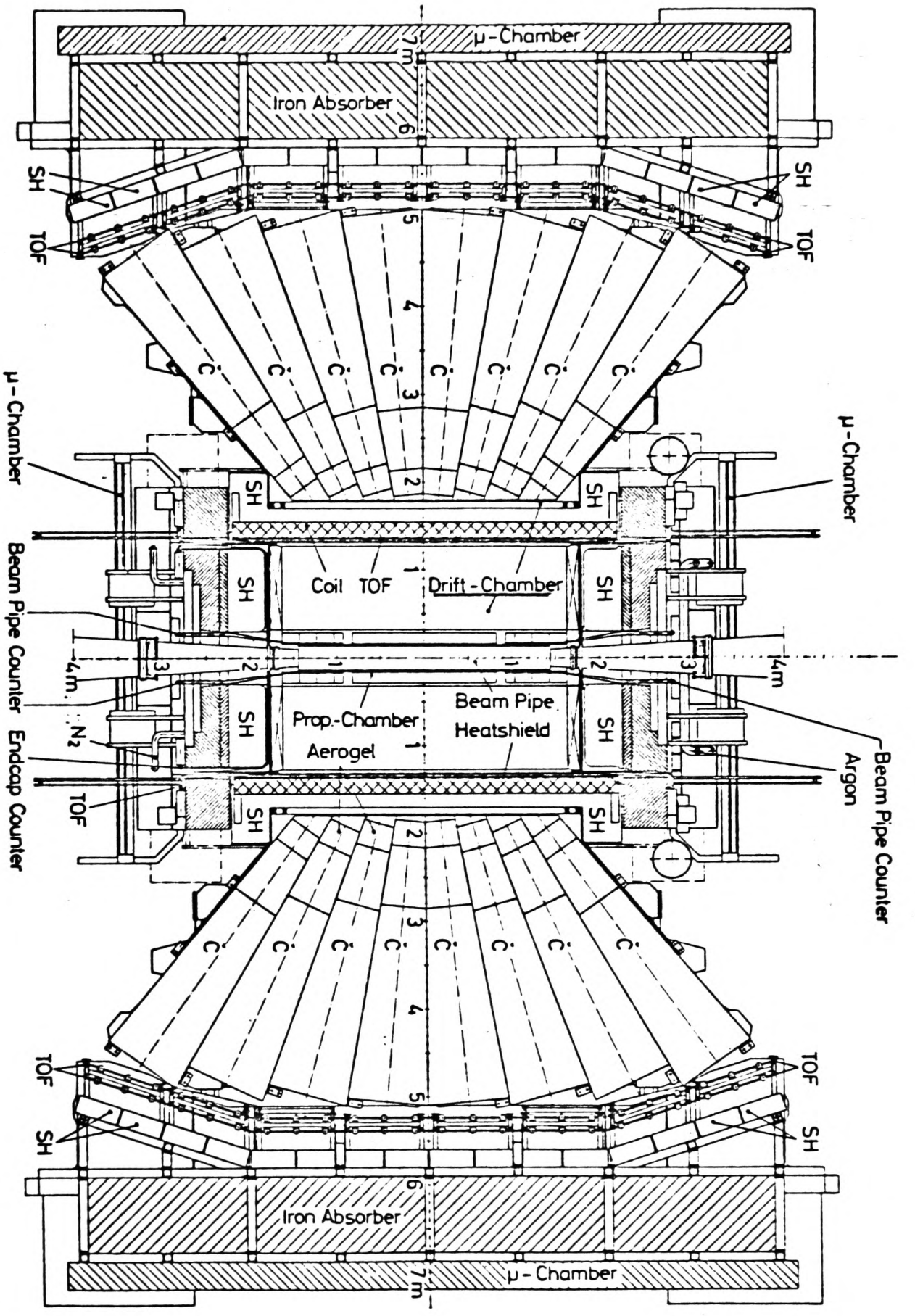

Figure 2.2 (cont.) Views of the TASSO experiment.

Structurally the detector can be divided into 3 major sections

Central Detector The large Central Detector had a magnetic field and proportional and Drift Chambers to measure charged particle momenta. It had shower counters to detect neutral products. A Time Of Flight (TOF) system was used with tracking information to provide some particle identification and trigger signals. The thick iron of the magnet yoke was surrounded by large area proportional tube arrays to form a muon identifier.

Hadron Arms At the sides of the Central Detector were 2 spectrometer arms containing several different types of Cerenkov counters, a large TOF array, shower counters and more iron and proportional tubes to form another muon identifying array. Principally these were all involved in particle identification. These spectrometer arms were referred to as the Hadron Arms because they were intended to be used to identify particles in hadron producing interactions.

Forward Detector At angles close to the beam axis a detector containing scintillator arrays, shower counters and proportional chambers. This was used to detect low q^2 Bhabha events in order to monitor luminosity. The cross section is well understood in this kinematic region and is large enough to provide an accurate measurement of the luminosity. This detector was also important for the study of the 2γ processes resulting from the radiation of low energy virtual photons in the initial state.

The elements of the detector relevant to the work of this thesis will now be described in further detail beginning with the parameters of the magnet and then describing components in rough order as encountered on moving radially outwards in the x-y or r-ϕ plane from the intersection

point.

2.4.1 The Magnet

The 0.497 Tesla axial magnetic field used to momentum analyse charged particles was generated by a conventional water-cooled cylindrical aluminium coil. It had an inner radius of 1.35 m, a length of 4.4 m and was approximately 1.1 radiation lengths thick. The magnetic flux was returned through laminated iron end plates 0.5 m thick and through laminated iron plates 0.8 m thick at the top and bottom of the apparatus. These iron plates formed the framework of the Central Detector. At each end a retractable plug was cut to enable access to the ends of detectors within the solenoid. The uniformity of the field was surveyed with a 3D Hall probe and it was found to be uniform to better than 6% everywhere with 2% being a typical figure for most of the useful volume of the tracking chambers. The field was parameterised using polynomial fits to an accuracy of better than 0.5% everywhere[29]. The non-uniformity of the solenoidal field at the ends was counteracted by two compensating coils mounted symmetrically about the beam axis. The uniformity of the field allowed circle fits to be used in track finding algorithms.

2.4.2 The Beam Pipe (BP)

The beam pipe at the TASSO intersection was a cylindrical aluminium vacuum pipe 13 cm in radius. There were baffles at $\pm$50 cm from the nomiminal intersection point in order to minimise background from off-axis particles and synchrotron radiation.

2.4.3 Beam Pipe Counters (BPC)

Four 0.5 cm thick quadrant scintillation counters were wrapped around the beam pipe. They had a sensitive length of 75 cm in the $\pm z$ direction. The ends of each counter were viewed by 56 AVP photomultiplier tubes. A coincidence of the discriminated and stretched signals of these counters

was used as a component in the trigger during 1979. This was later removed from the trigger as the counters performed inefficiently in a high machine background environment and thus had little power to select good events.

2.4.4 Central Proportional Chamber (CPC)[30]

The Central Proportional Chamber (CPC) consisted of 5 concentric cylindrical shells of low mass expanded styrofoam. The chamber was 170 cm in length with inner and outer radii at 18 and 29 cm respectively. The proportional gaps were 1.6 cm wide and each had 480 anode wires strung parallel to the beam axis. Copper cathode strips were etched against the inner and outer walls of the gaps. They were helically wound with opposite rotational senses at an angle of 36.5 degrees to the beam axis. Each layer had 120 cathode strips which could provide z coordinate information on tracks passing through the chamber. The chamber was filled and flushed with 'magic gas', a mixture of Argon, Methylal, Isobutane and Freon 13b1. The chamber was operated with the anodes grounded and the cathodes at -4 KV. The chamber anode wires were readout using single hit electronics. The pattern of anode hits was fed to a fast microprocessing unit which formed associations of hits to detect tracks. This information was used for the charged particle trigger as described in Chapter 4.

2.4.5 Synchrotron radiation Shield

During 1980 there was a 2.6 mm metal shield between the CPC and the Drift Chamber. It was constructed by interleaving layers of tin and aluminium sheet and covered 60% of the solid angle in the x-y plane. Its purpose was the reduction of background from soft synchrotron radiation photons entering the Drift Chamber.

2.4.6 Drift Chamber (DC)[31]

This chamber consisted of 15 layers of drift cells, 9 with sense wires parallel to the beam (0 degree wires), and 6 with wires strung at approximately 4.5 degrees to the beam line (α wires). The α wires followed the generating lines of rotational hyperboloids. All drift cells were of the same size with 72 forming the innermost layer and 240 the outermost layer. This permitted a common operating voltage and the use of a common drift velocity for preliminary trackfinding. Each cell had 1 sense wire and 6 field wires. The sense wires were 30 micron gold plated tungsten and the potential wires were 120 micron gold plated molybdenum. Initially a 90% Argon/10% Methane gas mixture was used. It was later changed to a 50% Argon/50% Ethane mixture to reduce the dark current in the chamber. The chamber was operated with the sense wires at a voltage of +1.85 KV and the field wires at -0.62 KV. The drift velocity relation in cells was determined by reconstructing cosmic ray tracks and was found to be approximately 2.5×10^{-5} m ns^{-1}

Single hit electronics were used in the readout. The signal was amplified then fanned out. One signal went to a TDC (time to digital convertor) to provide the drift time and hence position measurement. The rest of the signal was read into a fast track-finding processor for use in the trigger. The momentum resolution, dp_t, was measured as $0.02\times p_t^2$ (p_t in Gev) using identified muon pair events.

2.4. The Inner Time Of Flight (ITOF)

At a radius of 132 cm there was a cylindrical array of time of flight counters (ITOF). The 48 N.E. 110 (Nuclear Enterprise) scintillators which formed the array had length 390 cm, width 17 cm and a thickness of 2 cm. The scintillator attenuation length was about 2 metres. Each end of the scintillator was viewed by an RCA 8575 phototube. The signals from these were split and fed to a discriminator and ADC (analogue to digital convertor). The discriminator output was further divided and sent to stop

a TDC and to generate a logic pulse for trigger purposes. The start signal for the TDC's was an induced signal from the passing of the positron beam on a capacitative probe placed 7.1 metres from the intersection region. The ADC information allowed a correction to be made to the TDC reading for pulse height slewing effects. The array was calibrated using light signals from a common spark gap and light fibre system. The time resolution was determined by looking at selected Bhabha events to be 450 ps.

The signal from the ITOF was used in the trigger. A coincidence of the pulse stretched signals from tubes at either end of a scintillator, set a hardware logic bit known as the ITOF mean timer bit. This was used with signals from the DC and CPC processors to define a 'trigger track'.

2.4.8 Liquid Argon Barrel shower Counters (LABC)[32]

The TASSO experiment design includes 2 large volume, good resolution liquid Argon shower counters to cover the upper and lower regions immediately outside the magnet coil. For the data period of this thesis, only the upper module was installed. This covered the angular range $42^0 < \theta < 138^0$ and $30^0 < \phi < 150^0$ and its front face was 179 cm from the interaction point. The LABC consisted of stacks of 2 mm thick lead sheets seperated by 5 mm gaps which were filled with liquid Argon. The stacks were oriented to point directly to the interaction point. Lead plates were maintained at high voltages and served both to initiate the development of electromagnetic showers and as electrodes for the collection of charged particles. The liquid Argon gaps acted as ionisation chambers. Liquid Argon was chosen as a suitable medium as it has a high density and a larger ionisataion loss, $\frac{dE}{dx}$, coefficient than a gas, has a suitable drift velocity for charged particles and it causes little quenching of the shower. The lead plates of the 6.1 radiation lengths nearest the interaction point were 7×7 cm squares and formed the front towers. The remaining 7.6 radiation lengths were 14×14 cm squares

and formed the back towers. Four front towers preceded each back tower. Precise position measurements were possible using several layers of 2 cm wide electrode strips which were interspersed in the first 3.1 radiation lengths of the front towers. Strips were oriented either parallel to the beam axis (ϕ strips) or orthogonal to it (z strips). The first 2 layers of z strips provided an ionisation loss, $\frac{dE}{dx}$, measurement for charged hadrons. In a test beam setup, which did not simulate the 1.6 radiation lengths of material which preceded the counter in the experiment, a root mean square energy resolution of $\frac{0.09}{\sqrt{E}}$ was measured for electrons with incident energy $E>0.8$ Gev. The angular resolution for reconstructing showering particles is estimated to better than 6 mrad for photons or electrons with energy ,E, >1 Gev.

2.4.9 The Hadron Arm TOF (HTOF)[33]

The HTOF consisted of 48 counters each of lenghth 240 cm, width 33 cm and thickness 2 cm. EMI 9807B phototubes were used to view each end of the scintillator and their signals were fanned out to a timing arrangement similar to that used for the ITOF. The HTOF was not used in the trigger. The distance from the interaction point was about 6 metres. This greater distance allowed particle separation to higher momenta than the ITOF but the extra material in front of the counters created difficulties and ambiguities in tracking particles from the Drift Chamber to this array. The time resolution estimated using selected Bhabha events was 450 ps.

2.4.10 Lead Scintillator Hadron Arm Shower Counters (HASC)[34]

In the original experimental design these counters were to be placed in the Hadron Arms of the detector. However due to delays in the construction of the more complex liquid Argon counters some were placed in the Central Detector positions of the liquid Argon counters. The author had particular involvement in the construction and operation of these counters and therefore the details of their design, construction, testing

and use is the subject of Chapter 3.

2.4.11 Muon Chambers[35]

The muon identifying system consisted of arrays of proportional tube counters behind iron absorbers. 6 large arrays were mounted around the magnet yoke using it as an iron filter and each Hadron Arm had a large array preceded by an 80 cm thick iron wall. The aluminium tubes of the arrays were 4 cm square section and ranged in length from 1.8 m to 8 m. A 50 micron tungsten wire threaded centrally down the tube length was held at a potential of 2.5 KV while the tube was filled and slowly flushed with a 90% Methane/10% Argon gas mixture. Each array had 4 planes of tubes. The wires of the lower two went in the orthogonal direction to those of the upper two planes. Planes with a common direction were offset by half a tube width to achieve a rms (root mean square) position resolution of 6 mm.

Charged particles tracked into an array were declared to be muons if 3 of the 4 planes gave a common hit position within 3 standard deviations of the Drift Chamber track extrapolation, taking into account the multiple scattering ellipse of the track. From study of cosmic ray muons the detection efficiency for muons of momenta greater than 1 Gev is 99%.

2.4.12 Luminosity Monitor[36]

The luminosity was measured by a counter system designed to detect Bhabha scattered events at angles around 50 mrad. At this angle the event rate is high and momentum transfers are small, space-like and well described by QED.

Figure 2.3 shows the Forward Detector layout. The counters were arranged in 8 identical arms with 4 arms either side of the interaction region. The system was symmetric in the horizontal and vertical planes ensuring that the sum of the counting rates for Bhabha events was, to first order, insensitive to small displacements of the interaction

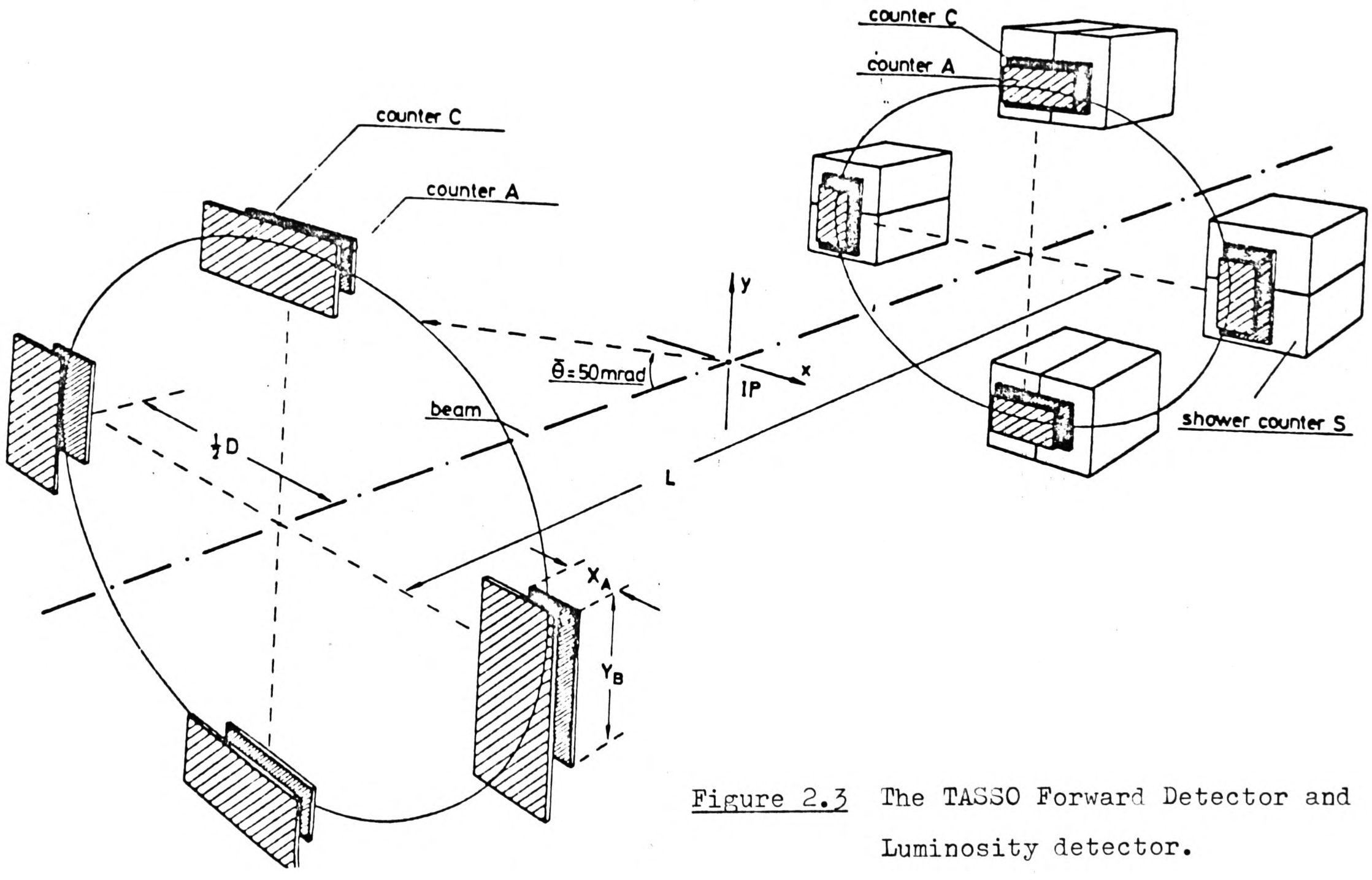

Figure 2.3 The TASSO Forward Detector and Luminosity detector.

point[37]. Each arm consisted of 2 plastic scintillator counters, a small one which defined the acceptance, A, and a larger coincidence counter, C, followed by a Lead-Glass Shower counter, S. A Bhabha event signature was a signal from one A counter in coincidence with the diametrically opposite C counter and large energy deposits in the corresponding shower counters. The geometrical acceptance of the detector was 1.4×10^{-4} steradians and this gave a 1 Hz counting rate at a beam energy of 15 Gev and a luminosity of $10^{31}cm^{-2}\ s^{-1}$. The final luminosity was determined after correcting for radiative effects to order α^3, false triggers of A or C counters caused by shower debris backscattered from the shower counters, and acceptance losses due to the complicated motion of the electrons in the end field and material of the solenoid. The final values were assigned a systematic uncertainty of 4% [38].

CHAPTER 3

Hadron Arm Shower Counters (HASC)

3.1 Introduction

This Chapter describes the design, manufacture, testing and operation of the Lead/Scintillator shower counters built for the Hadron Arms of the TASSO detector. The author was involved at all stages of this process apart from the initial design which was due G. Mickenberg[39].

A good resolution electromagnetic shower detector covering as large a solid angle as possible was desirable in the TASSO detector because much of the final state energy emerges as electrons or photons. QED reactions such as Bhabha scattering involve only electrons and photons while for annihilations producing hadrons about a third of the energy is expected to be in neutral pions which decay to photons. Specifically it was proposed to use the HASC to compare neutral and charged energy flows in jet-like events, to try to reconstruct neutral pions and to identify electrons with an energy greater than 4 Gev (below this energy they are identified using Aerogel Cerenkov counters).

3.2 Counter Design

The principal constraints on the design of the Hadron Arm shower counters were the necessity to integrate them in the Hadron Arm structure and the need for them to be relatively cheap while achieving a reasonable

energy resolution (dE = 0.2E for high energy photons of energy E) and a position resolution compatible with the Cerenkov counters (0.019 steradians). The design finally adopted was for a lead/scintillator sandwich counter utilising low cost acrylic scintillator and a simple light detecting system using wavelength shifter materials[40],[41].

The Hadron Arm shower counters consisted of 64 identical mechanical units. Each Hadron Arm was to take 32 units. The counters destined for the North arm were assembled by the DESY group on the DESY site. The counters for the South Hadron Arm were built collaboratively by Oxford, Rutherford Laboratory and Imperial College at Oxford Nuclear Physics Laboratory. Each mechanical unit was a rectangular box of dimension 142 x 100 x 20 cm as shown in Figure 3.1. The boxes were made from 5 mm steel plates which were welded together. On the bottom plate and the middle shelf of each box there were 2 stacks of acrylic scintillator sheets interleaved with lead sheets. Each stack had lateral dimensions of 68 x 48 cm and contained 9 acrylic scintillator sheets (plexiglass doped with 3% naphthalene, 1% butyl PBD and 0.01% POPOP[42]), each 10 mm thick, and 8 lead sheets, each 5 mm thick. The lead and scintillator were seperated by sheets of mylar and aluminium foil. The ionisation from showers initiated in the lead was converted to light in the scintillator and some was radiated or reflected to the gap between the 2 stacks. In this gap were sheets of wavelength shifter bar which were used with light guides to redirect the light to a phototube mounted on the face of the box. The counter design was such that if light from a single stack were sampled by a single tube the position resolution was the same as that of a Cerenkov cell. However due to economic constraints the majority of counters had 1 phototube to sample the light from 2 adjacent stacks of material. The wavelength shifter bars were 10 mm thick and consisted of Plexiglass doped with 120 mg l^{-1} of BBQ[43]. They absorbed the ultraviolet scintillator light, which had an attenuation length of a few centimetres, and isotropically reradiated it in the green part of the

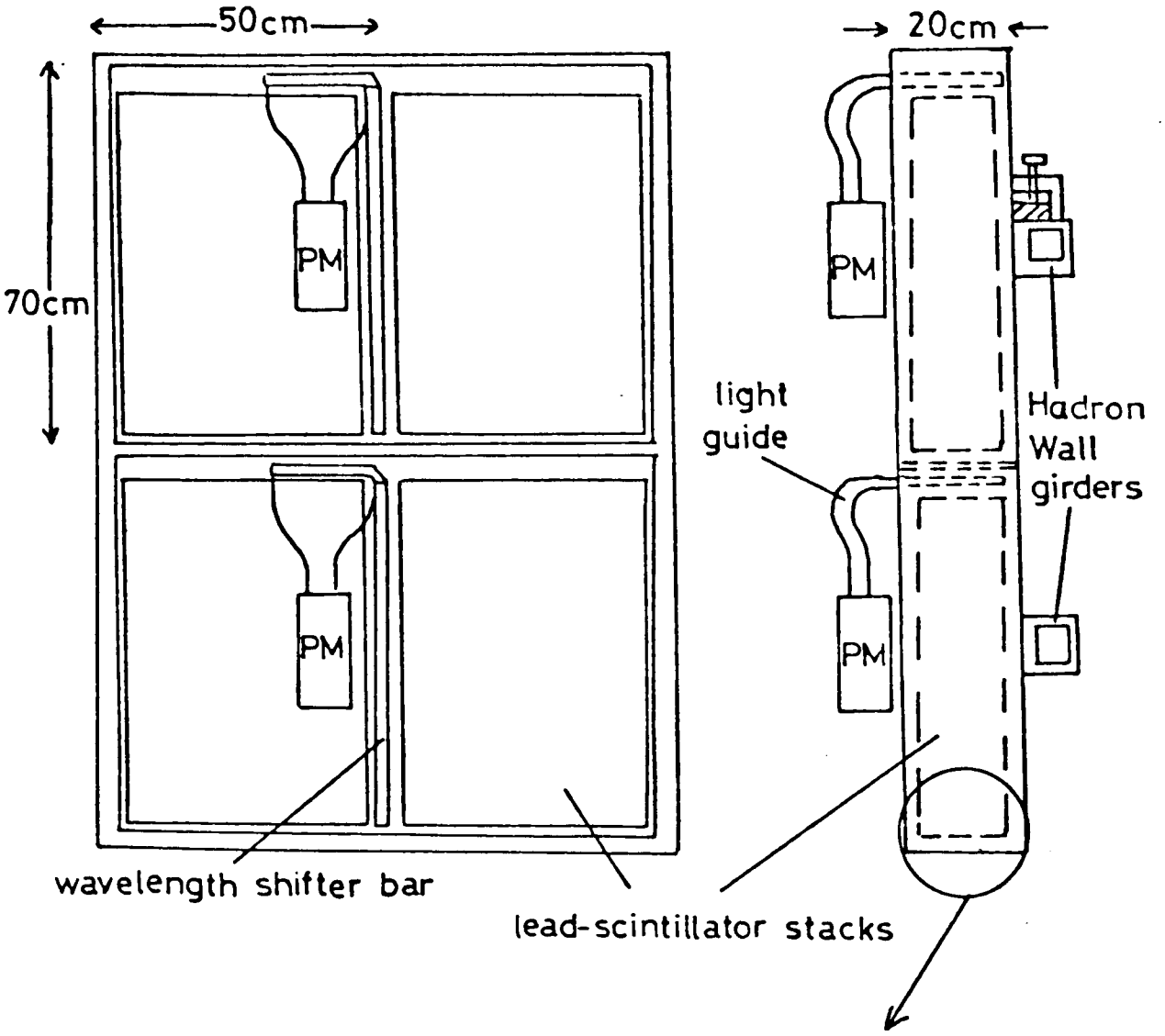

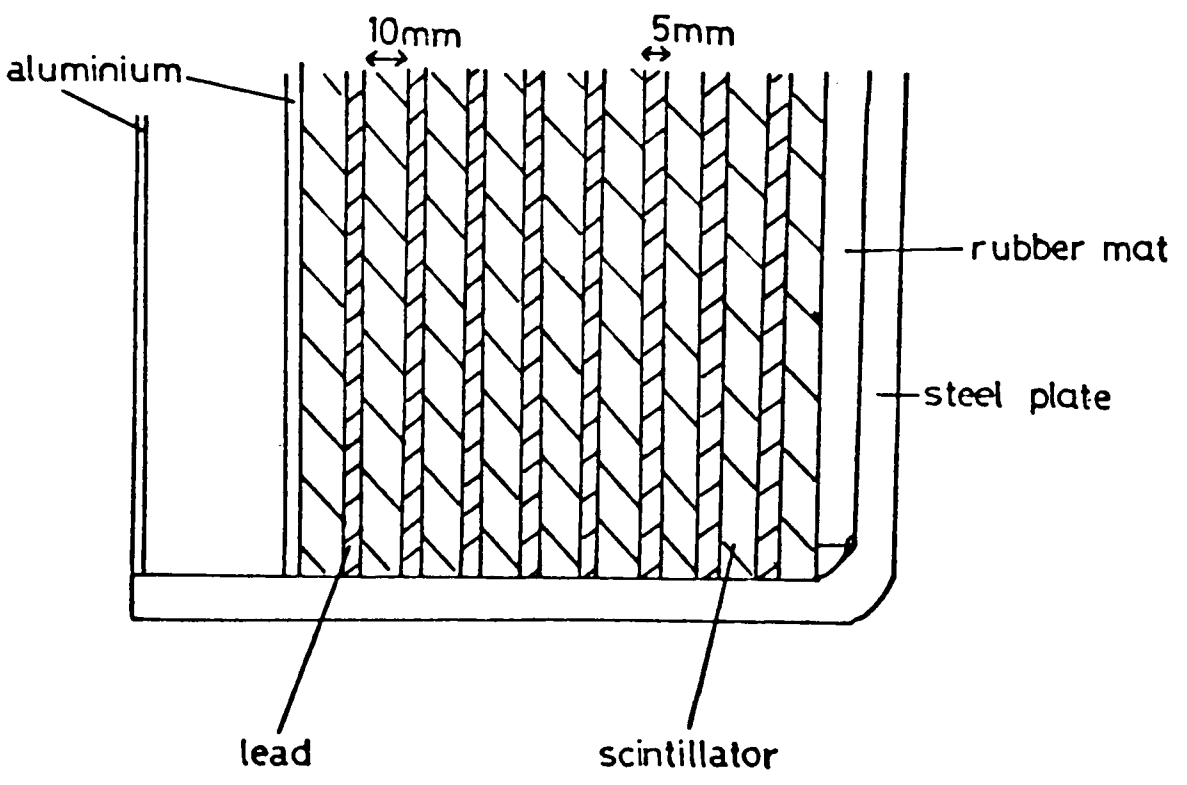

Figure 3.1 Design of the TASSO lead/scintillator shower counters.

spectrum where it had an attenuation length of about two metres. The lower end of the wavelength shifter bar was terminated by an aluminised mylar mirror and the upper end was glued to a light guide which had 2 prism faces in series to reflect light upwards out of the flat plane of the counter. Both prism faces had aluminised mylar mirrors in loose optical contact with them. As light from the end of the wavelength shifter bar furthest away from the phototube was attenuated approximately 30% more than that from the upper end, copper strips were inserted between the edges of the stack and the wavelength shifter bar, therby differentially blanking off controlled amounts of light. The strips were 1 cm wide and spaced at closer intervals in the region nearest the light guide. Test measurements illustrated the value of this technique. In the orthogonal direction no similar compensation for light attenuation in the scintillator could be made without a much more complex light collecting system. However white adhesive tape was stuck to the polished edge of the scintillator most distant from the wavelength shifter bar, in order to diffusely reflect some of the light back towards the centre of the counter. Reference (39) claims that this should increase the uniformity of response.

The North arm counters used 56 AVP photubes and bases from a earlier experiment. The South arm counters used 2 inch diameter EMI 9807B series phototubes. The phototube base design was optimised for linearity of response and to be compatible with a 2 mA current limit imposed by the use of LECROY 48 channel power supplies. The phototubes were rigidly clamped to the face of the steel boxes using drain pipe clamps, a slotted steel bar and some screw threaded 0.5 cm rod.

3.3 Counter Positions in the TASSO Experiment

The design proposal for the TASSO experiment envisaged the lead/scintillator counters as covering the solid angle of the Hadron Arms. However because construction of the Liquid Argon Barrel Counters (LABC)

was delayed some of the HASC's were moved to the central part of the experiment in order to increase their solid angle coverage. As LABC counters were completed the HASC's were moved to occupy their intended positions. Figures 3.2 and 3.3 show the counter positions for the data periods covered by this thesis.

The counters can be blocked into 7 large groups. Throughout the rest of this Chapter each group will be referred to by a one or two letter mnemonic which refers to the relative position of the group in the apparatus i.e. US means the group in the upper southmost section of the Central Detector.

3.4 HASC Readout

The signals from the phototubes of the HASC's were readout along 28 metre lengths of coaxial cable. The signals from groups N, LN and LC were readout to racks of electronics on the North Hadron Arm of the apparatus. The signals from groups S, UN, US and LS were taken to the electronic racks of the South Hadron Arm. Each signal was then divided into 2 approximately equal parts. One half of the signal was fed to the input of a Lecroy 2282 ADC module. The full scale of this ADC was 4000 channels which corresponded to 1×10^{-9} Coulombs. The ADC had the facility to automatically subtract pedestal values but for the data period of interest pedestal subtraction was done offline from sets of pedestal values taken at the start of real data taking runs. For data events the ADC modules were gated for 220 ns. The pulse length from the HASC phototubes was typically 60 ns but the longer time was necessary as the ADC modules were also used in the readout of the Cerenkov counters.

The second half of each phototube signal was fed to a linear fan in module. This summed the outputs from the various groups of counters so that several electromagnetic shower energy triggers could be constructed.

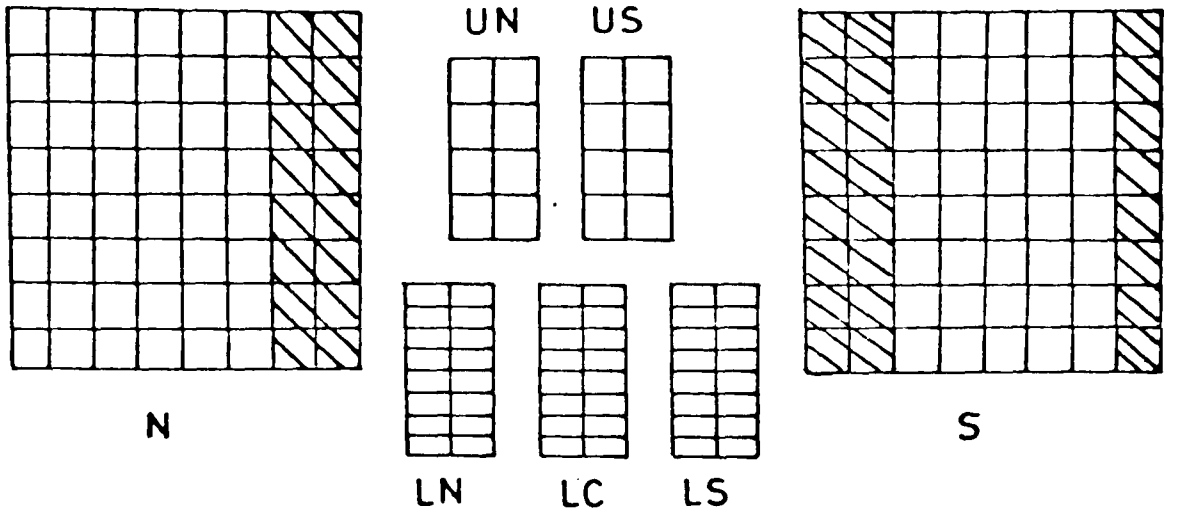

(a) Plan view. Shaded positions indicate areas not occupied by HASC.

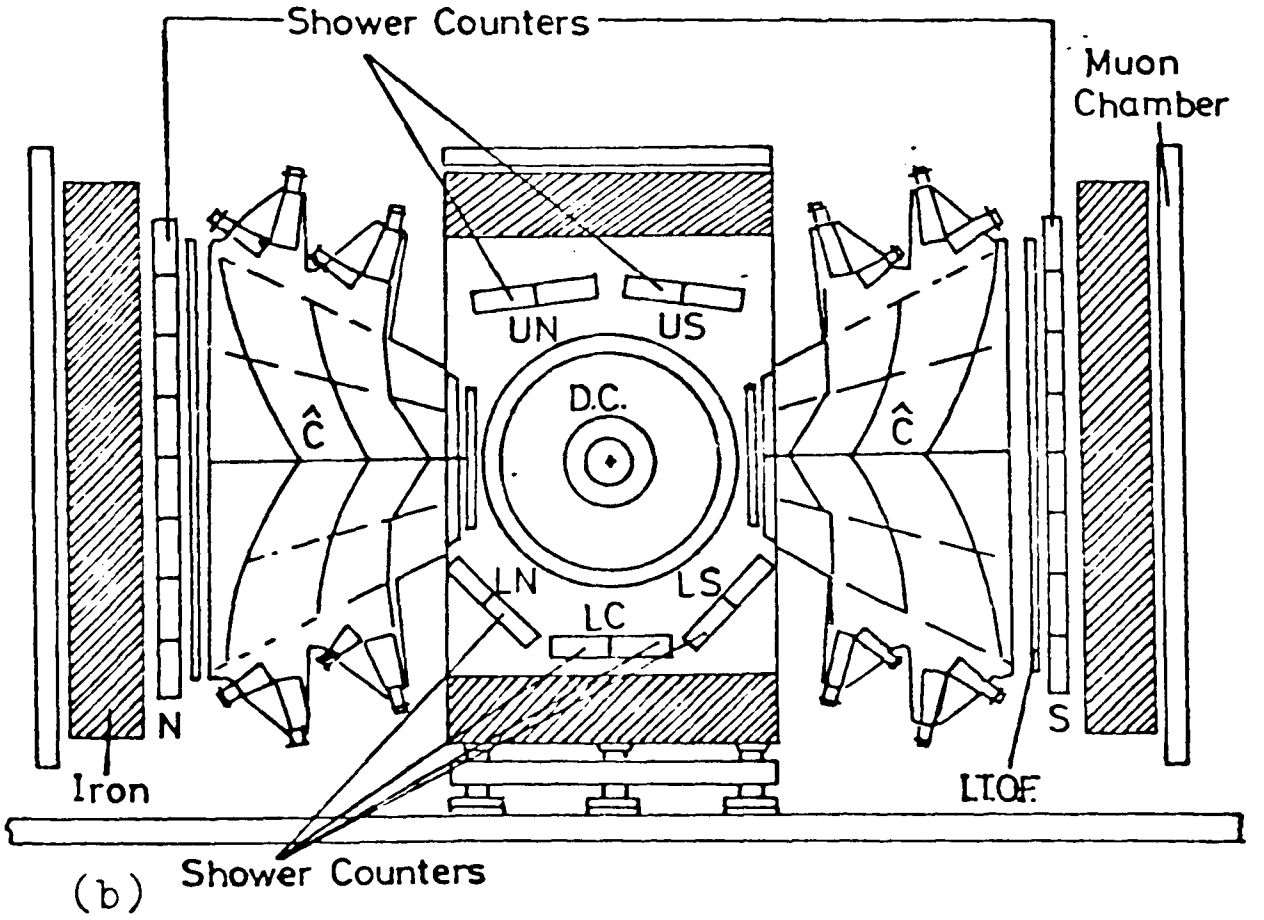

(b)

Figure 3.2 Positions of the HASC during 1979.

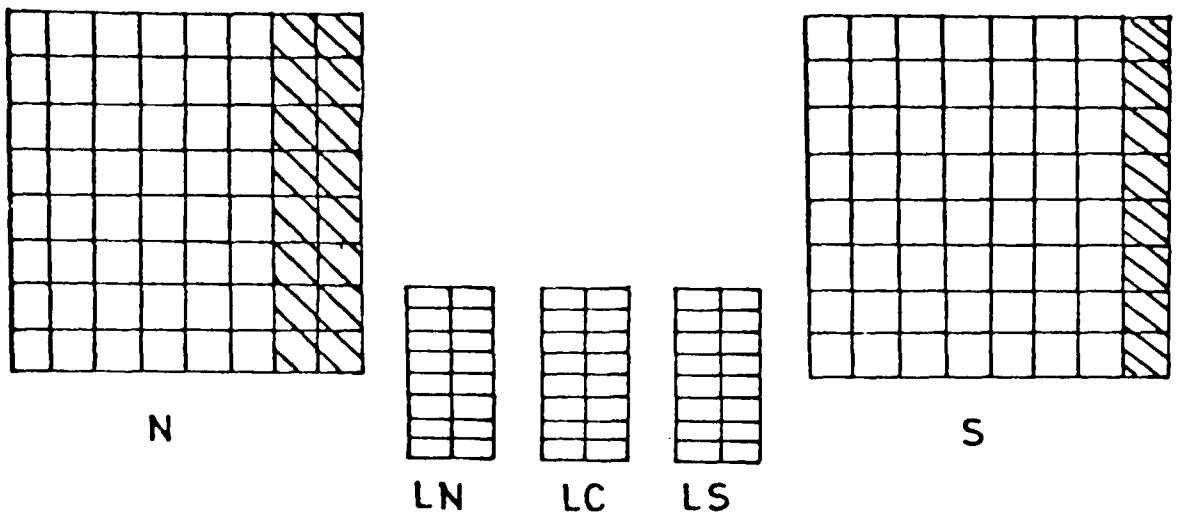

(a) Plan view. Shaded positions indicate areas not occupied by HASC.

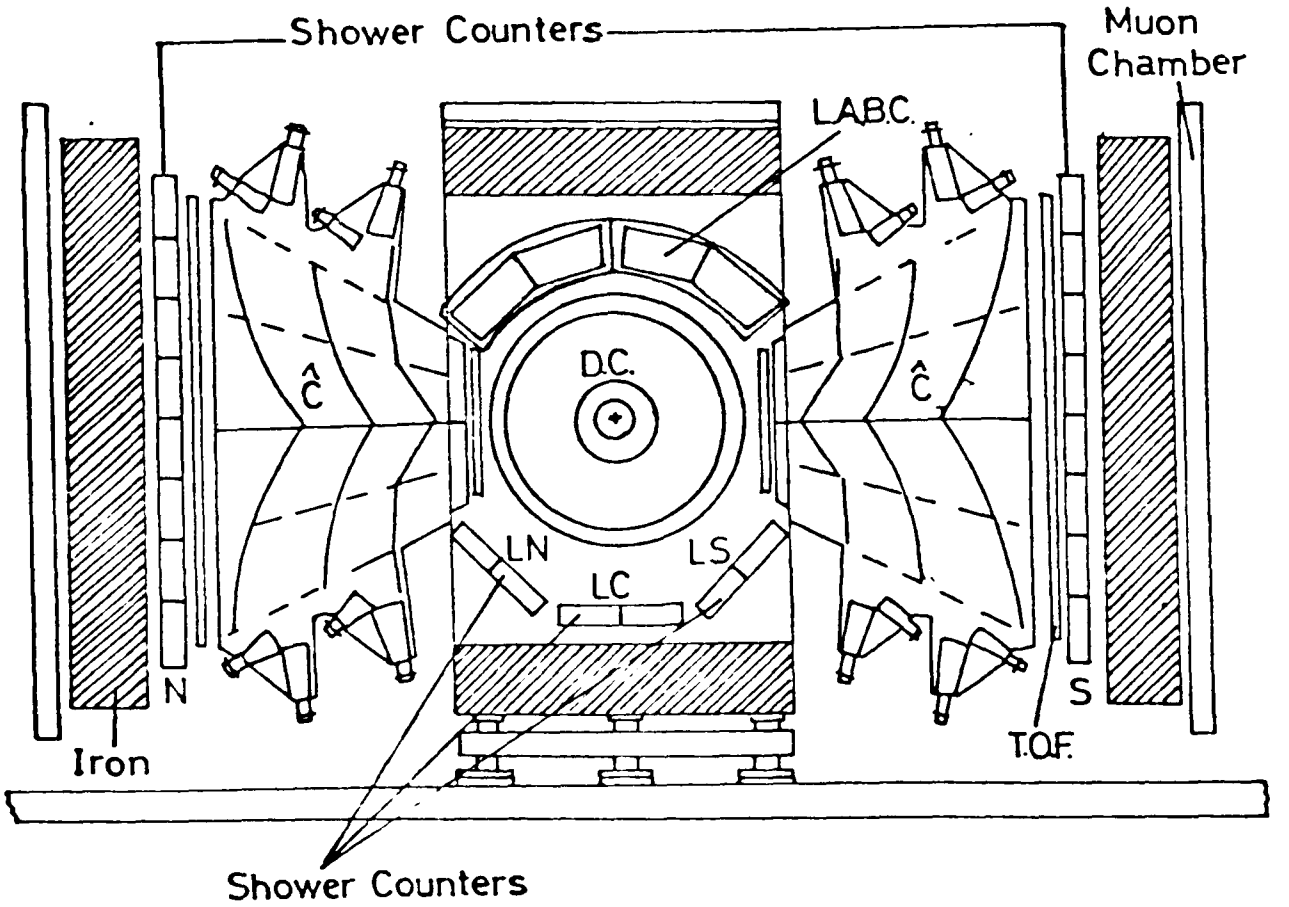

(b)

Figure 3.3 Positions of the HASC during 1980.

3.5 Shower Counter Triggers

The summed signal from a group of shower counters was fed to several discrimator units, to derive logic signals for input into the trigger decision box of the experiment (the SIGH box which is mentioned in Chapter 4).

2 types of trigger were formed

a) Total energy trigger - used to collect samples of Bhabha and 2 real photon events. The following expressions detail the trigger configuration as it changed with time. Summation of the outputs of several groups of counters is represented by a + sign. These combinations were then discrimated and the logical outputs of this process were used as indicated by the AND and OR statements to make a binary trigger decision..

for data collected in 1979

((US + UN) AND LS) OR ((S+LN+LC) AND (UN+US+LS+S))

for data collected in 1980

(N AND S) OR (LN+LC) OR LN

The energy threshold set for each group or sum of several groups was approximately 3 Gev for beam energies above 10 Gev.

b) Shower energy + 1 track trigger - this was used for low multiplicity events i.e. taus, 2γ events.

for data collected in 1979

((UN+US+LS+S) AND 1 prepro track) OR ((N+LN+LC) AND 1 prepro track)

for data collected in 1980

((S+LS) AND 1 prepro track) OR ((N+LN+LC) AND 1 prepro track)

The energy threshold set for each group or sum of groups was approximately 800 Mev of shower energy.

3.6 Shower Counter Testing

3.6.1 Cosmic Ray tests

After construction at Oxford and before transport to DESY the performance of each shower counter was tested using the experimental setup of Figure 3.4. The counter under test weighing approximately 750 Kg was elevated several feet off the ground on a special bogie and track. It was sandwiched between 2 scintillator planes, the lower being shielded by 5 cm of lead. These scintillators were used to identify penetrating cosmic ray muons. Above the counter were 2 orthogonal planes of proportional tubes of the type used in the muon detecting arrays of the TASSO detector. These tubes were used to accurately define the position at which the cosmic ray muon penetrated the shower counter and thus the response of the counter could be mapped over its full area. The trigger signals, the muon tube signals and the readout of the shower counter phototube was done using standard CAMAC interfaces to a NOVA minicomputer. For analysis purposes the area of the shower counter stack was divided into 10×10 cm squares and the response from cosmic rays projected onto this area was integrated. Typically 40000 cosmic muon triggers were taken per hour. Of these 10000 were acceptable vertical tracks and used for analysis. To collect reasonable statistics data was collected for 8 hour periods.

The results of a typical shower counter muon test is shown in Figure 3.5. Assuming Poisson statistics, the width of the ADC distribution indicates that 4-5 photoelectrons leave the photocathode of

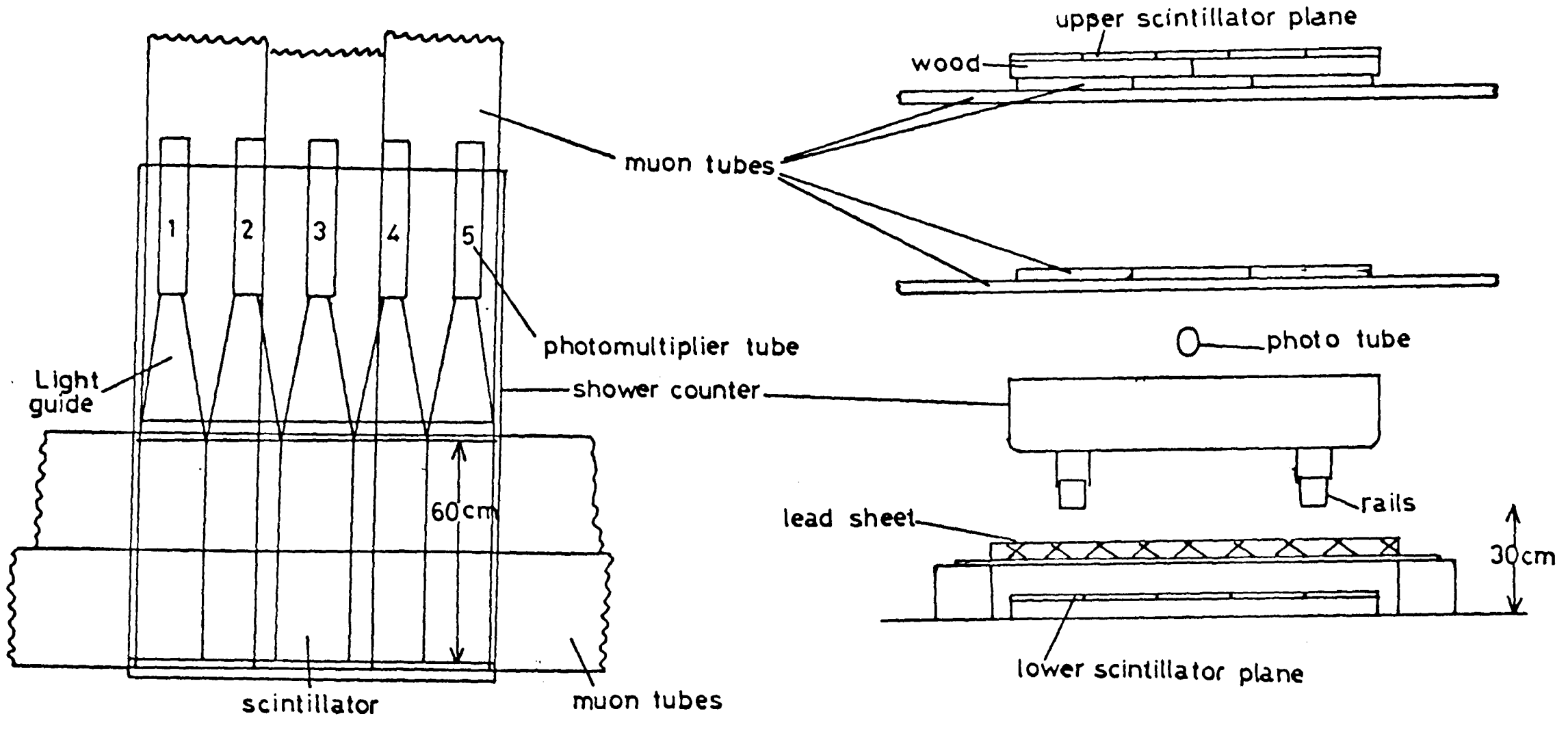

Figure 3.4 Test setup used at Oxford to measure HASC responce to cosmic ray muons.

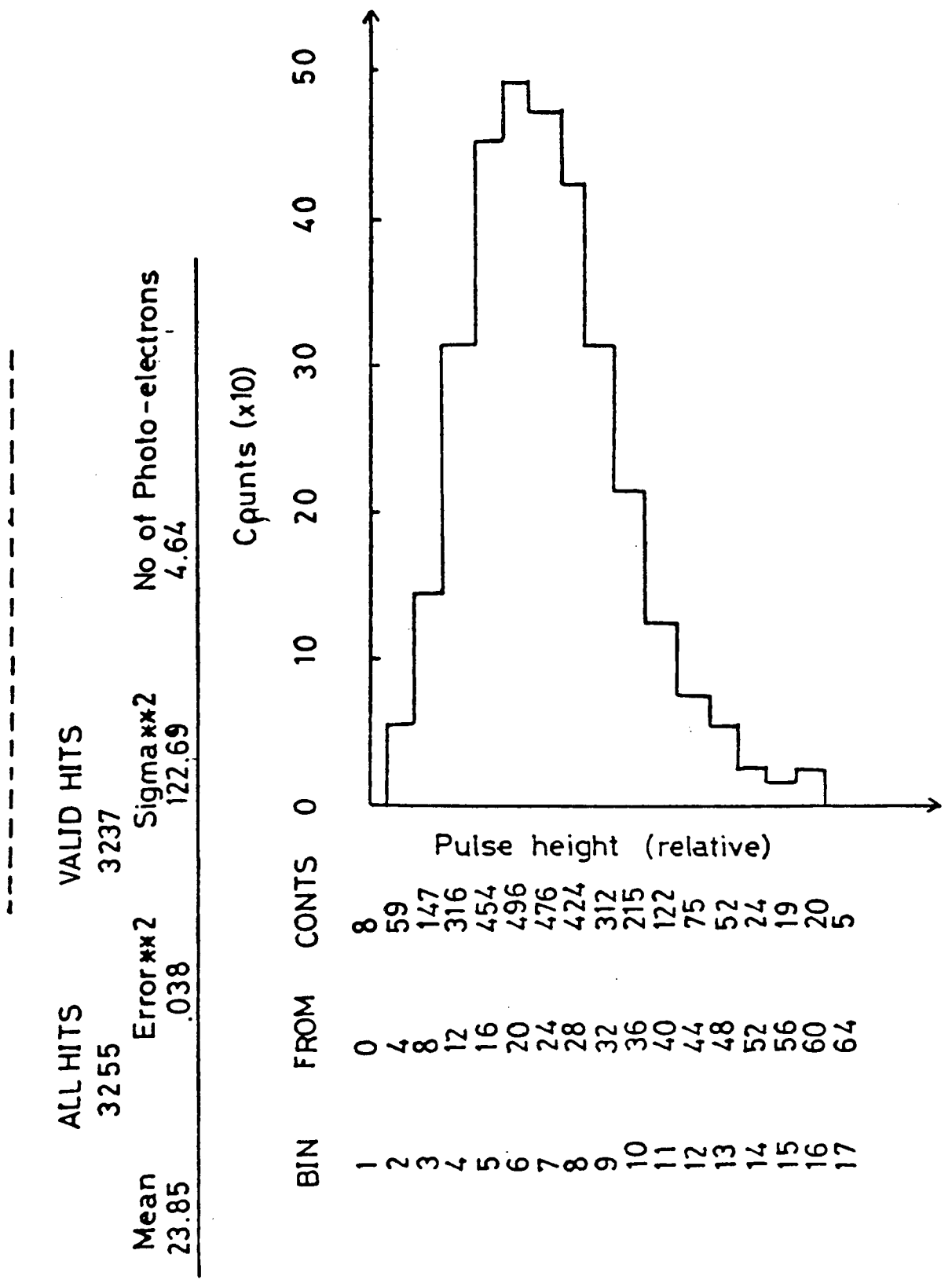

Figure 3.5 Histogram of pulse height response when cosmic rays hit a HASC. This test used the setup of Figure 3.4.

the phototube for a minimum ionising particle. The effects of light attenuation in the wavelength shifter bar and the scintillator can be clearly seen by taking slices of data as in Figure 3.6. The effect of the copper blanking strips reduces a 30% variation to 10% or less.

3.6.2 Electron Beam Tests

Several shower counters were tested by placing them in a monoenergetic test beam of electrons parasitically derived from the DESY accelerator at DESY. The energy of beam supplied was variable up to a maximum energy of 4 Gev. The beam was collimated to have dimensions of a few centimetres at the counter face. The counter response was mapped by mounting it on a platform which could be driven both sideways and vertically. An extra 5 mm lead sheet was positioned in front of the counter to simulate the material in front of the counters in the TASSO environment.

The response of the counter to electrons is shown in Figure 3.6. It can be seen that it is qualitatively similar to the results of the cosmic ray analyses performed using the Oxford experimental setup. The energy resolution for electrons was measured from the full width at half maximum values of the ADC distributions and found to be approximately 20% at 4 Gev.

3.7 Calibration and performance of the Shower Counter Array

In order to convert the response of a phototube signal from a counter to the physical energy of a particle it was necessary to monitor the gain of the phototubes of the array. This was possible in 2 ways :

1./ Online calibration - This was achieved by illuminating each tube of the array with light of equal intensity. The light was supplied via thin optical fibres[44] which were uniformly illuminated by a Xenon flash lamp[45].

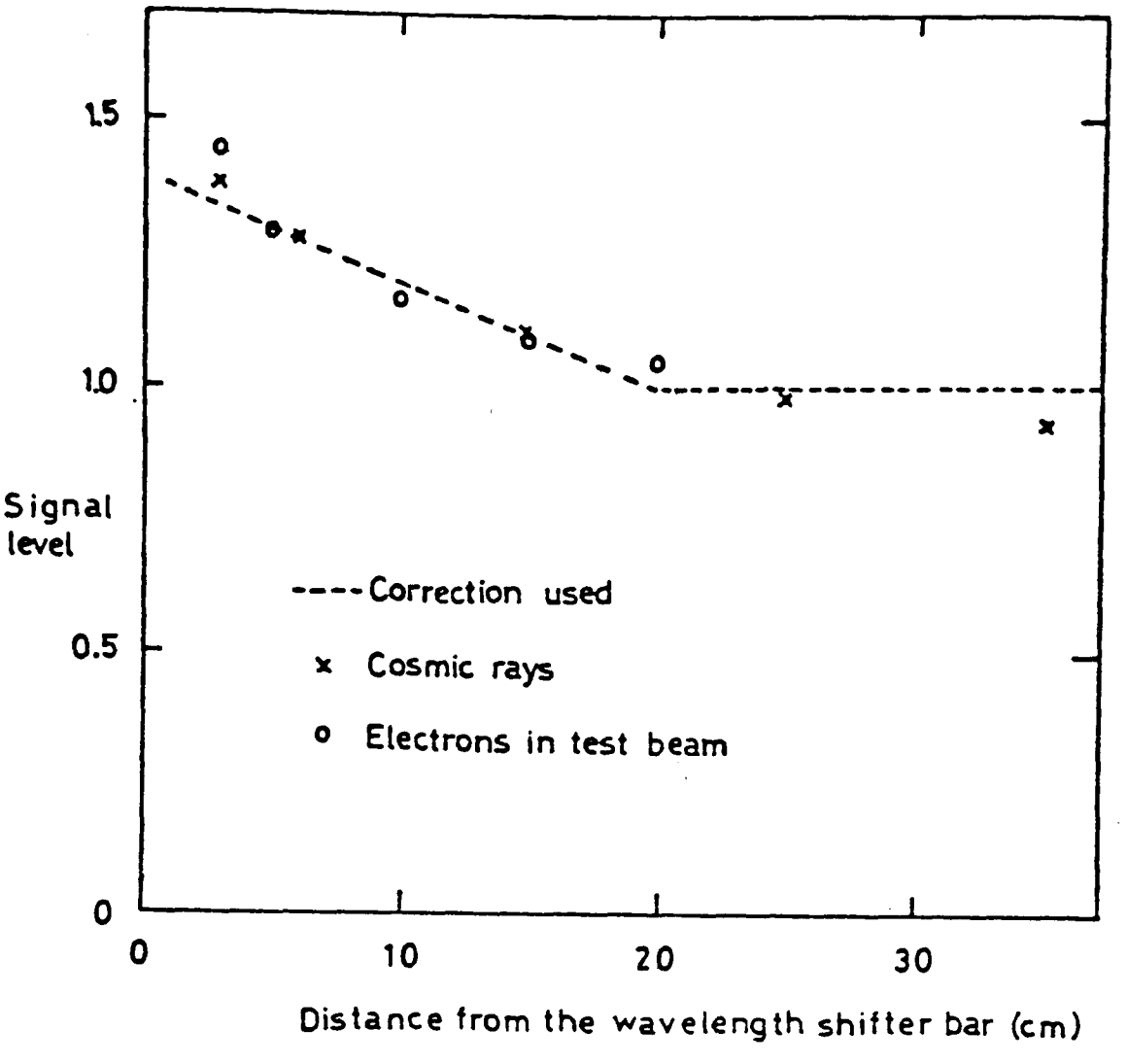

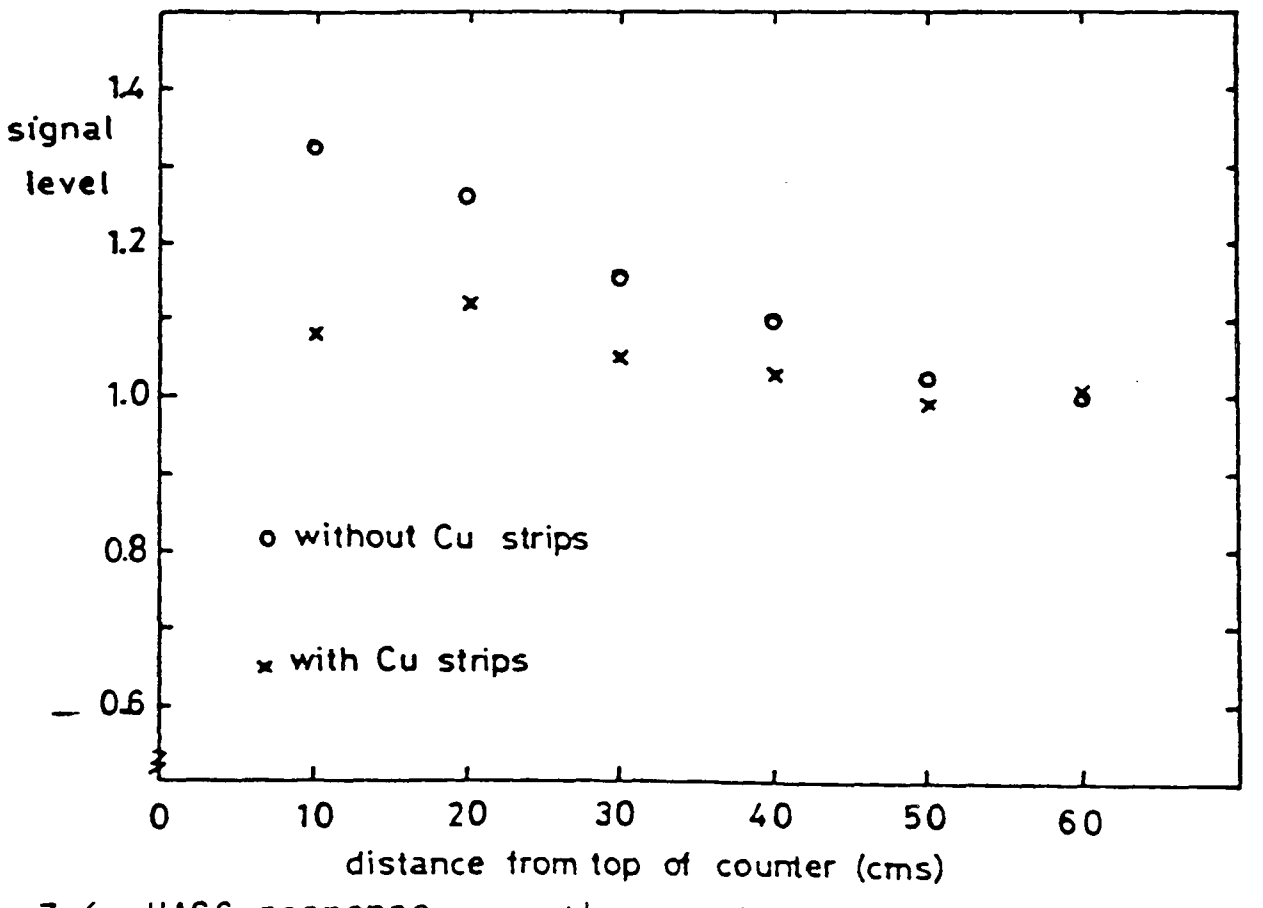

Figure 3.6 HASC response over the counter area.

The lower diagram shows the effect of copper blanking strips.

The upper shows the hit position correction used for tracks.

2./ Offline calibration - well defined non-radiating Bhabha events selected using strict cuts on track information afforded an approximately monoenergetic sample of electrons with energy equal to the beam energy.

3.7.1 Online calibration procedures

Groups of counters were intercalibrated by simultaneously illuminating them with light of the same intensity. This was done using bundles of thin optical fibres. One end of a bundle was illuminated uniformly by light from a Xenon flash lamp and individual fibres from the bundle were led to different counters. The fibre bundles varied in length from 1.8 to 12 metres and each individual fibre was of 0.5 mm diameter. A black PVC coating protected the fibre from physical damage. The individual ends of fibres terminated in a robust optical coupler and this was placed in a perspex holder glued to the top and half way down the length of a tubes wavelength shifter bar. This ensured that most of the optical path that light from the lead/scintillator stacks traversed was tested, using light of a similar spectral quality as that from the interaction of a real particle. The fibres were guaranteed to give outputs which were the same to a tolerance of 1% if the common end was illuminated uniformly and the fibres were placed straight and flat. The JADE group[46] at PETRA used identical fibres in the optical calibration system of their large lead glass array and showed in tests that the fibre output was not degraded seriously by loops with radii of curvature greater than 20 cm. Care was taken to introduce no severe loops.

Three Xenon lamps were used in the calibration system. They had 5 electrodes and were used as free running relaxation oscillators with the light being derived from arcing of the fifth electrode. The lamp stability was studied under bench top conditions and determined to be constant to $\pm 1\%$ over a short period of a few hours and to be constant to within $\pm 5\%$ over a longer period of several months.

An approximate absolute calibration of the Xenon lamps was derived from the electron beam tests. This enabled the high voltages of the phototubes to be set so that a particle of beam energy gave approximately half the full scale reading of the ADC's.

Calibration runs of about 1000 Xenon lamp events were taken every 2 to 3 days. The phototube outputs were read into ADCs using a strobe derived from the lamp discharge. A program on the online NORD computer calculated the average change of all phototubes attached to a single lamp and ascribed this to a shift in the intensity of the lamp. After this was factored out the new absolute online calibration constants for each counter were written to a file on the NORD. This file was used to detect dramatic deteriorations in counter performance.

3.7.2 Offline Calibration procedures

After intercalibration of groups of counters using the Xenon lamp and optical fibres, the absolute energy calibration of the counters was checked by studying the energy distributions of Bhabha scattered electrons. The Bhabha events were collected on a charged track trigger and selected using charged track information on energy and acollinearity of 2 track events using the cuts described in Chapter 5.

Although Bhabha electrons should have energy equal to that of the beam, the HASC's are not expected to detect that full energy. This is because they are only about 8-9 radiation lengths of material and in terms of the typical extent of an electromagnetic shower this is rather thin. Thus quite a large fraction of the energy will emerge from the rear of the counter and this leakage will be a function of both the initial energy of the electron and the angle at which it hits the shower counter. These effects were studied using the E.G.S.[47] (Electron-Gamma Shower) Monte Carlo program which was developed by Ford and Nelson at SLAC. This program models, at the individual interaction level, the development of

electromagnetic showers in user specifiable materials and detector geometries. The frequency of fundamental interactions of particles in any material is determined from large data files compiled or extrapolated from experimental data. Photons are considered to undergo pair production, Compton scattering and photoelectric processes while electrons or positrons can interact via elastic Coulomb scattering off nucleii, inelastic scattering off atomic electrons, bremsstrahlung or positron annihilation. Appendix 2 describes some of the simple theory appropriate to the calculation of these process. The relevent interaction cross sections for photons are small and well behaved but the charged particle cross sections are larger and less well determined. However large cross section processes generally have low momentum transfers and therefore do not give large contributions to shower fluctuations and so can be well approximated by continuum results. The results produced by the EGS program for the development of an electromagnetic shower in a block of lead were compared with the standard shower tables of Messel and Crawford[48] and found to be in excellent agreement, as shown in Figure 3.7.

The lead and scintilator sheets of the HASC's, as well as the material in front of them, were simulated in the EGS Monte Carlo and the dependence of the energy deposited in the scintillator sheets as a function of the initial energy and angle of both photons and electrons was calculated. As expected photons showers develop more slowly than electron showers. Table 3.1 gives a summary of some of the main results. It is seen that even a 1 Gev photon has a quarter of its energy leaking out of the rear of the counter. Figure 3.8 shows the angular dependence of the energy deposited in the scintillator. These curves were used to produce a correction for particles hitting the counter. Firstly the energy seen was corrected to correspond to the energy expected to be seen if the particle was normally incident on the counter. This energy, E_0, was then corrected to account for leakage from the rear of the counter using

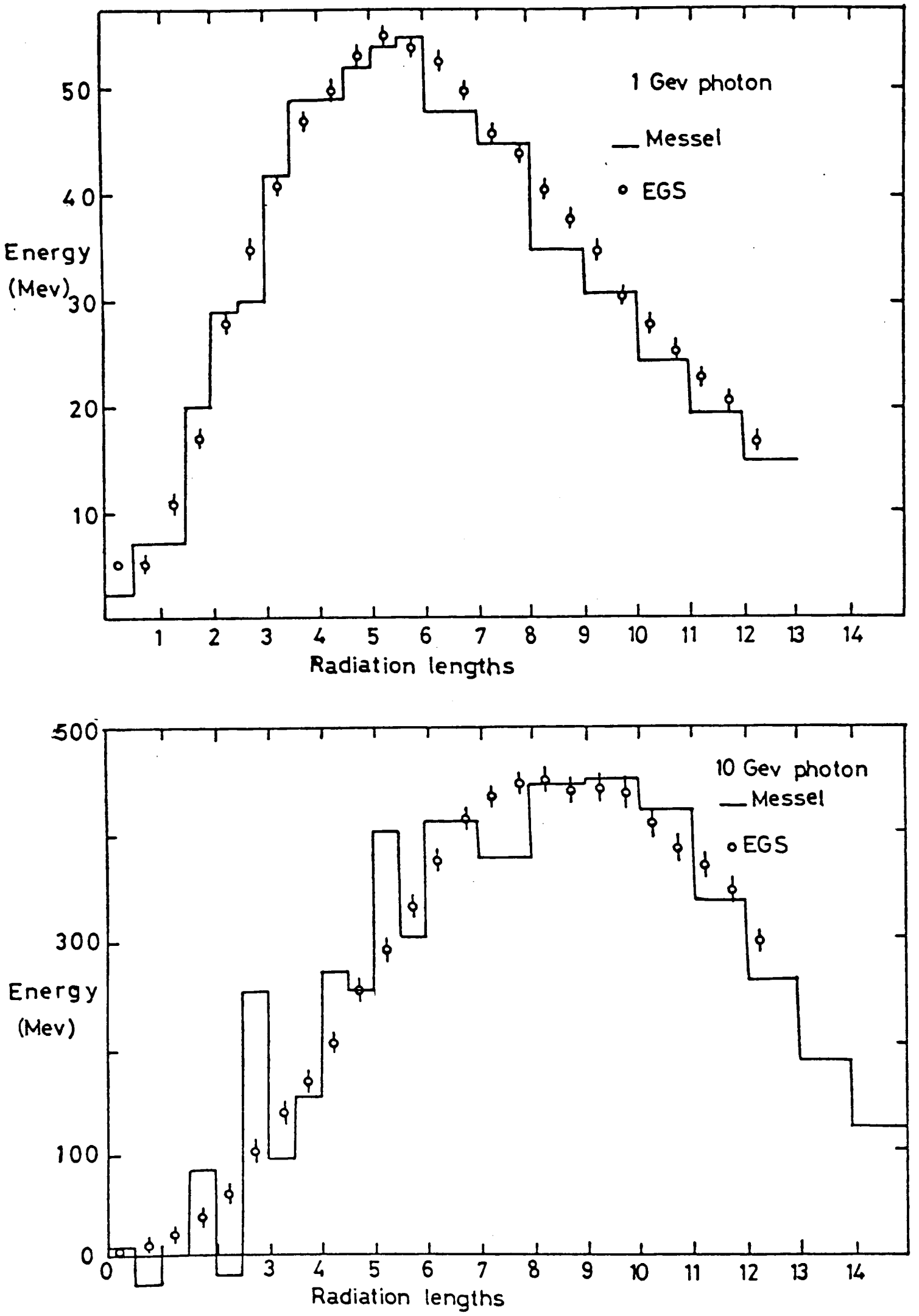

Figure 3.7 Comparison of E.G.S. with the shower tables of Messel and Crawford for the energy deposited in a lead block as a function of depth.

Energy of incident photon (Gev)	Angle of incidence of photon (degrees)	% Energy deposited in Pb	% Energy deposited in scintillator	% Energy emerging from rear of counter
1.0	0	58.2	10.5	27.0
	10	61.2	11.1	22.4
	40	66.1	11.5	13.4
5.0	0	47.9	9.0	41.0
	20	50.6	9.4	38.4
	40	61.9	11.1	24.4
10.0	0	43.6	8.14	47.4
	20	42.3	8.76	43.8
	40	60.7	10.9	26.8
15.0	0	43.3	7.7	51.0

Table 3.1 E.G.S results for HASC simulation.

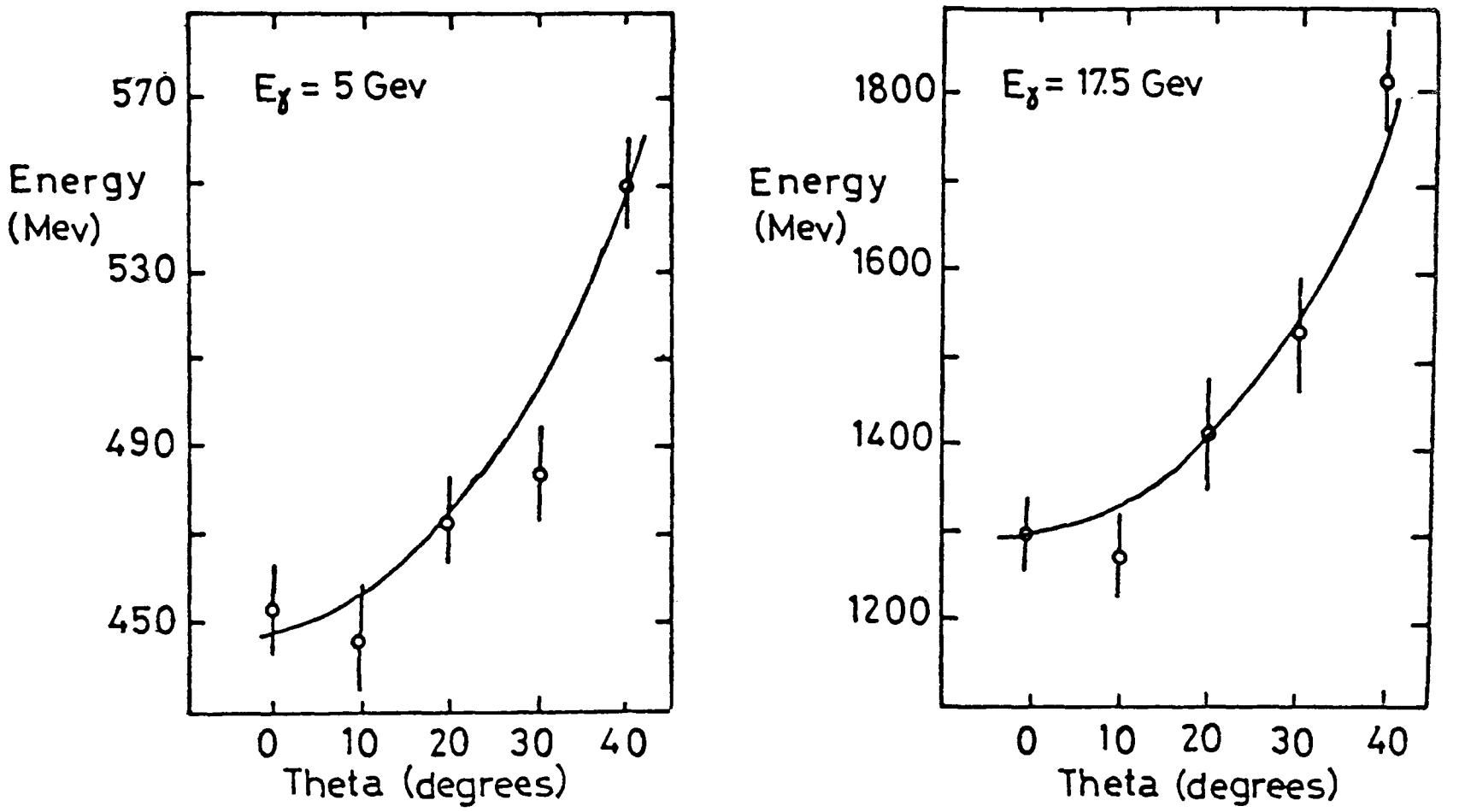

Figure 3.8 EGS prediction for the energy deposited by photons in the scintillator layers of the HASC as the angle of incidence of the photon is varied. The curve is a parameterised correction used to correct the data.

$$E_{corr} = E_0 + 0.02 \times E_0^2$$

where E_{corr} is the initial energy of the particle.

For charged particles it is also possible to make a correction for the distance of the projected hit of the particle from the wavelength shifter bar, using the curve of Figure 3.6 which was derived from electron beam tests.

For real data the distribution of the energy of Bhabha electrons incident on the counters of a particular group was studied after all these corrections had been applied. The deviation of the mean of such distributions from beam energy was used as a multiplicative factor to the calibration constants. Table 3.2 shows the results of this procedure over a period of a couple of months. It indicates that the initial online calibration was reasonably correct and that further corrections are relatively small ($< 10\%$). Figure 3.9 illustrates the corrected energy distribution of all counters after all corrections had been applied. The events at low values of energy deposited are due to Bhabha electrons being tracked into the wrong shower counter. The energy resolution indicated by this distribution is around 20%, which is in good agreement with the values from the test measurements.

The response of the counters to cosmic muons collected during data taking runs also provides a source of particles which deposit a known energy for calibration purposes. Figure 3.10 shows the energy deposited by such particles[49]. The mean energy is around 200 Mev, as expected for a minimum ionising particle. For the data period covered by this thesis no serious work using the cosmic muons as a calibration source was attempted.

Calibration number	Lamp 1 group	Lamp 2 group	Lamp 3 group
1	1.00	1.00	1.07
2	1.00	1.00	1.07
3	1.00	0.93	1.00
4	1.03	0.85	0.89
5	1.00	1.03	1.00
6	1.03	0.93	1.00
7	1.03	0.93	1.00

Table 3.2 Offline calibration factors derived from the mean of the deposited shower energy distribution of Bhabha tracks identified using tracking chamber and ITOF information.

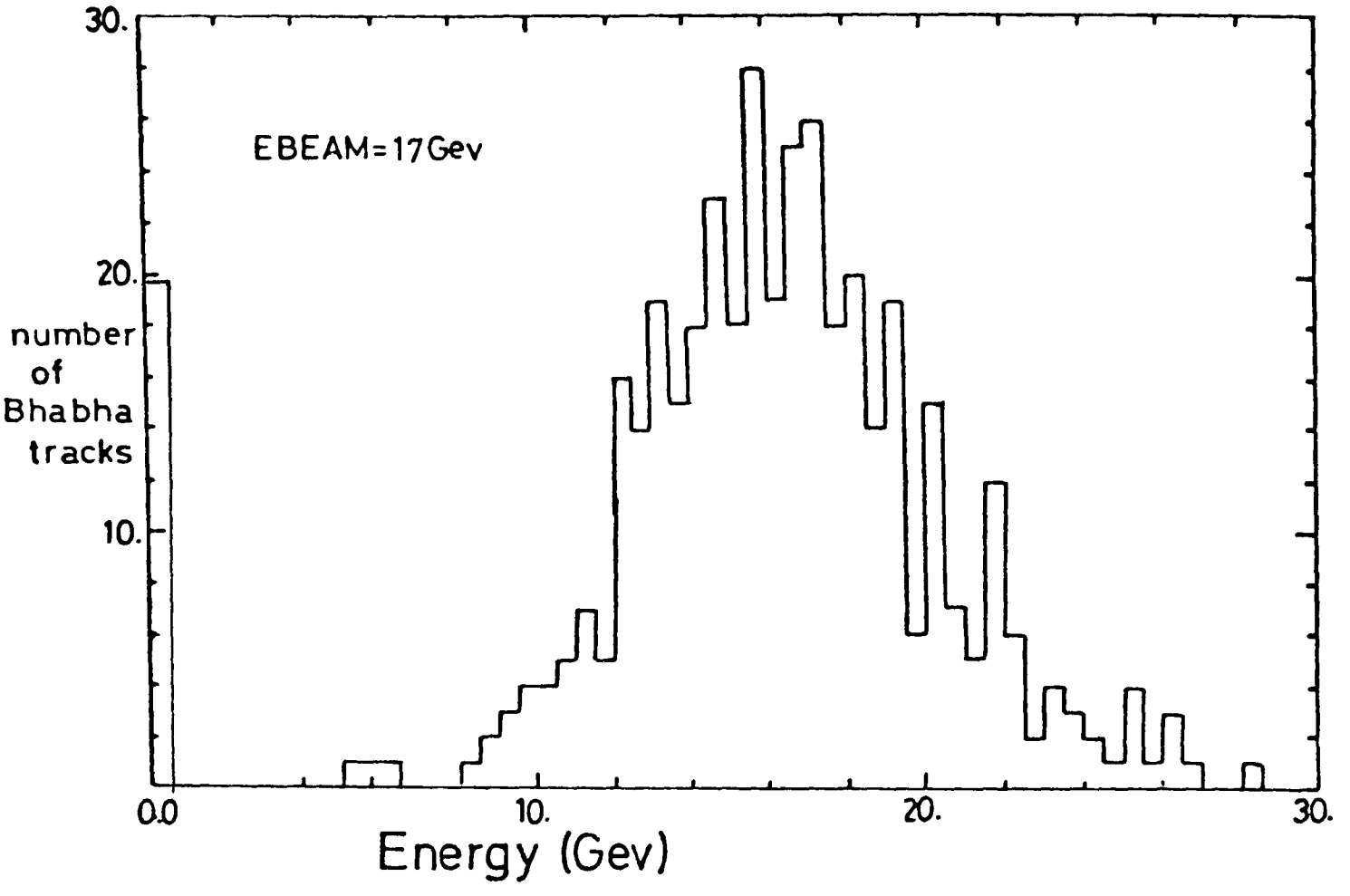

Figure 3.9 Shower energy deposited in HASC by Bhabha electrons.

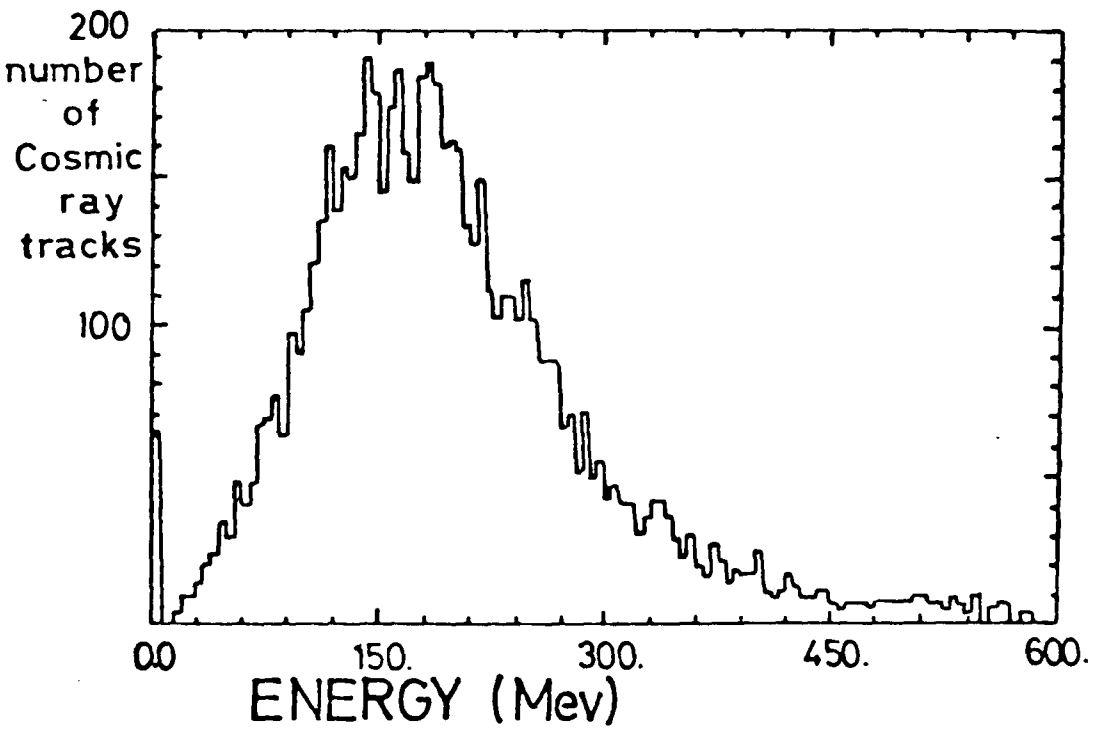

Figure 3.10 Shower energy deposited in HASC by cosmic ray muons during normal data taking runs.

CHAPTER 4

Data acquisition and data reduction

4.1 Introduction

This chapter describes how information from the many components of the experiment was combined to selectively trigger on events of physics interest and how these recorded events were reconstructed and sorted into event classes.

4.2 The Trigger

Triggering was a difficult task as background rates were high and the time between successive beam crossings was short. These considerations argued for a tight, fast trigger condition but a wide range of interesting final states existed and therefore the trigger conditions had to be sufficiently loose to include them all. The compromise used was to have several trigger levels and collect data using an 'OR' of several trigger conditions each tailored towards a particular event class.

The passage of beams through the TASSO apparatus was capacitively sensed by probes mounted around the beam pipe at a distance of 7.1 metres from the interaction point. The sign change of the induced signal from the passing positron bunch was accurately determined using a very fast zero cross discriminator. This signal was used both as a timing reference and a strobe signal to initiate triggering of the experiment. The time

between successive beam crossings was expected to be 1.9 μs if PETRA operated with 4 positron and 4 electron bunches. Thus the controller for the fast trigger logic electronics, the SIGH (Signal Interrupt and Gate Handler) box, was designed to accept and process signals arriving < 0.9 μs after the beam crossing, allowing 1 μs to reset NIM fast electonics if the crossing proved to be of no interest. During the first 0.9 μs two levels of trigger were distinguished:

1/ Stand Alone Triggers. These immediately indicated an acceptable event and so the SIGH box initiated the reading of data into the online NORD 10 computer and inhibited the issuing of further strobe signals.

2/ Pretriggers. If there were no stand alone triggers but there was a pretrigger, the SIGH box inhibited the sending of further strobes. However the event was not read into the online NORD computer unless further trigger signals, called posttriggers were recieved within 5.5 μs of the initial strobing.

If a valid posttrigger was recieved the data from the apparatus was read into the NORD 10 computer as in the case of stand alone triggers. If no posttrigger occurred the experiment was reset, ready to recieve the strobe from the next beam crossing.

Several of the main experimental triggers relied on information from the hardware processors which analysed hits from the central tracking chambers.

4.2.1 CPC processor[50]

The CPC processor correlated hits in adjacent layers of the CPC which had similar ϕ coordinates. The CPC was divided into 48 equal size $d\phi$ segments. Signal bits corresponding to each of these 48 segments

constituted the output from the processor, the output patterns being referred to as the CPC '48 bits'. A CPC 48 bit was set if correlated hits were found in 3 or 4 layers of the corresponding dϕ sector. The range in ϕ over which the processor searched for hits and hence the minimum transverse momentum, p_t, required of a track, could be programmed. For most data periods it was set to correspond to about a 100 Mev track.

4.2.2 Drift Chamber processor

The Drift Chamber Preprocessor (DC Prepro) utilised the hits from six of the nine '0' degree wires of the Drift Chamber together with the CPC 48 bits and ITOF mean timer bits. It searched for track segments using the Drift Chambers hits by comparing them with 15 track momentum masks using fast programmeable logic arrays. A good track was found if a track segment had corresponding (to ± 1 bit) CPC 48 bit and ITOF mean timer bits set. The number of tracks found was determined by the multiplicity of ITOF mean timer bits. For example, if 2 ITOF bits were correlated with 1 track segment it was counted as 2 seperate DC Prepro tracks. Conversely if 2 track segments extrapolated to the same ITOF counter only 1 DC Prepro track was counted.

The set of triggers satisfied by an event was coded for offline analysis into a 16 bit trigger word. Table 4.1 shows a list of triggers used during the 1980 data taking. The triggers of relevance to the work of this thesis will now be described in detail.

4.2.3 The Pretrigger (trigger bit 1)

This was formed by demanding a logical AND of a least one of each of the following ; a Beam Pipe Counter mean timer bit, a CPC 48 bit and a ITOF mean timer bit. During the 1980 data period the Beam Pipe Counter component was not required.

Bit	Trigger	Trigger Word (Octal)
1.	Pretrigger	1
2.	Liquid Argon Barrel	2
3.	Free	
4.	Free	
5.	Free	
6.	Luminosity	40
7.	ITOF Cosmics	100
8.	Lead-Scintillator Neutral	200
9.	Double Tag	400
10.	Free	
11.	DC prepro; Majority and Topology	2000
12.	Liquid Argon End-Cap	4000
13.	Free	
14.	(Lead-Scintillator)·(1 track)	20000
15.	(Single Tag)·(1 track)	40000

Table 4.1 Triggers used by TASSO at the end of 1980.

4.2.4 The DC Prepro Trigger (trigger bit 11)

This trigger could be set by one of two conditions :

1/ Majority Logic - This required at least 4 DC Prepro tracks each with greater than 320 Mev transverse momentum. High multiplicity hadronic events from the single photon annihilation process were captured by this trigger.

2/ Topology trigger - This demanded 2 or 3 Prepro tracks with 2 of the relevent ITOF mean timer bits opposite to within ± 3 ITOF counters. This meant that events with high momentum tracks had to be collinear to better than 22.5^{0}. The majority of Bhabha events were collected on this trigger.

4.2.5 Shower Counter Triggers (trigger bits 8 and 14)

These triggers have been described in detail in Chapter 3. They were useful in collecting an independent sample of Bhabha events to be compared with samples selected using topological track information and were used to calculate 2 track efficiency factors.

4.2.6 Forward Detector Triggers (trigger bits 9 and 15)

This trigger was formed by an AND of $\geq$ 4 Gev energy in the lead glass blocks of the Forward Detector and at least 1 DC Prepro track. It was used to collect low multiplicity 2γ events, the large shower energy deposit being due to one of the scattered initial state electrons. These triggers were used in efficiency determinations.

4.3 Event Readout

The online computer used by the experiment was a NORD 10. It was interfaced to detectors using standard CAMAC highways[51]. Typically the data from each event consisted of 2000 16 bit words which were read into the NORD in 40 ms. Events entered a short buffer in NORD memory where they were reformatted to be compatible with the offline data handling structures, BOS (Bank Organisation System)[52]. These events were immediately available to monitoring tasks and routine diagnostic histograms of wire hits or TDC or ADC distributions were accumulated from them.

After this buffer the events were transferred to a NORD disk. This could hold 10000 events which corresponded to 3 hours of data taking for an event rate of 1 Hz. Following this large buffer the events were transferred over a microproccessor link to the DESY central computing complex. Eventually the events were written to 6250 BPI tapes, each of which could hold about 15000 events.

4.4 Track Reconstruction algorithms

Most stages of the offline reduction relied heavily on information from charged tracks reconstructed from hits in the tracking chambers of the Central Detector. Two track finding algorithms were used at different stages of the offline reduction.

4.4.1 FOREST[53]

This was a very fast program used at an early stage to reconstruct tracks in the r-ϕ plane. It used only the hits of the Drift Chamber and assumed a linear drift time relation over the full drift cell volume. Tracks were fitted to circular arcs. The program was based on an algorithm whereby links connecting hits with similar ϕ in adjacent Drift Chamber layers were themselves interconnected, if they had a similar $\frac{d\phi}{dr}$, to form a tree like structure. The tree pattern for a possible genuine

track was readily discerned using simple criteria.

The FOREST program included an algorithm called ZREC to fit tracks in the y-z plane using the information of the α wire hits from the Drift Chamber. However this was only invoked if FOREST found 2 or more tracks in the r-ϕ projection. The FOREST/ZREC program typically took 50 ms of IBM 370/168 central proccessor time to reconstruct a 12 prong event.

4.4.2 MILL[53]

MILL was a much slower program than FOREST and was only used on smaller samples of preselected events. It performed a much more rigorous track search, trying many more hit permutations and including the hits from the CPC. The projected position of the track in the drift cell and the entrance angle to the cell were determined and a non-linear drift time relation over the cell volume was used. For the same event as quoted above the MILL program required 8 seconds of IBM 370/168 processor time.

Chapter 5 describes a method which was used to determine the efficiency of these track finding algorithms for low multiplicity events. Generally for tracks with momenta greater than 0.2 Gev FOREST was more than 90% efficient while MILL was determined to be 100% efficient. The efficiency of FOREST varied with time due to poor determinations of the drift time relation of charged particles.

Figure 4.1 shows the central tracking chamber for a hadronic annihilation event before and after track reconstruction.

4.5 Track parameterisation

The final track parameterisation was via the 6 variables shown in Figure 4.2. R denotes the radius of the track projection in r-ϕ, d_0 is the distance of closest approach to the origin in r-ϕ (+ve if the origin is within the track circle), z_0 is the closest distance to the origin in the z coordinate and θ is the angle of dip of the track. The track charge, determined from the sign of the radius of curvature, was denoted

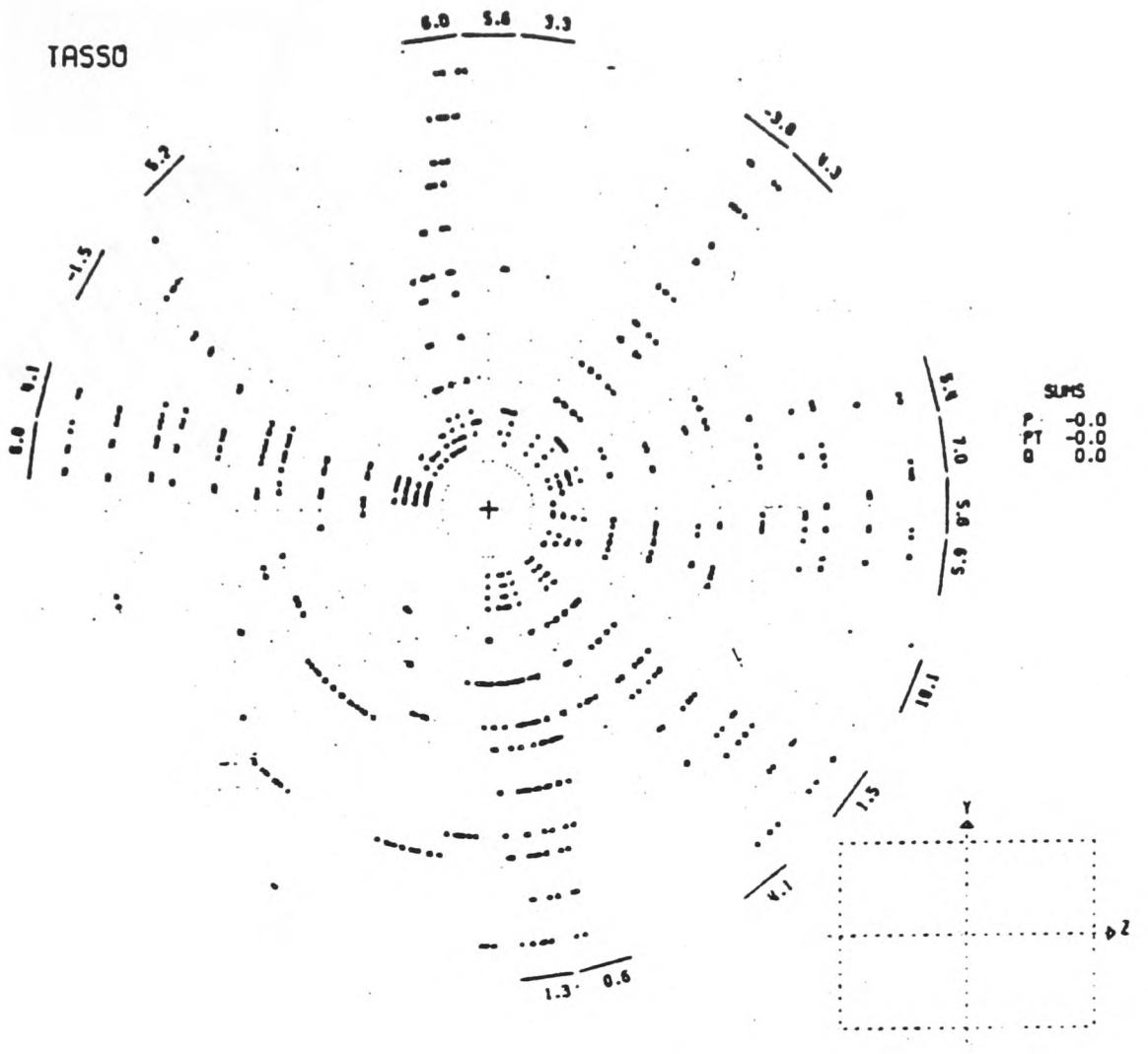

Figure 4.1 TASSO hadronic event before and after track reconstruction.

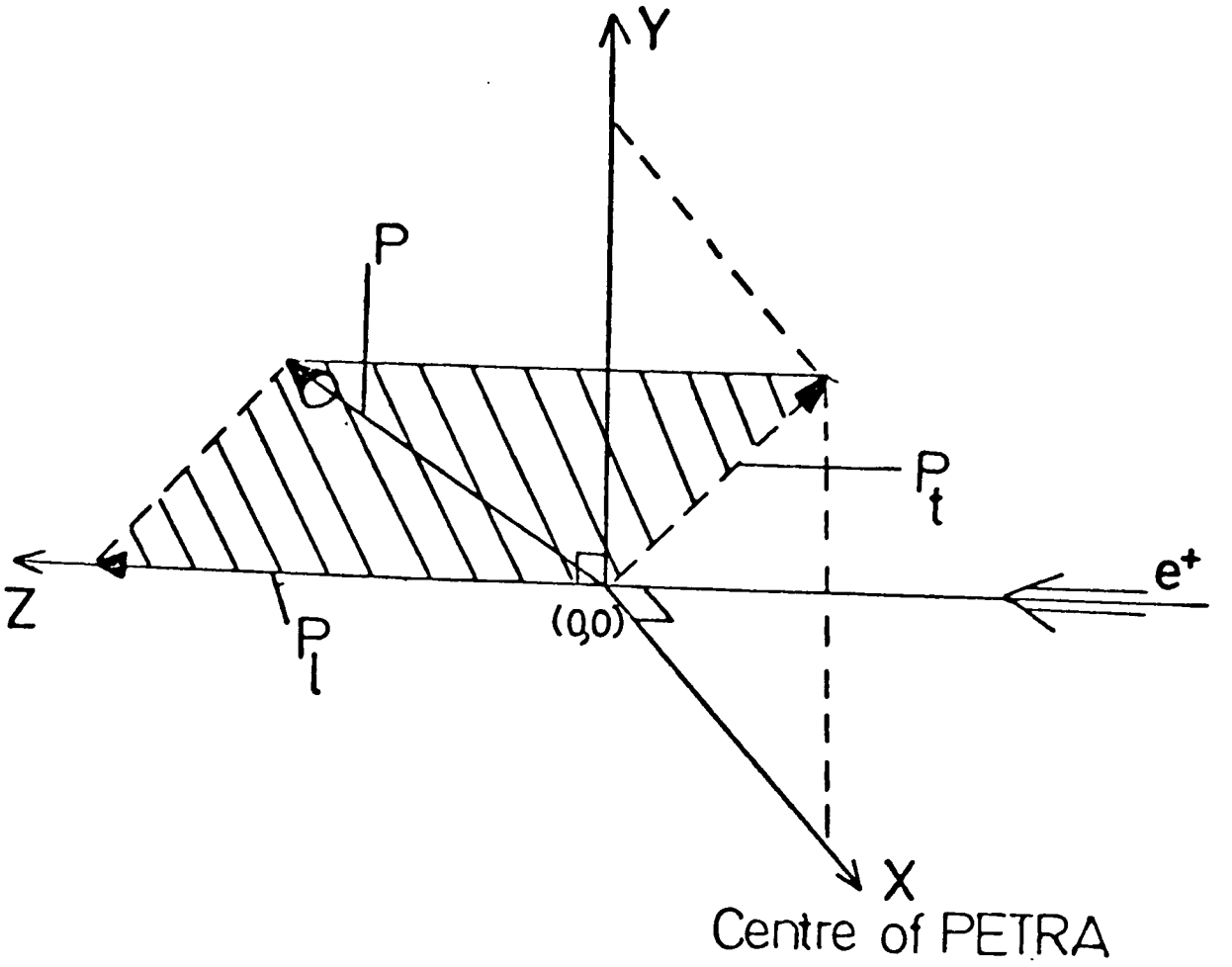

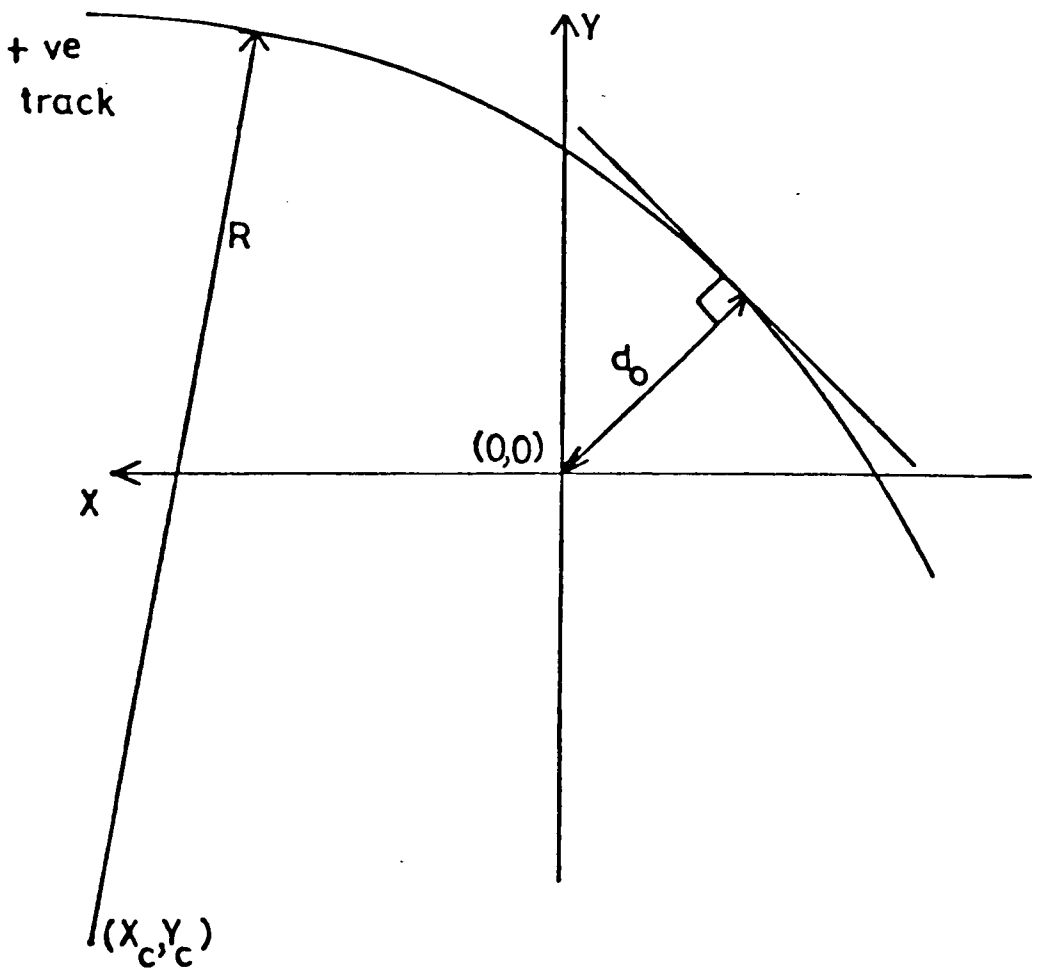

Figure 4.2 Definition of main track parameters.

by Q. The track momentum is denoted by p. The transverse momentum, p_t, is the momentum projection in the r-ϕ plane. The track quality was gauged by calculating a χ^2 for the fitted track. The resolution in r-ϕ was 200 microns. The d_0 resolution was 2-3 mm which is consistent with multiple scattering errors in the material of the inner detector. The resolution in z was about 5 cm and was limited by the bunch length.

4.6 Standard Data Reduction procedures

The vast majority of triggers accepted by the online experiment originated from background processes such as beam gas or beam pipe interactions or cosmic ray events. The principal steps leading to the extraction of physics events is illustrated in Figure 4.3, indicating the number of events remaining at each level of reduction. The cuts made at each step are described in further detail below.

4.6.1 Pass 1

This stage involved no rejection of events. The FOREST trackfinder was run on all events and some reformatting of events was carried out. Calibration data for ADC's and TDC's was included at this point.

4.6.2 Forward Detector Triggers

A file of triggers from the Forward Detector was produced from Pass 1 tapes by demanding

1/ single tag + 1 track trigger (bit 15)

2/ $\geq$ 3.5 Gev measured shower energy in the Forward Detector

3/ $\geq$ 2 tracks in r-ϕ with $|d_0| < 2.5$ cms

4/ $\geq$ 1 track in r-ϕ-Z with $|z_0| <$ 30cms

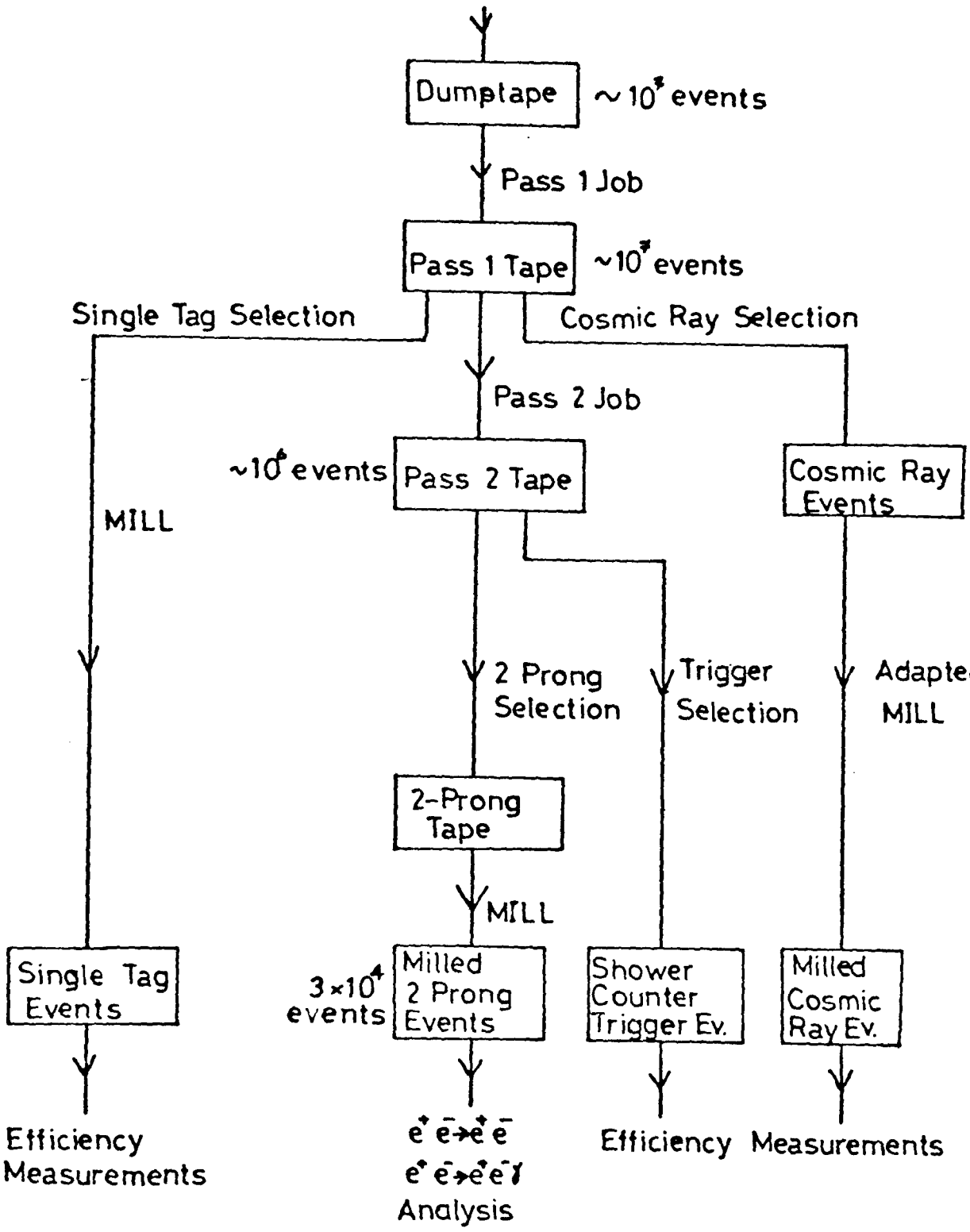

Figure 4.3 Data reduction steps.

4.6.3 Pass 2

Events from Pass 1 tapes were outputted to Pass 2 tapes if they satisfied at least 1 of the following 3 criteria

a/ $\geq$ 2 tracks found in the r-ϕ projection with each track having $|d_0| < 2.5$ cms.

b/ a Forward Detector trigger bit set (bits 9 or 15)

c/ a neutral energy trigger bit set (bit 8 or 14)

4.6.4 Shower Counter Trigger Selection

Pass 2 data with shower counter bit 15 (Shower + > 1 track) was written to a seperate file for approximately one quarter of the data. This provided a sample for the determination of charged 2 prong efficiencies.

4.6.5 Two Prong Data Sample

This selection utilised ITOF and track information. The ITOF information was essential to remove cosmic ray events. Typically a cosmic ray took 10 ns to traverse the diameter of the Drift Chamber. Two collinear tracks from a genuine beam event had a difference of ITOF times centred around 0 ns.

The cuts used to select events from Pass 2 were

1.) 2 to 4 tracks found in r-ϕ, having $|d_0| < 2.5$ cms and transverse momenta of greater than 100 Mev. If greater than 2 tracks the others had to form a cone in r-ϕ with $d\phi < 5.0^0$.

2.) $\geq$ 1 track reconstructed in r-ϕ-z with $|z_0| < 15$ cms.

3.) At least 2 tracks collinear in r-ϕ to within 15^0.

4.) ITOF information had to be available for the fastest tracks in each hemisphere and the absolute value of the time difference for these 2 tracks had to be less than 5 ns (removes cosmic ray events.)

After this selection using FOREST track information the events of this file were processed by the MILL track finding program. This file countained events from Bhabha scattering, muon pair production and 2 photon processes. Chapter 5 describes how harsher cuts were used to measure the Bhabha cross section.

CHAPTER 5

Determination of the Bhabha cross section

5.1 Introduction

This Chapter presents a determination of the cross section for the reaction $e^+ e^- \rightarrow e^+ e^-$ at several beam energies between 6 Gev and 18 Gev using data collected by the TASSO experiment at the PETRA storage ring between September 1979 and December 1980. A large sample of Bhabha events is identified, using tracking information from the Central Detector, by their distinct topological signature. The cross section results are compared to QED and used to to place limits on the popular electroweak scenarios.

5.2 Data Samples

Table 5.1 indicates the relative amounts of data collected as a function of time and of beam energy. Several time periods indicated by SCAN were times when the PETRA beam energy was incremented in 10 Mev steps, collecting 30 nb^{-1} at each energy setting. This was an attempt to discover narrow bound toponium states. For the analysis of this Chapter cross sections are calculated on a run by run basis using the appropriate beam energy.

Run Numbers	Date	Energy (Gev)	Luminosity (nb^{-1})	Type
658 - 724	Jul 79	15.8	67.8	
725 - 763	Jul 79	13.9	94.5	
765 - 1385	Aug - Nov 79	15.0	2314.8	Scan
1421 - 1571	Nov 79	6.0	97.0	
1678 - 1729	Feb 80	16.5	87.0	
1730 - 1760	Feb 80	17.0	5.5	
1761 - 1891	Mar 80	17.5	253.3	
1892 - 1962	Mar 80	17.9	96.1	
1964 - 2200	Mar - Apr 80	17.5	831.1	Scan
2201 - 2232	May 80	15.0	128.9	
2233 - 2260	May 80	18.3	102.7	
2263 - 2348	May - Jun 80	17.8	256.9	Scan
2350 - 2481	Jun 80	18.3	296.0	
2482 - 2833	Jul - Aug 80	17.0	2162.7	Scan
2834 - 3041	Aug 80	16.5	1237.0	Scan
3077 - 3247	Oct - Nov 80	18.0	610.0	Scan

Table 5.1 Run numbers, beam energies and luminosities of data.

The analysis was performed using the 2 prong datasets whose selection from online triggers is described in detail in Chapter 4. These datasets contain a mixture of Bhabha events, muon pair events, cosmic ray events and events induced by the 2γ process.

5.3 Event Selection

5.3.1 Experimental Signature

The single photon exchange diagrams responsible for Bhabha scattering are shown in Figure 1.1. These diagrams produce events containing 2 collinear electrons each with an energy equal to that of the initial beam particles. Thus, events should be easily identified using simple cuts on the final state energies and acollinearity of the 2 charged final state tracks. Several factors make the identification of events from the zeroth order process more difficult :

Detector interactions

While traversing the detector electrons or positrons may interact to produce electromagnetic showers. This will change the multiplicity of the detected event and will degrade both the energy and angular distributions of the events.

Detector resolution

All measured track quantities have errors associated with them due to the finite resolution of the measuring methods and apparatus. At high energies these resolutions can be quite large i.e. the momentum measurement error on a 15 Gev charged particle in the Drift Chamber is as large as 4.5 Gev.

These considerations mean that energy and acollinearity selection criteria have to be less stringent than first imagined.

Radiative corrections

Higher order QED diagrams can produce events with identical or similar topologies to those of the zeroth order diagram. The contribution of these events to the data sample selected depends on the experimental cuts used and the resolution of the apparatus. It is calculable using analytic QED formulae in conjunction with a Monte Carlo model of the apparatus.

Background processes

Several other processes have characteristics in common with the Bhabha process and can therefore be miscatagorised as Bhabha events. These include muon pairs, cosmic rays and low multiplicity 2γ events. Their contribution to a sample of Bhabha events depends on the cuts used in the event selection. Section 7 of this Chapter discusses in detail the background contamination of the final event sample.

5.3.2 Experimental Cuts

The following cuts were used to isolate a large, clean sample of candidate Bhabha events :

1.) 2 track coplanar trigger (bit 9) set

2.) 2 and only 2 charged tracks reconstructed in 3 dimensions, r-θ-ϕ

3.) each charged track to have

(a) $|\cos(\theta)| < 0.8$

(b) $p_i > 0.2 \times E_b$ where p_i is the charged particle momenta and E_b is the beam energy.

(c) $|d_0| < 1.5$ cms

(d) $-3.0 > t_m - t_c > 2.0$ ns

where t_m is the ITOF measurement for the track and t_c is the expected ITOF measurement calculated using the Drift Chamber momentum of the track, assumming pion masses.

4.) Each event to satisy :

(a) $\Sigma_i\ p_i > 0.7 \times E_b$ for i=1,2

(b) $\delta < 10^0$ in 3 dimensions where δ is the acollinearity angle between the 2 charged tracks

(c) $\langle z_0 \rangle < 6.0$ cm where $\langle z_0 \rangle$ is the mean z_0 of the 2 charged tracks in the event.

(d) $|t_1 - t_2| < 5.0$ ns where t_1 and t_2 are the measured ITOF times of flight of the 2 charged tracks.

Cuts 1 and 2 were applied for definiteness to avoid bias in the determination of correction factors to the data. They also rejected some high multiplicity background events i.e. taus.

Cut 3(a) on the $|\cos(\theta)|$ of tracks was applied because of trigger efficiency correction considerations. The trigger requirement, which includes an ITOF mean timer bit, limits, because of the length of the counters in z, the acceptance of the trigger in θ to $|\cos(\theta)| < 0.828$. However to avoid edge effects, which would have introduced large uncertainties in the the determination of large correction factors, the $|\cos(\theta)|$ range was cut to $|\cos(\theta)| < 0.8$.

The cuts on $|d_0|$ and $\langle z_0 \rangle$ require the tracks to have come from a consistent interaction region.

The cut 3(d) requires the counters to have reliable ITOF information. The cut 4(d) on the time of flight difference of tracks is the same as that imposed in the selection of the 2 prong tapes from FOREST tracks. This cut is imposed after the tracks have been put through the MILL track finding program. It excludes the majority of the cosmic ray background.

The momentum cuts were chosen to exclude most of the 2γ background whilst retaining the majority of the genuine Bhabha events. Figure 5.1 shows the distribution of the sum of charged energy seen in hadron events produced by both the 1γ and 2γ processes and illustrates the positioning of this energy cut.

5.4 Calculation of the Bhabha cross section

For the i^{th} data taking run at a centre of mass energy $\sqrt{s_i} = 2\times E_b$ and of integrated luminosity L_i, the differential cross section is given by

$$s_i \frac{d\sigma_i}{d\cos(\theta)} = \frac{s_i\, N_i(s,\theta)}{L_i\, \epsilon_i(s,\theta)\, \Delta\cos(\theta)} \qquad (5.1)$$

where N_i is the number of events observed in the angular interval $\Delta\cos(\theta)$ and $\epsilon_i(s,\theta)$ is the efficiency for observing events at this beam energy in that same angular interval. ϵ can be written as the product of several efficiency factors:

$$\epsilon = \epsilon_{trigger} \times \epsilon_{recon} \times \epsilon_{cuts} \times \epsilon_{rad} \qquad (5.2)$$

The component terms are for losses due to trigger, reconstruction, detector interactions, selection cuts and the effect of radiative corrections. These corrections are generally functions of both particle energies and angle. The calculation of these efficiencies is described in later sections.

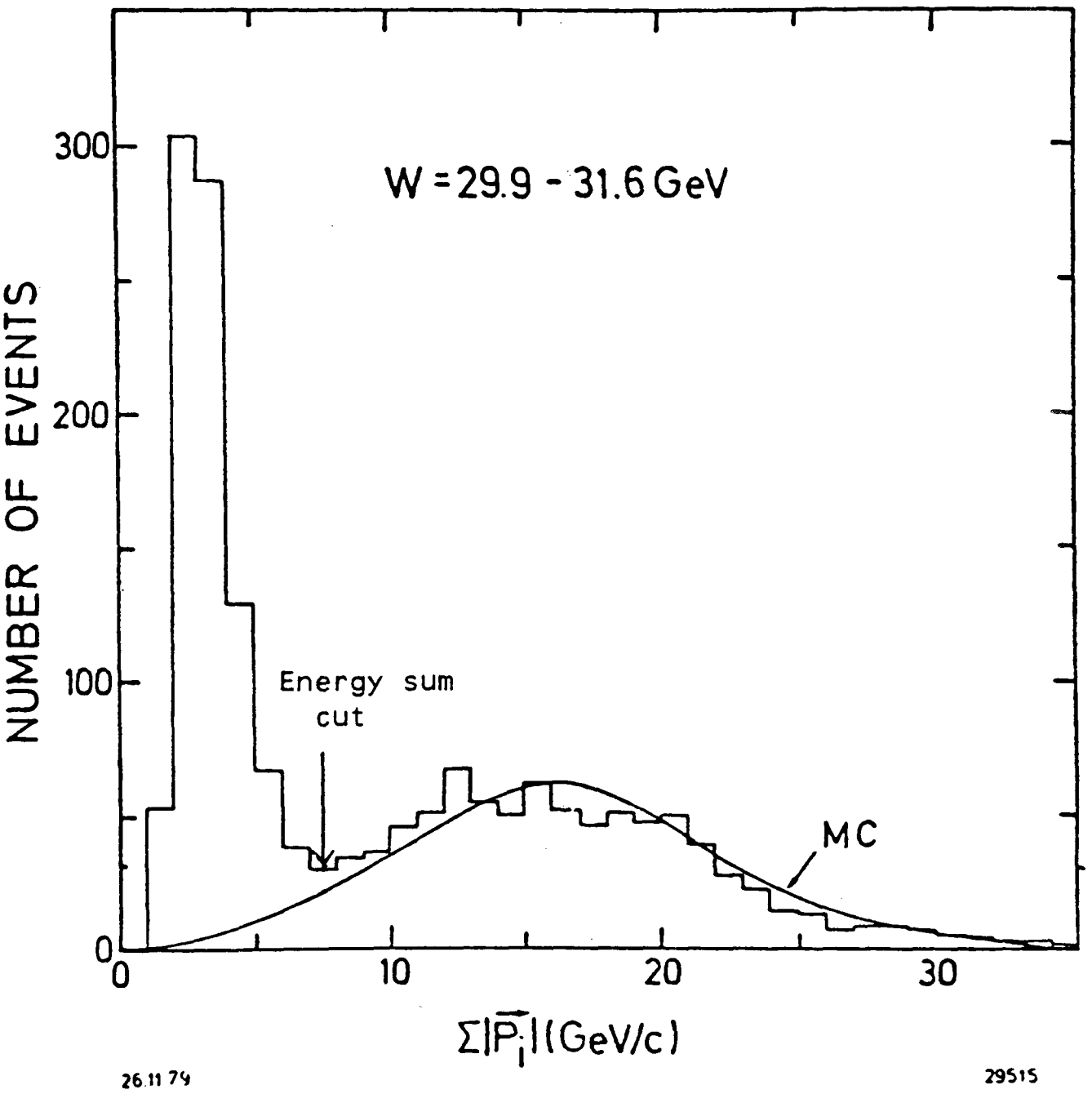

Figure 5.1 Charged particle momenta for hadron events. This illustrates the seperation of events for 1 and 2 photon annihilation events using the sum of seen charged energy.

For the following discussion we consider a single angular interval. The terms $f_i = \frac{s_i}{L_i \, \varepsilon_i}$ vary from run to run and when combining the cross section measurements from several runs they should be used as relative weights for each run. If we consider statistical errors only we can write

$$\sigma_i = f_i \times N_i \quad \text{and} \quad \mathrm{Var}(\sigma_i) = f_i^{\,2} \times N_i \tag{5.3}$$

where σ_i is the cross section estimate of the i^{th} run, which contains N_i events. We wish to derive a weighted mean of many runs to get a best estimate of the cross section, σ. If we knew the weighted mean σ and the f_i, we could calculate the predicted number of events Np_i which are expected in the i^{th} run.

$$Np_i = \frac{\sigma}{f_i} \tag{5.4}$$

Conversely if we had measured this number of events in the i^{th} data run we would calculate the cross section σ for this run as

$$\sigma = f_i \, Np_i \tag{5.5}$$

By using Np_i as weighting factors, we minimise biases introduced into the cross section determination by downward statistical fluctuations in short data taking runs.

The weighted mean is

$$\sigma = \frac{\Sigma_i \, \sigma_i \, Np_i}{\Sigma_i \, Np_i} = \frac{\Sigma_i \, N_i \, \sigma}{\Sigma_i \, \frac{\sigma}{f_i}} \tag{5.8}$$

$$\sigma = \frac{\Sigma_i \, N_i}{\Sigma_i \, \frac{1}{f_i}} \tag{5.9}$$

and the error on this mean value is given by

$$Var(\sigma) = \frac{\Sigma_i N_i}{(\Sigma_i \frac{1}{f_i})^2} \qquad (5.10)$$

This formalism was used to calculate the differential cross section. The number of events selected after background subtraction was used for calculation of the mean. The number of events before background subtraction was used for calculation of the associated errors. A total cross section was calculated by summing the contribution of each angular bin over the angular range of study, $|\cos(\Theta)| < 0.8$.

5.5 Determination of Efficiencies

To convert the number of events selected by the cuts of Section 5.3.2 to a cross section requires a knowledge of the efficiency of the TASSO apparatus and the data reduction and selection procedures. For low multiplicity collinear trigger events these factors were investigated using both data samples of independent triggers and by the use of detailed Monte Carlo models of the physics processes and the effect of the apparatus.

Samples of events collected using the independent triggers afforded by the HASC (Hadron Arm Shower Counters) and the Forward Detector were isolated. These data samples were used to measure the efficiency of the collinear trigger, the track reconstruction programs and some of the event selection cuts. Using data samples from the same runs and averaging over short periods allowed the efficiency to be continuosly monitored. The results of these determinations were used as input to the Monte Carlo simulations of the apparatus.

5.5.1 Trigger Efficiency

The collinear 2 prong trigger is described in detail in Chapter 4. It required a correlation of a CPC 48 bit, a ITOF mean timer bit and a Drift Chamber preprocessor bit. For data collected in 1979 an additional requirement of any 1 of the 4 Beam Pipe mean timer bits was required. The efficiency of each of these components was determined for several data periods, using data from HASC and Forward Detector triggers, by selecting a clean sample of 2 prong events using shower and track information. The following cuts were applied :

1) shower + 1 track (bit 14) or forward tag (bit 15) trigger bit set

2) 2 and only 2 tracks reconstructed in 3 dimensions

3) each track to have $p_i > 300$ Mev , $|d_0| < 1.0$ cm , $|z_0| < 4.0$ cm

These cuts gave a clean sample of low multiplicity events from both the Bhabha and the 2γ reactions.

5.5.1.1 CPC 48 Bit and ITOF Mean Timer Bit Efficiences

The CPC 48 bit and ITOF mean timer bit efficiencies were determined by projecting tracks onto the CPC and ITOF sectors and then counting the relative number of times the appropriate sector bit was set. It was required that there were no additional tracks projected into any of the adjacent sectors. The efficiency per track, ε, of these trigger components is determined by

$$\frac{\text{number of tracks with bit set}}{2 \times \text{number of events}} = \frac{1}{2 - \varepsilon} \qquad (5.11)$$

This formula corrects for the bias introduced into the determination by using an event sample which required 1 track to have been found at the trigger level. The error on the efficiency determination was estimated using the Binomial distribution.

5.5.1.2 Drift Chamber Prepro Efficiency

For the determination of the DC Prepro efficiency events were selected which had 2 CPC 48 bits and 2 ITOF mean timer bits set, with the counters collinear to within ± 3 ITOF bits. If the DC Prepro was perfectly efficient these events would fire the 2 prong collinear trigger every time. By counting the number of events with a set 2 prong trigger bit the efficiency of the DC Prepro per track, ε, could be determined via the expression

$$\frac{\text{number of events with set trigger bit}}{\text{number of events in sample}} = \frac{\varepsilon}{2-\varepsilon} \qquad (5.12)$$

This formula corrects for the bias introduced by using events which, by selection, have at least one good track at the trigger level. Errors were assigned using the Binomial distribution.

5.5.1.3 Beam pipe Counter Efficiency

The beam pipe counter efficiency was determined by counting the multiplicity of counters set in each event. As the counters were close to the beam, the setting of a mean timer bit could occur either by the passage of a good track through the counter (P_1) or by a random track generated by stray interactions in the beam pipe(P_2). A fit to the observed multiplicity of set bits was made using the probabilities P_1 and P_2 as free parameters. The result was

$$P_1 = 0.784 \pm 0.023$$

$$P_2 = 0.139 \pm 0.0015$$

This means that the probabilty of an event having at least 1 beam pipe counter bit set is 0.97 ± 0.02.

Table 5.2 shows the results of the trigger efficiency determinations. The main inefficiency is from a gradually worsening ITOF mean timer efficiency factor. In all these determinations no significant dependence of the efficiency on $x = (p_i/E_b)$ or $|\cos(\theta)|$ was found. Figure 5.2 shows the angular and energy dependences for the ITOF mean timer bit efficiencies.

5.5.2 Reconstruction Efficiency

To determine the efficiency of the track reconstruction programs, FOREST and MILL, a data sample of clean low multiplicity events was selected using information from the trigger bits, the ITOF mean timer and CPC mean timer bits. The cuts used were

1) shower + 1 track trigger (bit 14) or Forward Detector + 1 track trigger (bit 15)

2) 2 and only 2 ITOF mean timer bits opposite each other to within 1 mean timer sector

3) 2 and only 2 CPC 48 bits set. The bits had to be collinear to within ±1 48 bit and had to be collinear with the set ITOF mean timer bits to within 1 sector.

The efficiency of all the programs was determined by taking the ratio of the number of tracks reconstructed to the number of tracks expected in the event. The number expected was always 2. Before determining the ZREC efficiency the event sample was required to have at least 2 tracks found in r-ϕ by the FOREST algorithm. Similarly the MILL efficiencies were

Run Period	CPC 48 Bit (per trk)	ITOF MT (per trk)	Beam Pipe MT (per event)	DC Prepro (per trk)	Total Trigger Efficiency per 2-prong event
638 - 1385	0.990 ±0.004	0.983 ±0.004	0.970 ±0.001	0.997 ±0.010	0.913 ±0.023
1421 - 1571	0.990 ±0.004	0.983 ±0.004	0.970 ±0.001	0.997 ±0.010	0.913 ±0.023
1680 - 2200	0.994 ±0.003	0.974 ±0.006	-	0.992 ±0.010	0.913 ±0.024
2201 - 2325	0.987 ±0.003	0.961 ±0.006	-	0.995 ±0.005	0.891 ±0.017
2352 - 2829	0.987 ±0.003	0.961 ±0.006	-	0.995 ±0.005	0.891 ±0.017
2834 - 3041	0.988 ±0.003	0.945 ±0.007	-	0.990 ±0.005	0.854 ±0.019
3077 - 3489	0.988 ±0.003	0.945 ±0.007	-	0.990 ±0.005	0.854 ±0.019

TABLE 5.2 Trigger Efficiencies

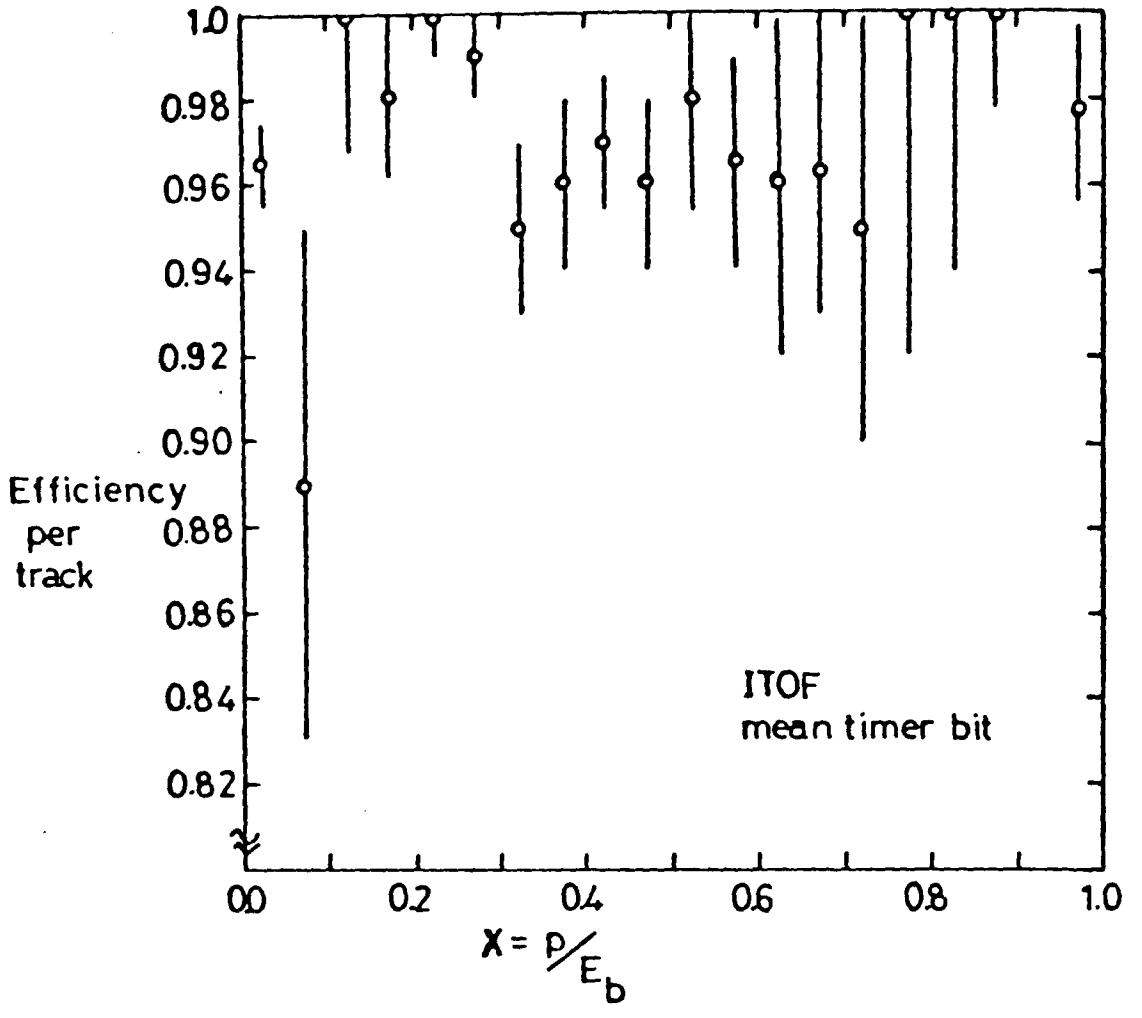

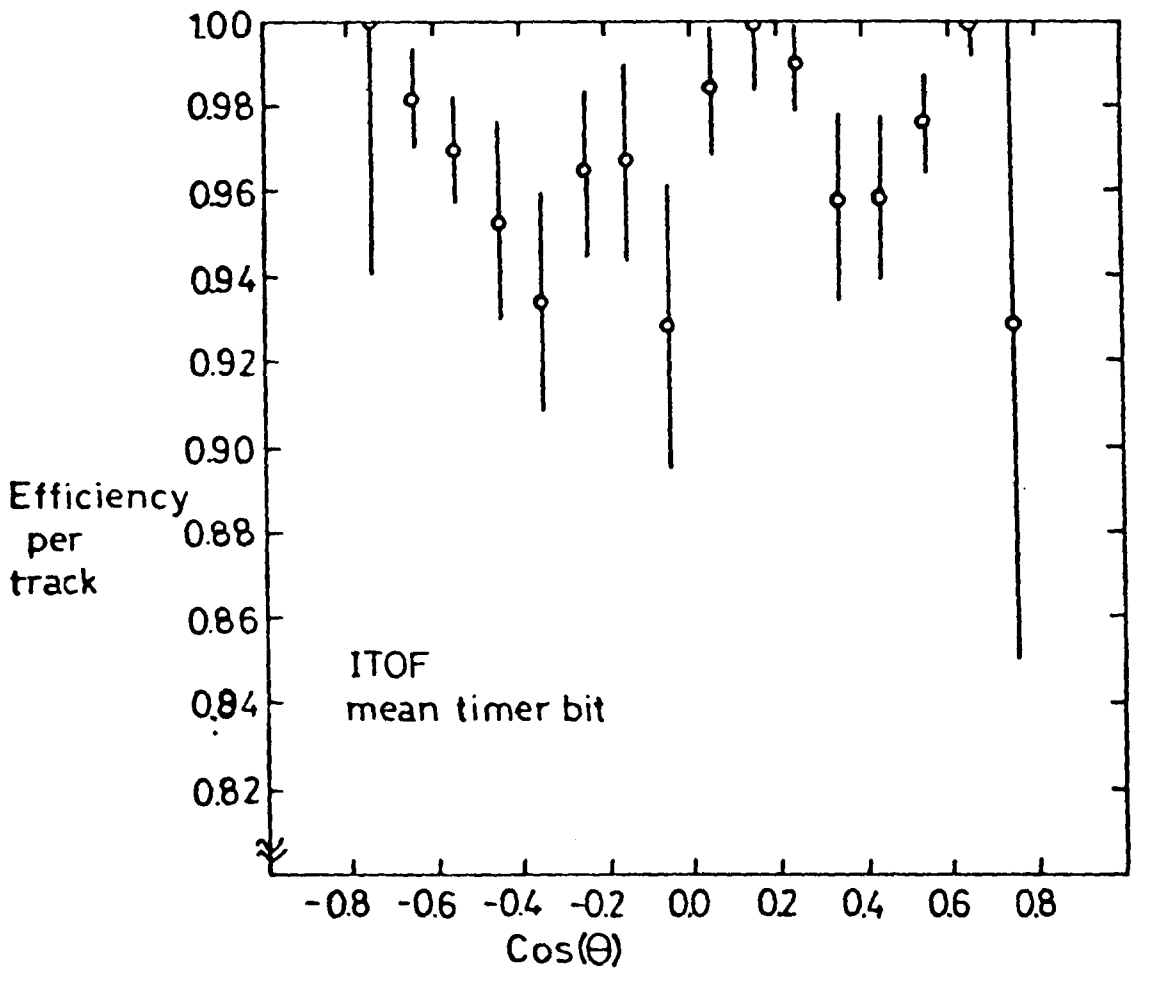

Figure 5.2 Angular and energy dependence of trigger efficiency component.

determined on the sample of events which passed the data reduction cuts imposed on the sample which had undergone FOREST and ZREC reconstruction.

The results of the reconstruction efficiency determinations are given in Table 5.3. The FOREST efficiency suffers a dramatic deterioration after run number 2352. This is associated with a change in the gas mixture of the Drift Chamber from an Argon/Methane mix to an Argon/Ethane mix. This necessitated the resetting of high voltages on all the cells of the chamber and a redetermination of the drift time relation for all the cells. Towards the end of the data period these effects became better understood and the efficiency once more rose to values achieved before this change. The MILL program efficiency always remained at 100%.

No significant angular or energy dependence was discerned for tracks with $|\cos(\theta)| < 0.8$ and $p > 200$ Mev.

5.5.3 Selection Efficiency

The efficiencies of the $|d_0|$, $\langle z_0 \rangle$ and ITOF cuts were measured by selecting a clean sample of Bhabha events using the same cuts as described in the reconstruction efficiency section above, but with the extra requirement of a deposit of energy in the shower counters behind the appropriate mean timers. This selection utilises only shower energy information, CPC 48 bit and ITOF mean timer bit information and provides a sample with little bias as far as track or timing information is concerned.

The results of the selection efficiency determinations are shown in Table 5.4. The statistics of the measurement are limited for certain data periods due to the lack of shower detector coverage. However the values for the efficiencies are consisent within the statistial errors. The $|t_1-t_2|$ cut efficiency was found to be the same for both FOREST and MILL tracks.

Run Period	Forest r-ϕ (per trk)	Forest zrec (per trk)	Mill r-ϕ (per trk)	Mill z (per trk)	Total Recons Efficiency per 2-prong event
638 - 1385	0.980 ±0.010	0.957 ±0.006	1.000 ±0.001	1.000 ±0.001	0.955 ±0.020
1421 - 1571	0.964 ±0.012	0.980 ±0.006	1.000 ±0.003	1.000 ±0.003	0.929 ±0.025
1680 - 2200	0.979 ±0.008	0.964 ±0.007	1.000 ±0.002	1.000 ±0.002	0.957 ±0.024
2201 - 2325	0.979 ±0.008	0.964 ±0.007	1.000 ±0.002	1.000 ±0.002	0.957 ±0.017
2352 - 2829	0.892 ±0.014	0.912 ±0.009	1.000 ±0.001	1.000 ±0.001	0.786 ±0.017
2834 - 3041	0.905 ±0.020	0.920 ±0.013	1.000 ±0.003	1.000 ±0.003	0.814 ±0.019
3077 - 3489	0.941 ±0.018	0.975 ±0.008	1.000 ±0.004	1.000 ±0.004	0.885 ±0.019

TABLE 5.3 Reconstruction Efficiencies

Run Period	d_0 <1.5 cm (per trk)	$t_m - t_c$ -3.< <2. ns (per trk)	$\langle z_0 \rangle$ <6.0 cm (per event)	$\lvert t_1 - t_2 \rvert$ >5.0 ns (per event)	Total Efficiency 2-prong event
638 - 1385	1.000 ±0.004	0.996 ±0.004	1.000 ±0.010	1.000 ±0.008	0.992 ±0.017
1421 - 1571	1.000 ±0.006	0.987 ±0.009	1.000 ±0.016	1.000 ±0.013	0.974 ±0.030
1680 - 2200	1.000 ±0.013	0.986 ±0.013	1.000 ±0.013	0.949 ±0.035	0.923 ±0.051
2201 - 2325	1.000 ±0.021	0.979 ±0.021	1.000 ±0.054	0.960 ±0.039	0.920 ±0.083
2352 - 2829	1.000 ±0.004	0.992 ±0.006	1.000 ±0.010	0.960 ±0.018	0.944 ±0.024
2834 - 3041	1.000 ±0.007	0.993 ±0.007	1.000 ±0.015	1.000 ±0.013	0.987 ±0.027
3077 - 3489	1.000 ±0.011	0.989 ±0.011	1.000 ±0.028	0.957 ±0.029	0.936 ±0.049

TABLE 5.4 Selection efficiencies

5.6 Radiative Corrections

The contribution of higher order diagrams to the measured cross section was calculated using the programs of Berends et al[13]. The data is corrected in order to derive the contribution of the zeroth order graphs alone. This permits comparison of the results with other experiments.

Figure 5.3 shows the results of an analytic integration program which used the cross section for the Bhabha process calculated to order α^3 and integrated over a phase space defined by simple cuts on the maximum acollinearity and minimum energy of the 2 charged particles in the Bhabha event. Figure 5.3 shows the contributions from the bremsstrahlung and virtual components. Figure 5.4 shows the region of integration on a simple phase space diagram.

Berends et al[18] have implemented the cross section formula in a Monte Carlo event generator. This has the advantage that it permits a realistic evaluation of the radiative corrections whilst imposing complex cuts such as complicated detector geometries. This generator has been used extensively for the work of both this and the next Chapter.

5.7 Monte Carlo simulation of Bhabha Scattering

This section describes the 2 Monte Carlo models of the detector which were used in conjunction with event generators and real data analysis al gorithms to produce predictions of the acceptances for real data events.

5.7.1 E.G.S. (Electron Gamma Showers) This simulation of the apparatus, and the interaction of particles with it, used the EGS package which was introduced in Chapter 3.

The detector model was based on the TASSO Central Detector as specified in Table 5.5. Each substantial layer of material in the Central Detector was modelled by a thin semi-infinite cylinder of the

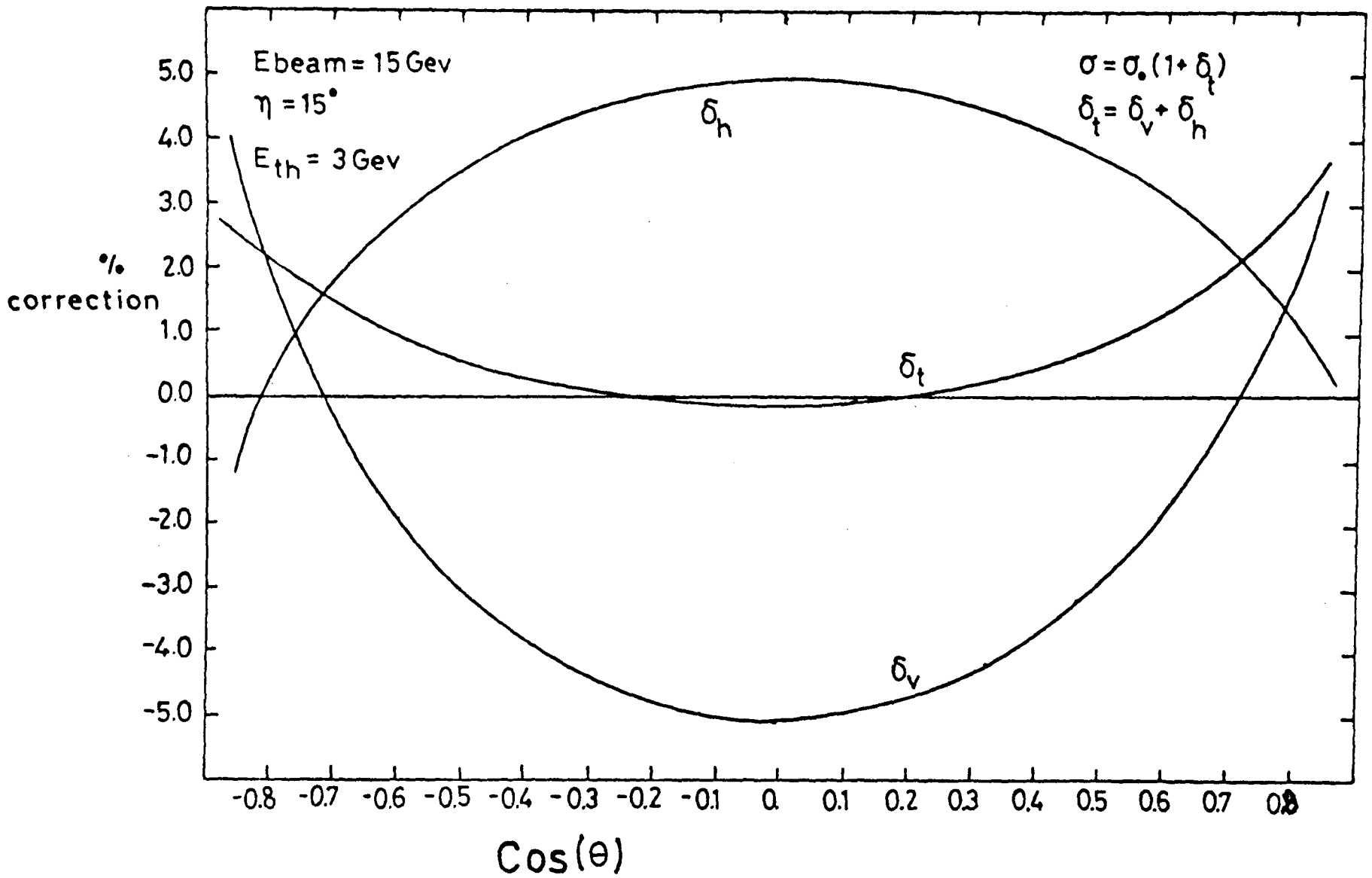

Figure 5.3 Radiative correction to Bhabha scattering. This is the result of an analytic integration using the programs of Berends.

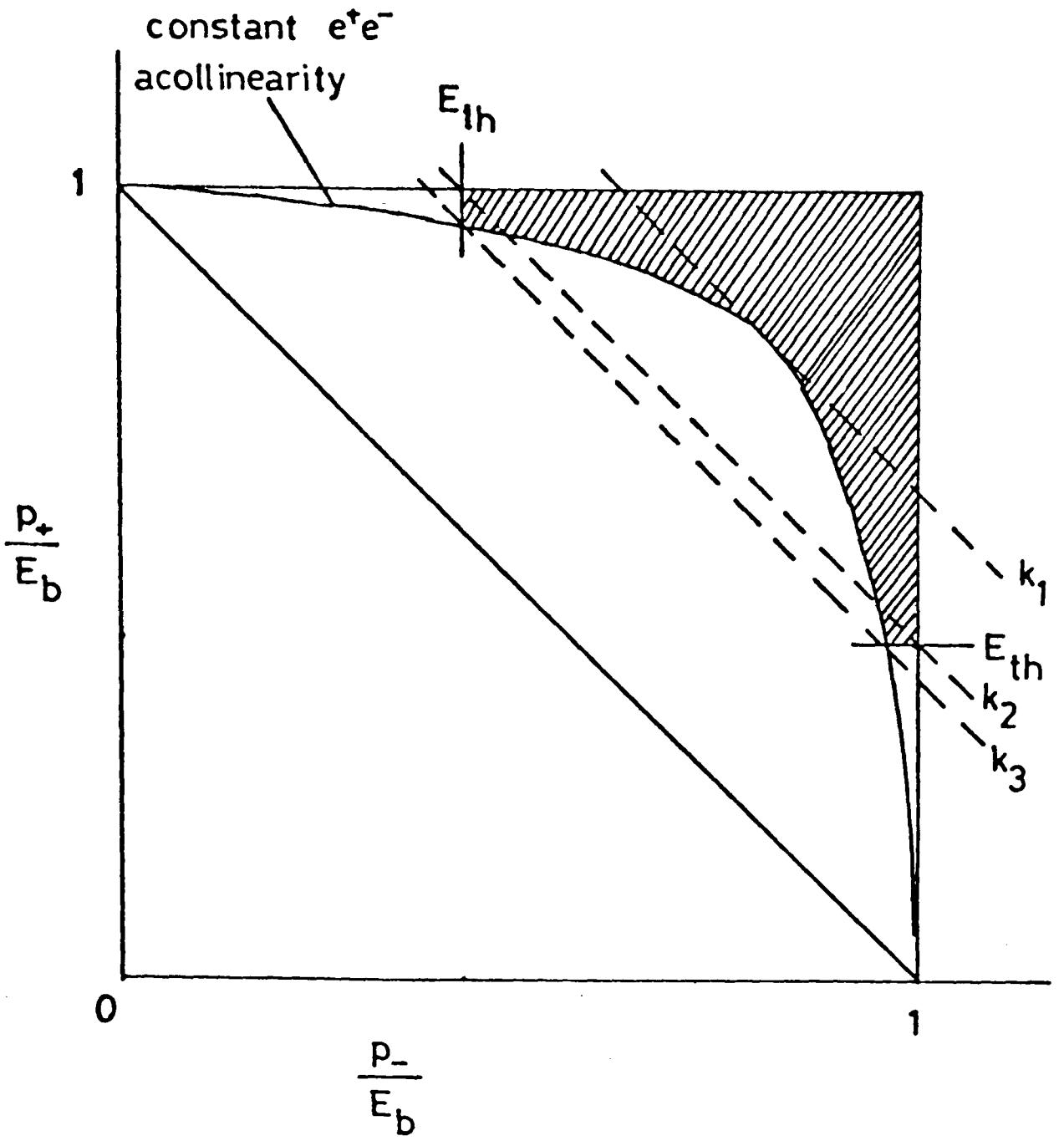

Figure 5.4 Phase space diagram for the analytic integration of the radiative Bhabha process. The shaded area represents the allowed phase space after applying simple cuts on the energies of the charged particles and their acollinearity.

Material in the TASSO Inner Detector

	Mean Radius (cm)	Thickness (cm)	X/X_0
1) Beam pipe			
Al		0.4	0.045
Rohacell		0.6	0.003
Kapton		0.0025	0.001
PVC		0.45	0.010
Al cooling pipe			0.002
	13.4		0.061
2) Pipe counters			
Scintillator		0.5	0.0116
Al foil		0.0050	0.0005
Wrapping		0.01	0.0003
	15.1		0.012
3) CPC			
Expanded Polystyrene		7.0	0.0030
Epoxy, 24 x 0.09		0.21	0.0063
Copper, 8 x 0.04/1.2		0.027	0.0186
Kapton, 8 x 0.075		0.060	0.0021
Mylar , 2 x 0.075		0.015	0.0005
Al foil		0.020	0.0022
Tungston Anode wires			0.00003
Gas (Argon + Isobutane)		5.6	0.00045
	23.3		0.033
4) Synchroton Radiation Shield*			
Al -	32.0	0.20	0.022
Sn	32.0	0.06	0.050
			0.072
	32.0		
5) Drift chamber			
Fiberglass	32.5	0.49	0.024
Argon gas	79.5	90	0.008
			0.032
Total	26.1		0.210

* Installed Dec. 1979 after run 1571. This represents about 60 % of the solid angle. About 30 % of the solid angle has the 2.0 mm Al replaced with 0.125 mm mylar. The proportional chamber rail system is in the remaining 10 %. Typically there are about 1.5 cm Al in this region.

Table 5.5 Specification, used in E.G.S. simulation, for the material of the Central Detector.

appropriate radiation thickness of an appropriate material at the mean radius of that layer. The synchrotron radiation shield between the CPC and Drift Chamber was installed for all the data collected during 1980. It adds about 50% extra material to the path of a normally incident electron.

All shower particles were propagated through material until their energy fell below a negligible level of 100 Kev. This cutoff was determined by lowering the threshold until negligible differences in the results were found. Every charged particle which emerged out of the layer representing the inner wall of the Drift Chamber was counted as a reconstructed track if its transverse energy was above 200 Mev. This cutoff was dictated by the steep falloff of the efficiency of the FOREST trackfinding program at this momentum.

5.7.2 SIMPLE

The SIMPLE Monte Carlo was developed as a general Monte Carlo for detectors at storage rings. Its name refers to its ease of use and adaptation rather than the sophistication of its representation of the detector. The TASSO version originally modelled the central tracking chambers of TASSO. The author added his own representations of the shower counter systems, both HASC and LABC, using geometry routines from data analysis routines. SIMPLE used a less sophisticated parameterisation of the interactions of electrons and photons than EGS. Appendix 2 explains some of the formulae which explain the interaction of electrons and photons with matter in the high energy particle regime appropriate to the study of this thesis. In SIMPLE, photons of energy above 100 Mev were given a momentum independent probablity of $0.777\frac{X}{X_0}$ to pair convert in a detector element of thickness X and a material of radiation length X_0. The energy of the initial particle was correctly shared between the produced electron positron pair using the formula of Tsai[54]. Electron

bremsstrahlung in thin layers was treated by the parameterisation of the photon spectrum given by Tsai[54]. For any thin layer of TASSO all the bremsstrahlung energy was treated as the radiation of a single photon. Photons with energies less than 50 Mev were ignored by SIMPLE. SIMPLE had advantages over the EGS simulation as it was faster, it included the interactions of hadrons, and it included a fuller geometry of the apparatus including elements beyond the Drift Chamber. It also simulated, more correctly, the hits in the tracking chambers, and their fitting to circles as performed in FOREST. The SIMPLE Monte Carlo was used for the determination of correction factors in the Bhabha analysis, for background estimates and in the analysis of the eeγ reaction of Chapter 6.

The effect of the track multiplicity, momentum and acollinearity cuts was investigated using the Monte Carlo together with the Berends Bhabha event generator.

5.8 Results of Monte Carlo Simulation

The result of the EGS Monte Carlo simulation of Bhabha events in the TASSO detector is summarised in Figures 5.5 to 5.8. Figure 5.5 shows the acollinearity of selected Bhabha events from the data compared with the results of the Monte Carlo simulation. Good agreement is obtained. For acollinearity angles less than 2 degrees this distribution is dominated by the experimental resolution of the Drift Chamber. At angles greater than this the effects of radiative corrections are the dominant contribution. Figure 5.6 shows good agreement between the momentum distributions of the data and Monte Carlo.

The efficiency factor for selecting Bhabha events after applying the momentum and multiplicity cuts to the Monte Carlo is shown in Figure 5.7. The efficiency is seen to be fairly flat for $|\cos(\theta)| < 0.5$. However at the edge of the angular acceptance, as tracks traverse greater amounts of matter, the efficiency begins to fall steeply. This is unfortunate because the Bhabha cross section rises steeply here and for a precise

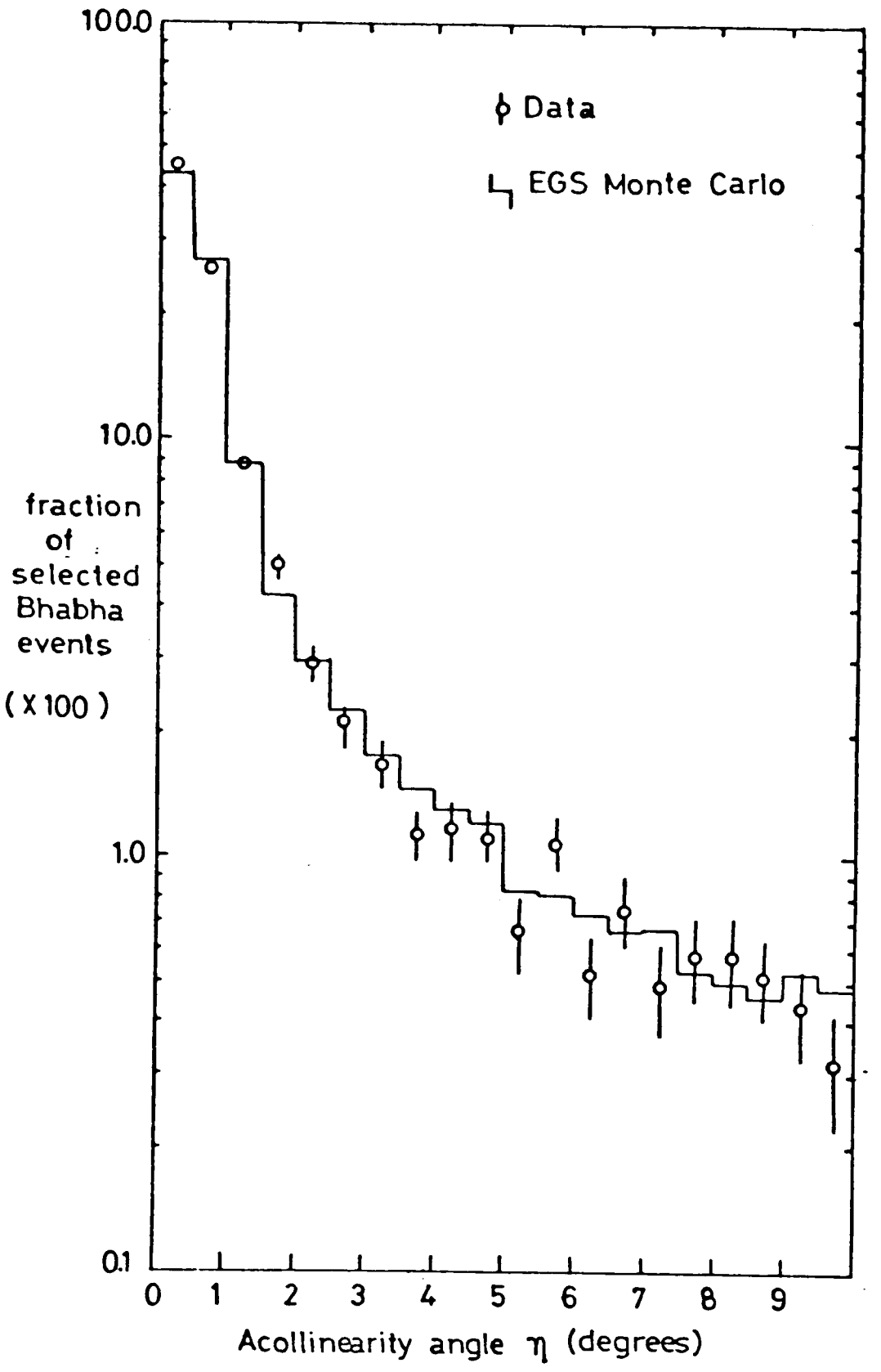

Figure 5.5 Acollinearity distributions of data and E.G.S. Monte Carlo simulation.

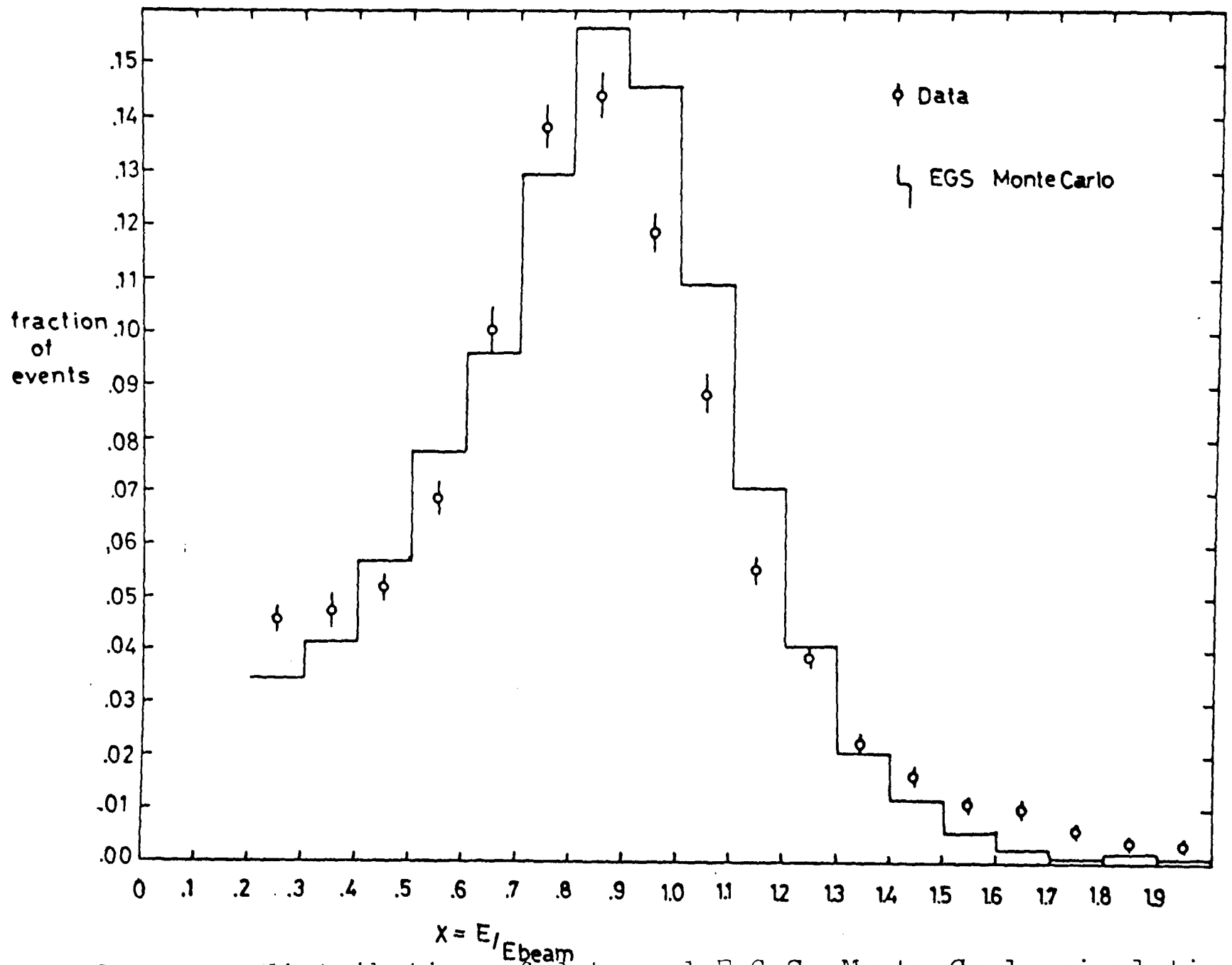

Figure 5.6 Momentum distribution of data and E.G.S. Monte Carlo simulation.

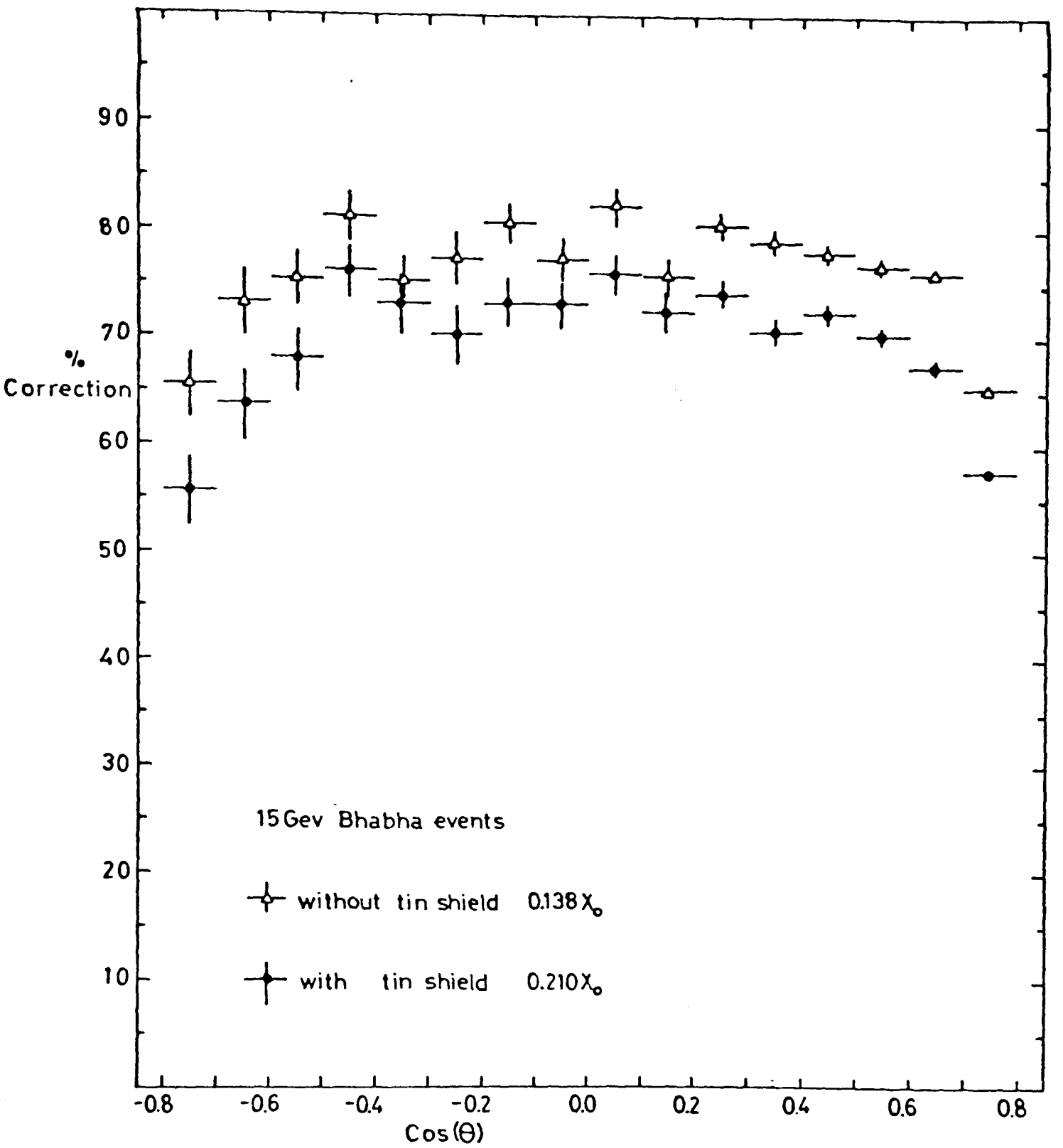

Figure 5.7 E.G.S. prediction of the efficiency of detecting Bhabha events after interacting in the TASSO detector. (Simple energy and accollinearity cuts are used to identify Bhabha events).
The effect of the synchrotron radiation shield is illustrated.

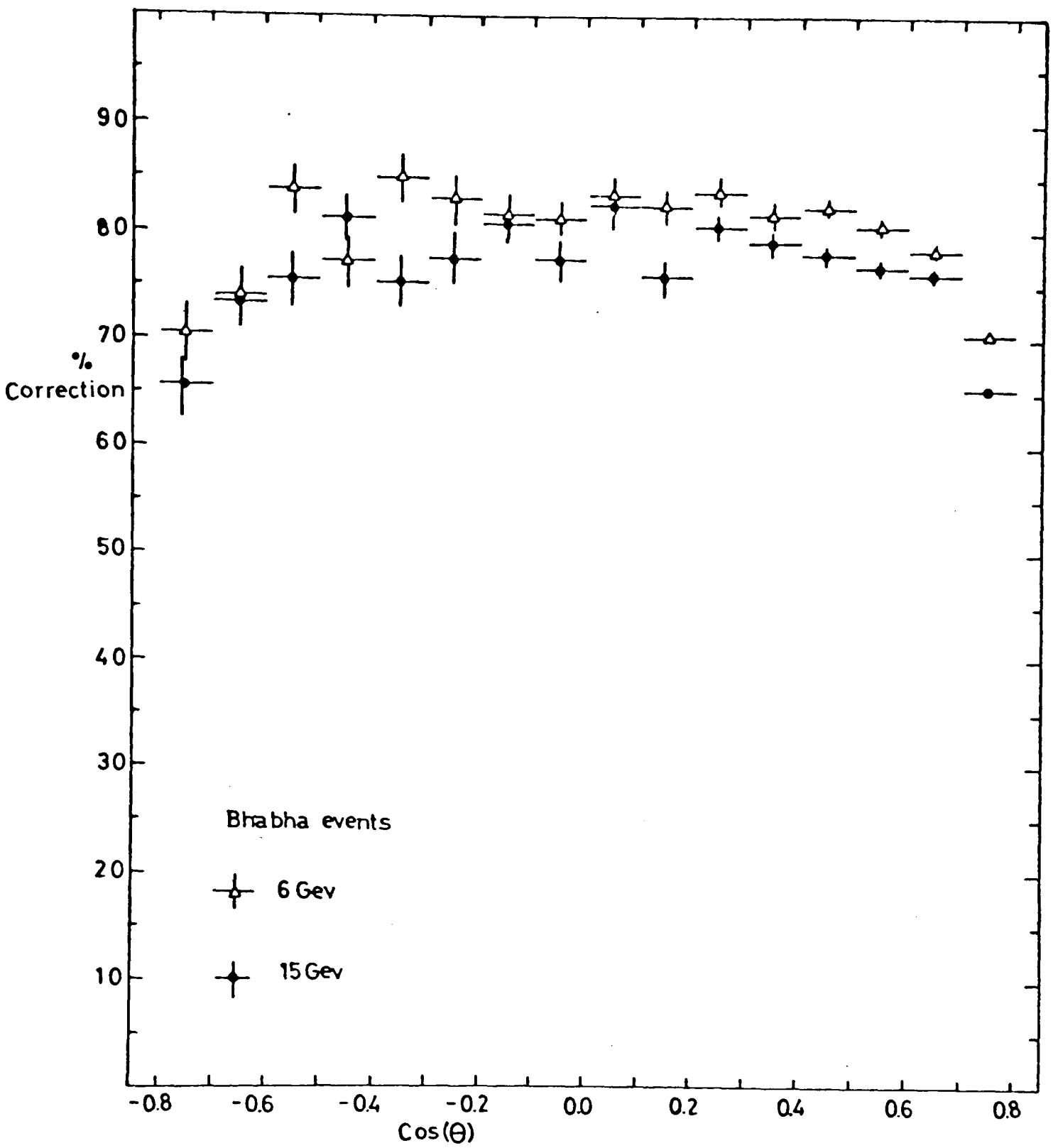

Figure 5.8 E.G.S. prediction of the efficiency of detecting Bhabha events after interacting in the TASSO detector. The energy dependence of this correction is illustrated.

determination of the total cross section this is the angular region where one would like to know the efficiency most reliably.

Figure 5.7 illustrates the dependence of the efficiency on the presence of the synchrotron radiation shield. Figure 5.8 shows the energy dependence of the EGS correction.

The total efficiency for detecting 2 prong Bhabha events in the TASSO apparatus is given in Table 5.6. The results of 2 methods are used. The first method multiplies the trigger, reconstruction, selection, and acceptance efficiencies, determined above, together. This assumes they have been determined in a manner such that they are independent quantities. The second method is the result of using the trigger and reconstruction efficiencies as input to the SIMPLE Monte Carlo and allowing SIMPLE to use its own parameterisations for interactions. It is seen that both methods lead to the same results. They also give similar angular efficiency corrections. The results of the first method were used for final result calculations.

5.9 Background Contamination

The contribution of events from processes which have a topological signature which could mimic Bhabha events is discussed below.

5.9.1 Heavy Lepton Pair production

TASSO have measured the muon and tau pair production cross sections and found them to agree well with QED and electroweak theories.[55] The contribution of these events to the Bhabha signal was estimated using QED event generators developed by Berends et al in conjuncton with the SIMPLE model of the apparatus. Muon pair events have the same topological signature in the Central Detector of TASSO as Bhabha events but the cross section is much smaller as only the annihilation graph is involved. Tau pair events have the same cross section as muon pairs but their contribution is even smaller as they decay with a lifetime of 10^{-13}

Run Numbers	Efficiency derived from E.G.S. x efficiency factors	Efficiency value from the SIMPLE Monte Carlo
638 - 1385	0.57 ± 0.03	0.52 ± 0.03
1680 - 2200	0.51 ± 0.03	0.49 + 0.03
2201 - 2325	0.49 ± 0.03	0.50 ± 0.03
2352 - 2829	0.40 ± 0.04	0.43 ± 0.03
2834 - 3041	0.40 ± 0.05	0.38 ± 0.03
3077 - 3489	0.44 ± 0.04	0.45 ± 0.03

Table 5.6 Efficiency of identifying Bhabha events after all factors (trigger, reconstruction, radiative corrections and interactions) are considered.

seconds, via the weak interaction. Their decays involve undetected neutrinos or neutral particles and the resultant events are failed by the Bhabha selection cuts on the multiplicity, acollinearity or energy of the charged tracks. Figure 5.9 shows, relative to the Bhabha cross section, the contribution of the muon pair background as a function of cos(θ). The tau pair contribution was determined to be approximately 10% of the muon pair contribution. The size of the heavy lepton contamination of the total cross section measurement is approximately 6%.

5.9.2 Two Photon Annihilation

This process involves the bremsstrahlung and subsequent interaction of virtual photons from the initial state electron and positron. The spectrum of photons is peaked at low values of k, the photon momentum and thus the initial particles suffer only minimal deflection and escape detection within the central part of the detector. The detected particles tend to have very low momentum and to be boosted along the z direction because the photons are of unequal energy and the center of mass of their interaction is moving along the z direction. Most 2γ events are eliminated by the energy and acollinearity cuts. The remaining contamination was estimated using a Monte Carlo generator due to Vermaseren at al[56]. Their contribution was found to be negligible.

5.9.3 Hadron production from single Photon Annihilation

The contamination from single photon annihilation production of hadrons is minimal as the average detected multiplicity of these events is about 20. A Monte Carlo simulation using the generator of Meyer et al [57], which utilised a Feynman-Field parameterisation for hadron production, gave a negligible contamination.

5.9.4 Cosmic Ray Events

The cosmic ray flux was severely suppressed by the time gating and trigger requirements of the accelerator and detector. It was found that about 10% of all accepted online triggers were cosmic ray events. They were rejected by cuts on $|d_0|$ and $\langle z_0 \rangle$ but the most efficient cut for their removal was the $|t_1-t_2|$ timing cut. The residual contamination was estimated by selecting events from the 2 prong tapes with the same cuts as for Bhabhas but requiring $|\langle z_0 \rangle|$ to be between 6 cms and 12 cms. The distribution of cosmics in $\langle z_0 \rangle$ is expected to be flat and therefore the contamination of cosmics in the $\langle z_0 \rangle$ range of the selected data can be estimated. This background contamination mainly populates the central $\cos(\theta)$ bins as most of the cosmic rays pass vertically through the apparatus. Figure 5.9 show the angular distribution of events , relative to the Bhabha cross section, used to estimate this background. The contamination of the total cross section measurement is approximately 1%.

5.10 Distributions for the selected data

Figure 5.10 shows data distributions for the Bhabha events which were selected using the cuts described in Section 5.3.2. The double peak structure in the d_0 distribution is caused by the intersection point of interactions moving away from the nominal (0,0,0) coordinates. The data can be corrected to give a single peak by determining the position of intersection of the beams using the vertex position as derived by extrapolating tracks in hadron events to a single point. The cuts used on d_0 selection were sufficiently loose that this was not necessary.

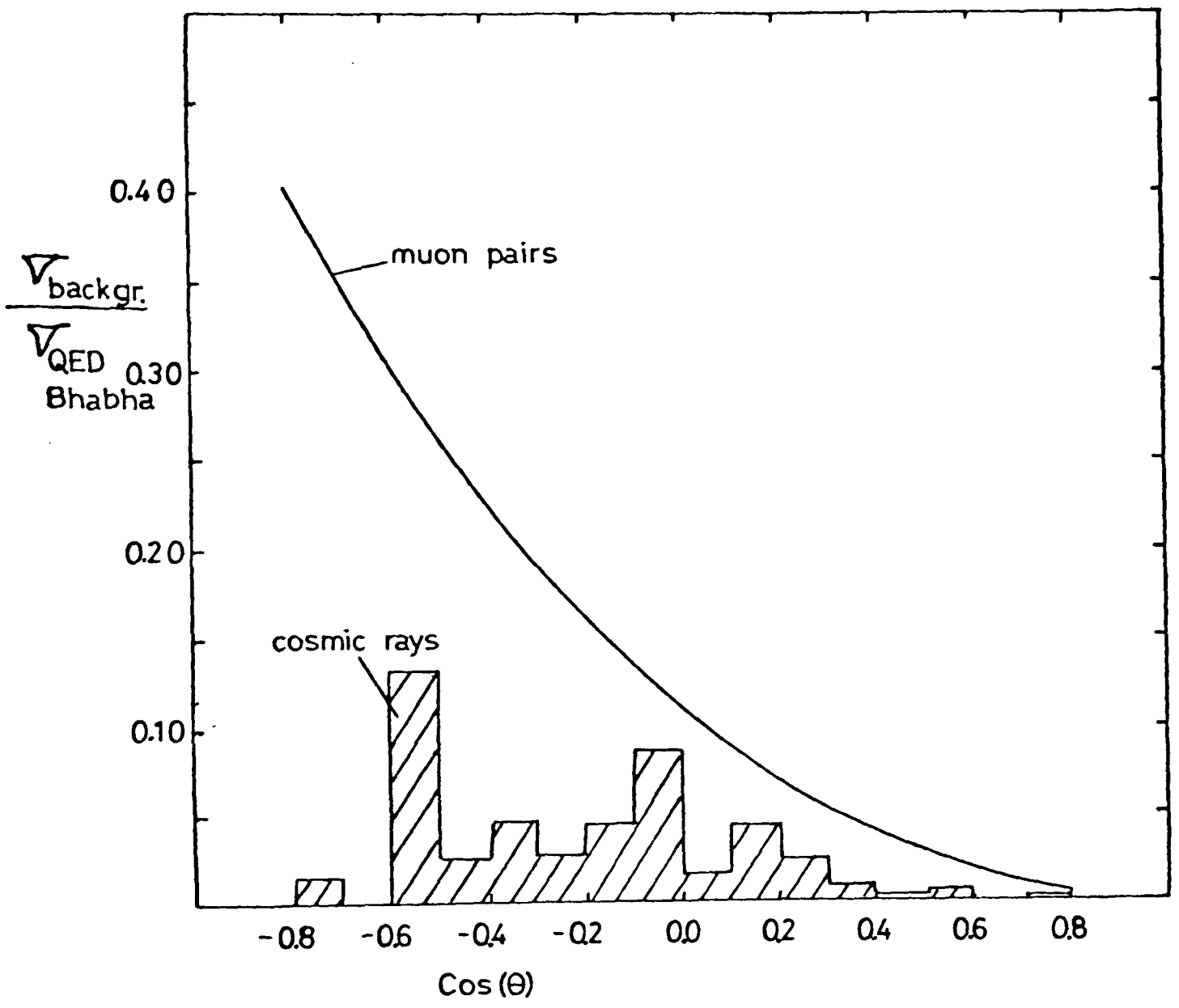

Figure 5.9 Background contamination of the Bhabha signal.

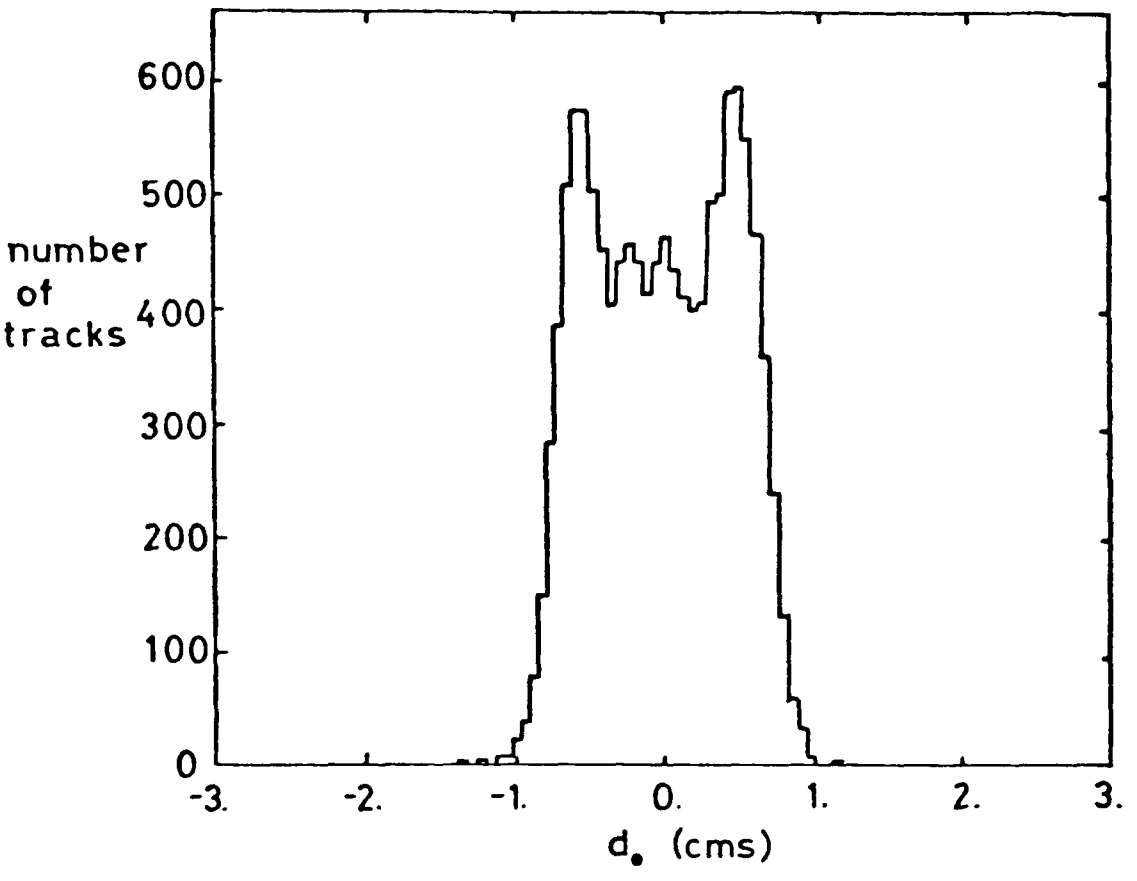

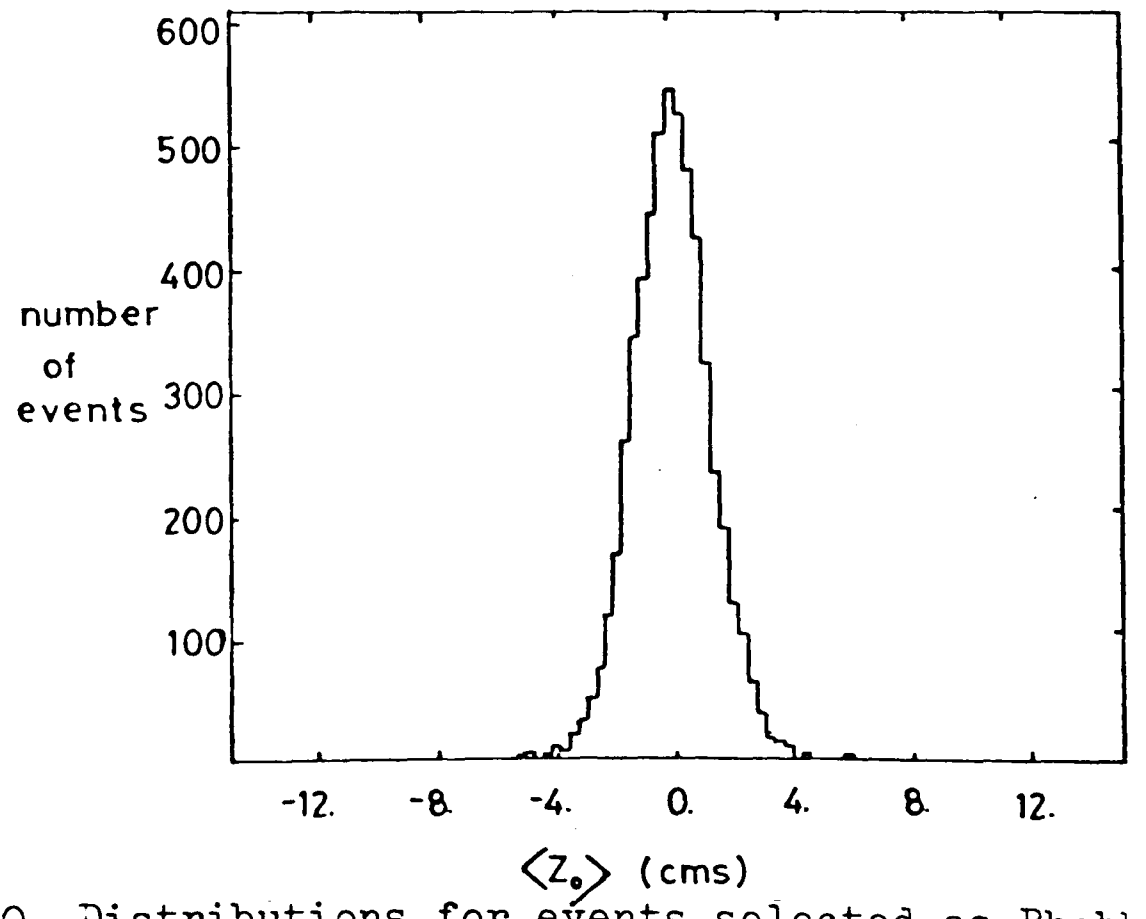

Figure 5.10 Distributions for events selected as Bhabha scattering events.

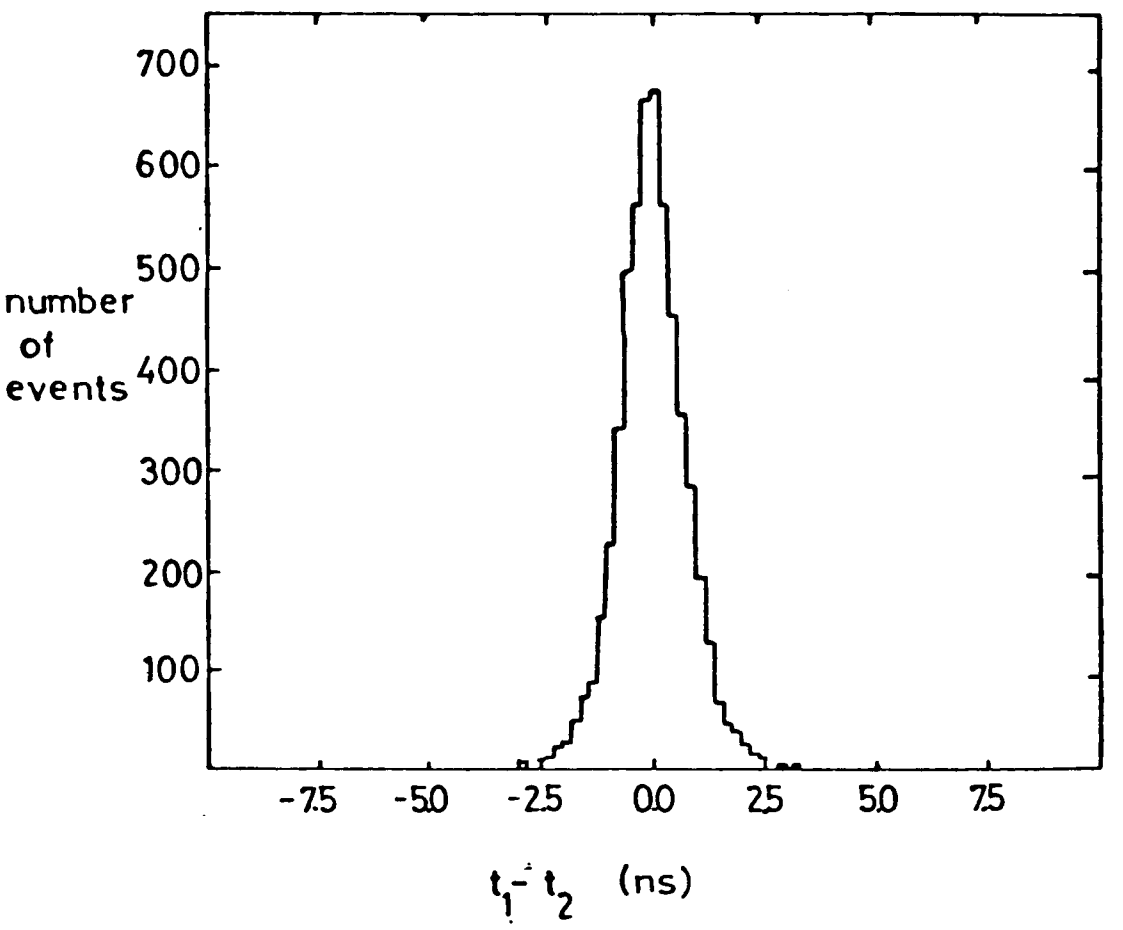

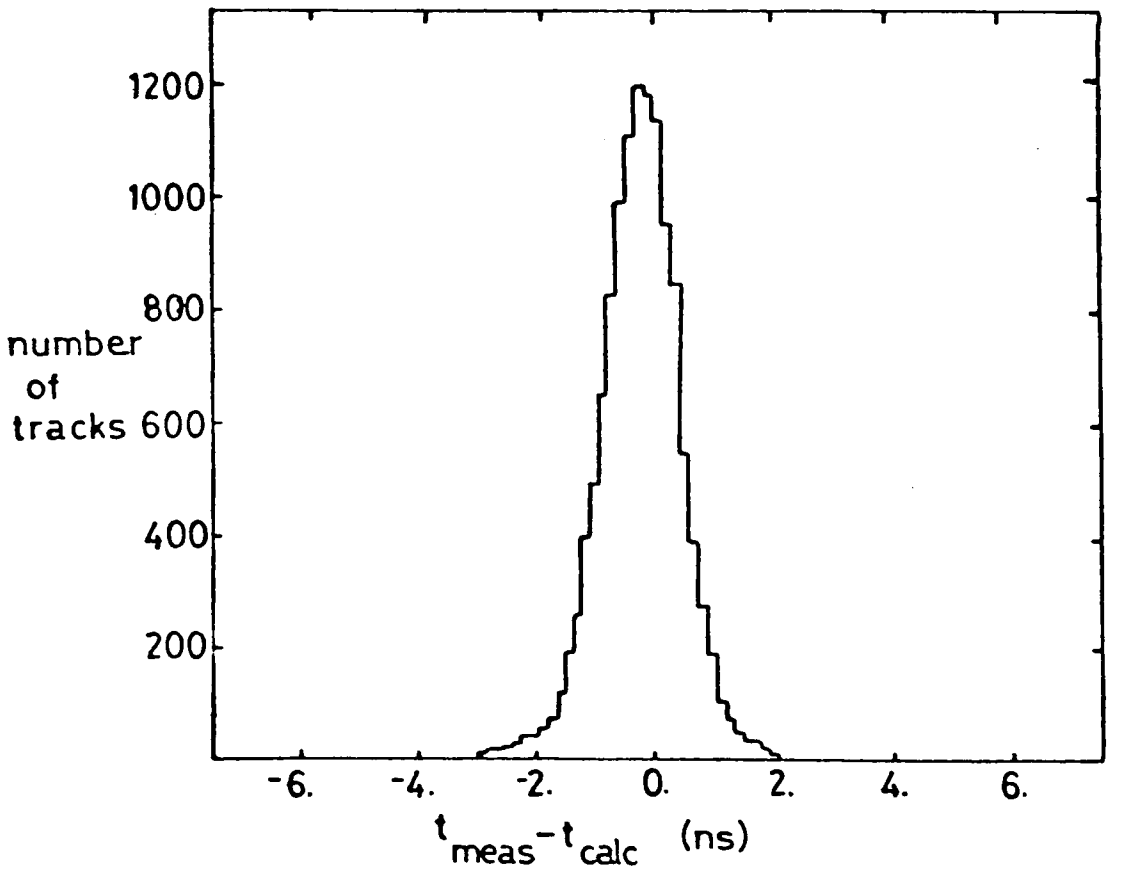

Figure 5.10 (cont.) Distributions for events selected as Bhabha scattering events.

5.11 Results of cross section determination

5.11.1 Total cross section

Table 5.7 shows the value of the total cross section measurements in bins of energy and divided to distinguish data samples from the periods when the synchrotron radiation shield was or was not present. Extensive studies of the data divided into smaller energy bins and shorter data periods did not indicate any variations in the results presented to within the statistical accuracy of the samples. The one anomalous data period is that for the data sample collected after run number 3100 in October 1980. The value of the cross section is approximately 1.5 times that expected. Studies failed to indicate the origin of this discrepancy, which is too large to be ascribed to any reasonable systematic or physics source. Other members of the collaboration experienced similar difficulties in using this section of data for absolute cross section determinations. For these reasons this data sample is ignored in all that follows.

The values of the total cross section of Table 5.7 are systematically lower than that expected from standard QED if only the statistical error of the measurements is considered. The sources of systematic uncertainties in normalisation arise from the luminosity measurement of the Forward Detector and from the uncertainty in the determination of the efficiency factors input to the cross section calculation. Typical values for these errors are:

Forward detector luminosity	4% (see section 2.4.1)
Trigger efficiency	2%
reconstruction efficiency	2%
Selection efficiency	2.5%
EGS Monte Carlo simulation	2%
Radiative corrections	1.5%

Squared Centre of mass energy s (Gev^2)	Luminosity (nb^{-1})	Number of events	$\frac{(\nabla)\ \text{measured}}{(\nabla)\ \text{QED}}$
144.0	96.5	639	0.875 ± 0.036
483.0	37.5	82	0.925 ± 0.[illegible]10
895.4	391.9	428	0.981 ± 0.049
939.7	2158.6	2374	0.960 ± 0.020
1116.4	1243.1	807	0.911 ± 0.021
1217.7	3530.2	2242	0.938 ± 0.021
1339.0	54.7	49	1.378 ± 0. 20
*1290.8	606.8	371	1.530 ± 0.067
Average of all data with beam energy above 10 Gev			
1100.0	7416.4	5984	0.949 ± 0.013

Table 5.7 Results of Bhabha total cross section determination.

* This data period is not used in average calculations or fits.

The trigger, reconstruction and selection errors are estimated from the statistical accuracy of the data samples used in the efficiency measurement. The Monte Carlo error is that expected if the thickness of the material of the inner detector is wrong by approximately 0.01 radiation lengths. The radiative correction error reflects the uncertainty in the knowledge of terms such as the hadronic vacuum polarisation, which require experimental input for their calculation. Combining the contribution of all these terms in quadrature leads to an estimate of the systematic uncertainty in the total cross section measurement of 6%. The data and theory become readily compatible when an uncertainty of this size is considered.

Table 5.7 shows that, within statistical accuracy, the high energy results from the periods when the synchrotron radiation shield was or was not present are compatible. This gives confidence that the corrections from the EGS Monte Carlo simulation are of the correct size. Figure 5.11 shows the total cross section as a function of the beam energy after these periods have been combined. The value of the cross section decreases by a factor of 10 over the range of energies studied.

5.11.2 Angular cross sections

Figure 5.12 shows the differential angular cross sections for the data presented in Table 5.7. The shape of the distributions agree, within statistical accuracy, well with the QED prediction even though, over the full angular range, the cross section decreases by nearly 2 orders of magnitude. The corrections applied to the data, such as background subtractions, are significantly different for different parts of this angular range. Figure 5.13 shows the angular cross section divided by the QED cross section for all the data collected with beam energy greater than 10 Gev. The curve is systematically low but shows little significant angular discrepancy. This distribution is compared to several theories in the next Section.

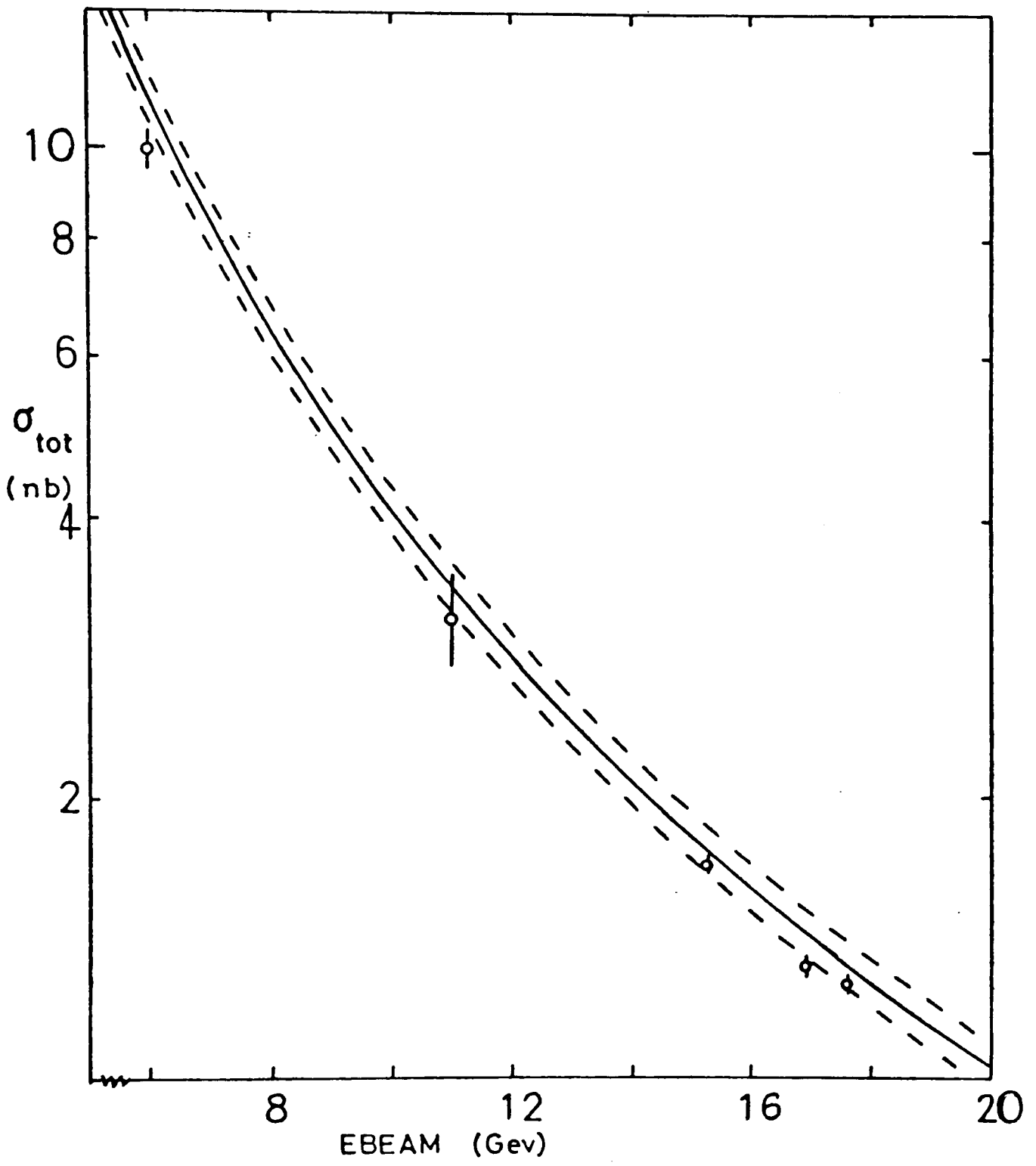

Figure 5.11 Total Bhabha cross section as a function of beam energy. The solid line is the QED lowest order prediction. The dotted lines show the effect of a 5% systematic error.

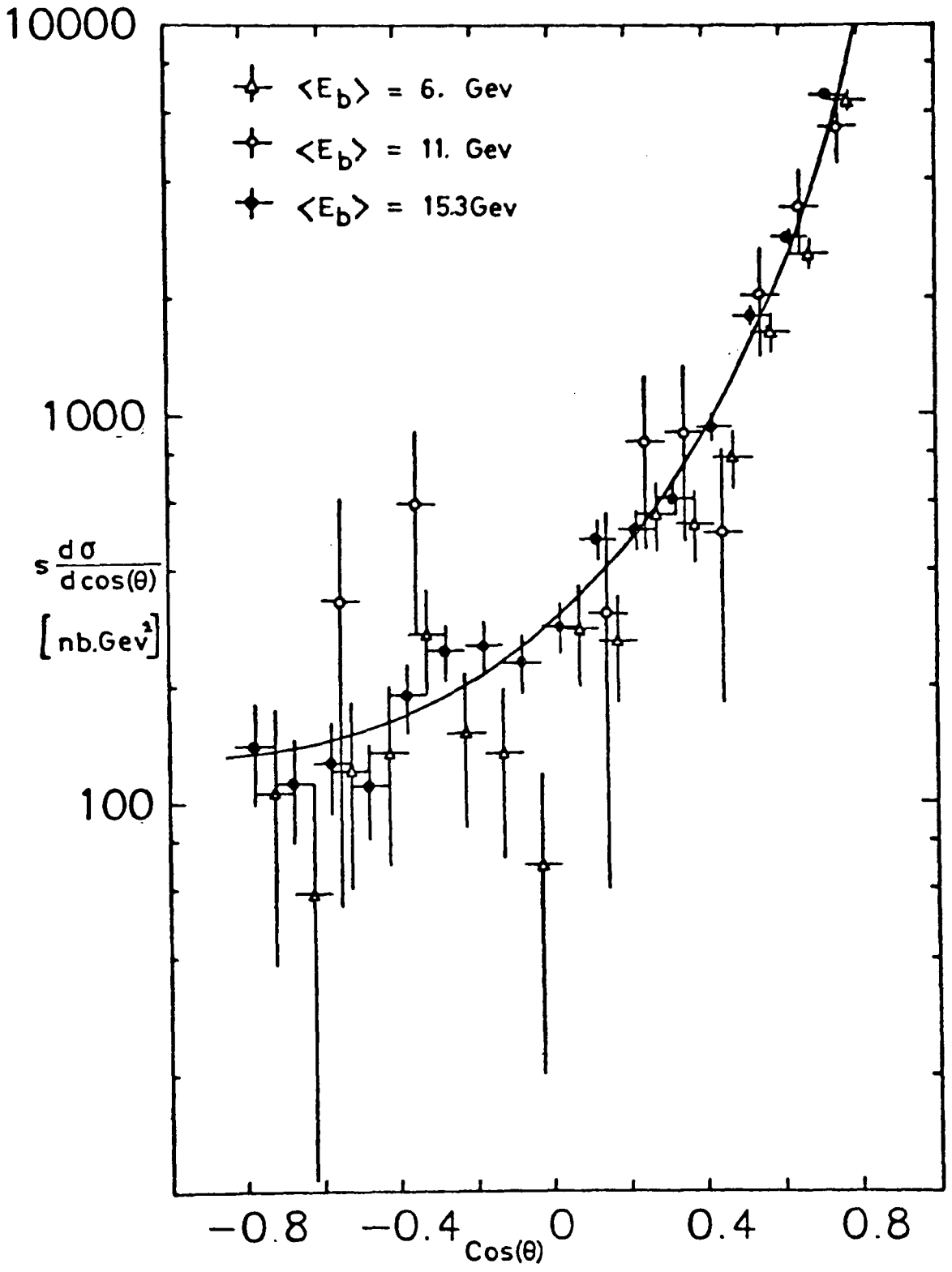

Figure 5.12 Measured differential angular Bhabha cross section.
The solid line is the QED prediction.
This is the data from 1979.

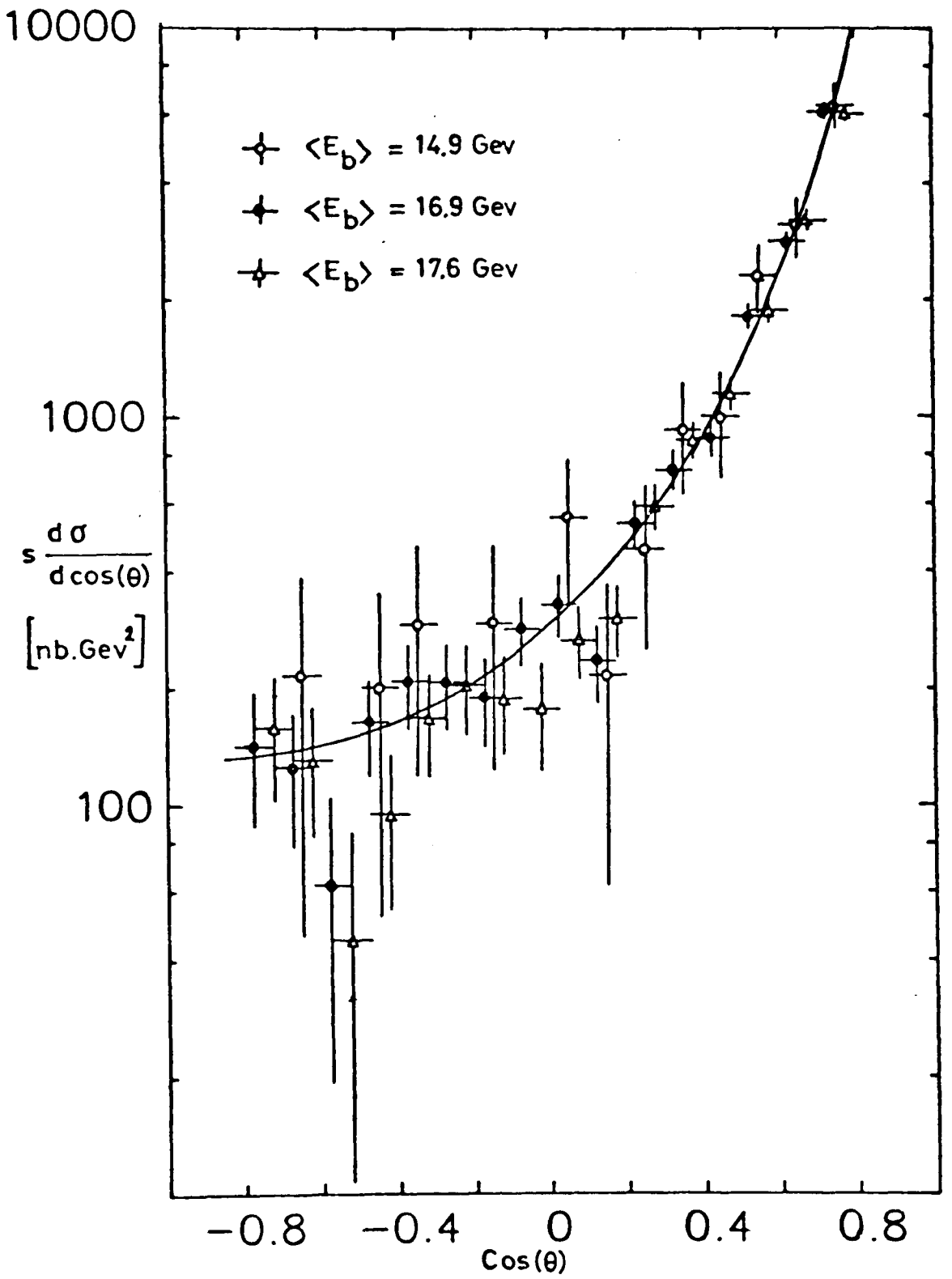

Figure 5.12 Measured differential angular Bhabha cross section
The solid line is the QED prediction.
This is the data from 1980.

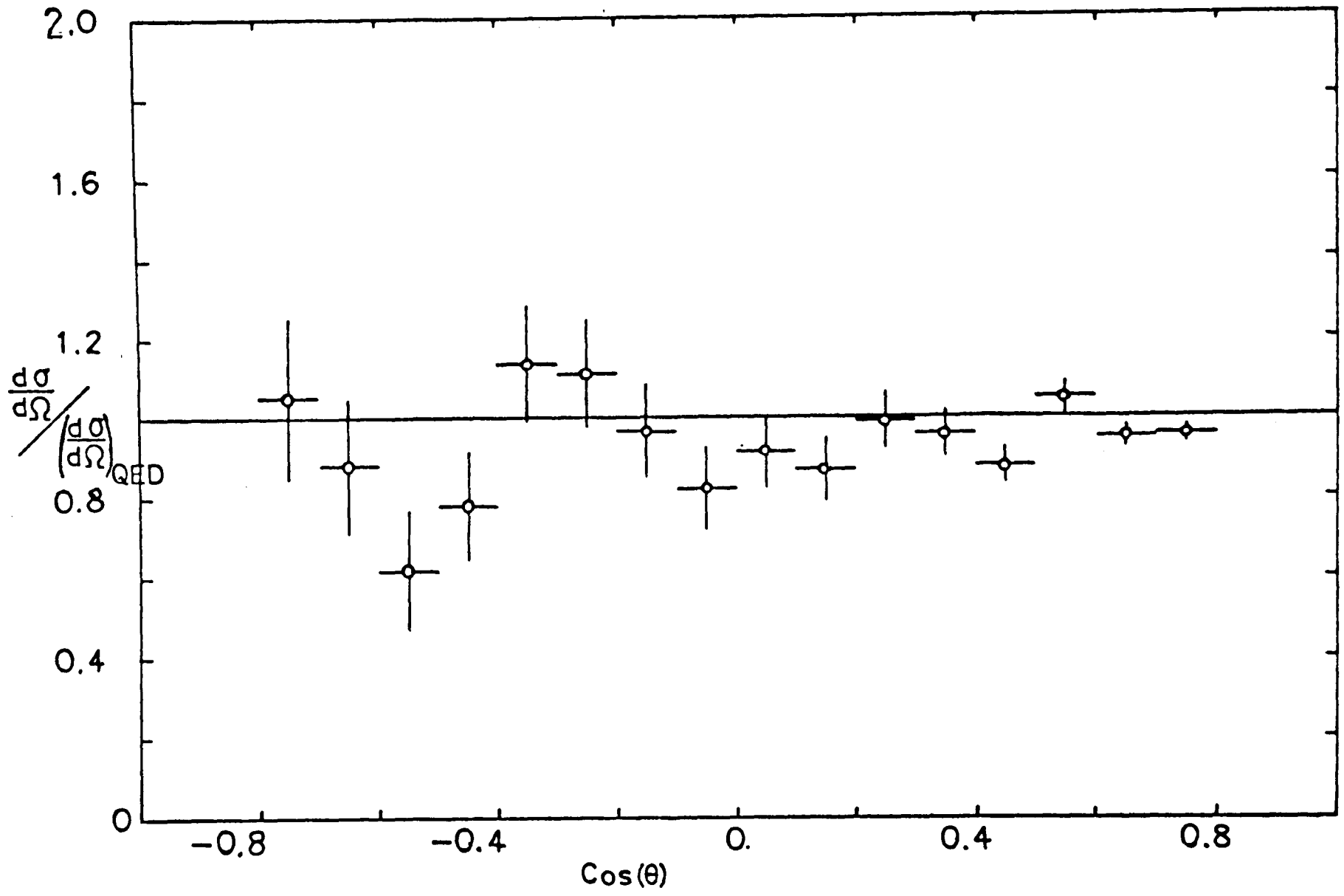

Figure 5.13 Ratio to QED prediction of measured angular cross section for data with E_b > 10Gev.

5.12 Interpretation of results

The candidate theories of Bhabha scattering at high energies, QED and electroweak, are tested by fitting the angular cross section formulae of these theories to the measured cross section results of the last section.

The fitting program used was MINUIT from the CERN program library. All fits were performed by minimising the simple χ^2 :

$$\chi^2 = \sum_i \frac{(N \times F_{meas} - F_{theory})^2}{(N \times \Delta F)^2} \qquad (5.13)$$

where $F=\frac{d\sigma}{d\Omega}$, ΔF is the statistical error of the measurement and N is a normalisation parameter. The error includes a systematic point to point contribution in quadrature with the statistical errors of the points. This systematic error consists of a 2% uncertainty in the most extreme $\cos(\theta)$ bin from the Monte Carlo simulation and an error estimated to be approximately 10% of the background contribution. All points in the angular range were fitted simultaneously allowing the normalisation as a free parameter of the fit. However, as the normalisation of the data has a large systematic uncertainty and therefore contains little information of physics interest, the values quoted for the other parameters of the fit are taken at the point where the normalisation parameter assumes its best fitted value for the theory under test. An alternative strategy was to normalise by the measured cross section value in the bin centred at $\cos(\theta)=0.75$. This meant that the forward detector luminosity was not used and all measurements were derived solely from Drift Chamber data. For the data presented here, the 2 methods gave identical results as the cross section values divided by the QED expectation were the same for the two bins which contained the majority of the data, $\cos(\theta)=0.75$ and $\cos(\theta)=0.65$. Comments on the correlation of the normalisation parameter with the other parameters of the fit are made below. The χ^2 of all the

fits was of the order of 20 for 13 or 14 degrees of freedom (16 data points - 2 or 3 fitted parameters). The majority of this was contributed by the points in the $\cos(\theta)=-0.55$ and $\cos(\theta)=0.55$ bins each of which gave 5 units to the total χ^2.

5.12.1 Derivation of confidence levels for n-parameter fits[58]

Limits on the values of the parameters of fits at various confidence levels were derived by plotting the variation of χ^2 as parameters were simultaneously varied.

For the simple case of a 1 parameter fit, P_1, the best value of the parameter is given at a value of χ^2 which we will denote by $\chi^2_{min}(P_1)$. If the fit is linear then as the parameter is varied away from the minimum the χ^2 will follow a parabolic variation. If the errors are normally distributed the 68% and 95% confidence regions correspond approximately to moving 1 and 2 standard deviations away from the minimum. This is equivalent, on average, to the χ^2 value increasing by 1 and 4 units from its minimum. Figure 5.14 shows the limits which would be derived in this case.

The case of a fit to 2 parameters, P_1 and P_2, is also shown in Figure 5.14. It illustrates the fit with N, the normalisation, and a Λ parameter as free parameters. The simultaneous variation of parameters produces contours of constant χ^2 in the P_1-P_2 plane. The projection of the χ^2 variation onto a parameter axis produces a parabolic χ^2 variation as the parameter is varied and the other parameter is held fixed. The region in the P_1-P_2 plane within which 68% or 95% of all measurements are expected to occur (given normally distributed and correlated variables) is within the χ^2 contour where the χ^2 has increased by 1 or 6 units respectively. Similarly for a 3 parameter fit the 95% confidence value is determined by the value of parameters on the contour 8 units above the χ^2 minimum.

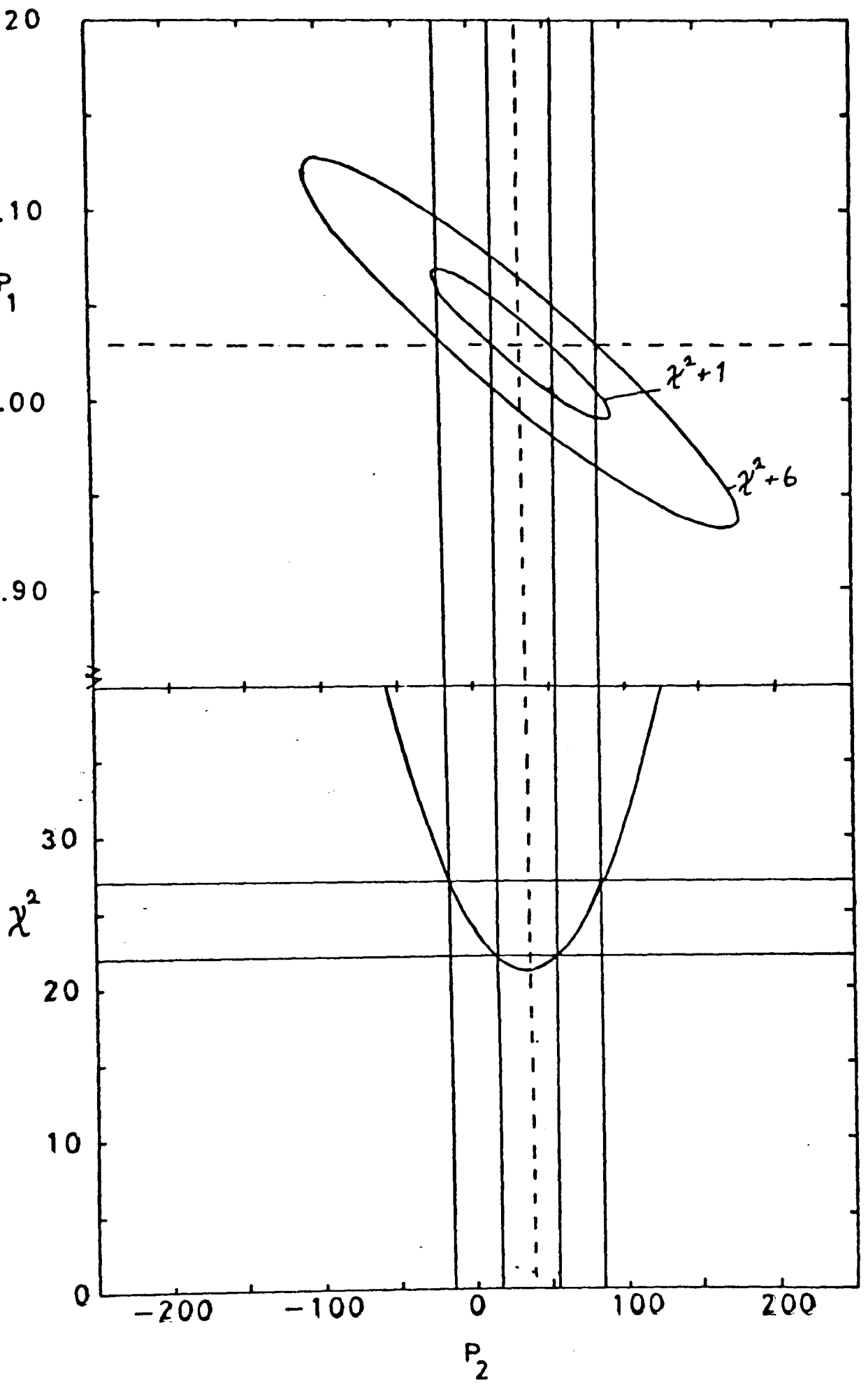

Figure 5.14 Derivation of confidence levels for a 2 parameter fit.

5.12.2 QED Λ parameters

The angular cross section was fitted to equation (1.8) in the limit that $\Lambda^2 >> s$ and $\Lambda^2 >> t$. The form factors used in the fit are of the form

$$F_s(t) = 1 + \kappa t \quad \text{and} \quad F_t(s) = 1 + \kappa s$$

where $\kappa = \frac{1}{\Lambda^2}$. The fit is best performed in terms of κ as this is the variable in which the fit is linear and therefore there is a parabolic dependence in the variation of χ^2 with the fitted parameters. Several comments about the measurement of the Λ parameters are worth noting :

a) The measurement is sensitive to both s-channel and t-channel exchange as we are able to measure the charge of the scattered lepton and hence the cross section at large backward angles where the s-channel contribution is comparable to that of the t-channel. Calorimetric experiments such as MARK-J at PETRA are unable to do this.

b) If time reversal is a good invariance all the form factors are real[3],[4].

c) Arguments based on analycity and crossing symmetry imply that in the physical region $\Lambda_s = \Lambda_t$[3],[4].

Figure 5.14 shows the variation of χ^2 with κ and N for a fit in which $\Lambda_t = \Lambda_s$. If QED was correct and the measurements were perfectly accurate the minimum would be at (κ=0,N=1). The offset is a measure of the systematic error in the measurement. A fitted value for κ of $(34 \pm 51) \times 10^{-6}$ $(\text{Gev}^2)^{-1}$ was derived at the point where N had its best value of 1.03. The error is that from the 95% confidence level contour

when N is at its best fitted value. This gives a value for the Λ parameters of

$$\Lambda_+ = 108 \text{ Gev} \quad , \quad \Lambda_- = 241 \text{ Gev} \text{ at } 95\% \text{ confidence}$$

The correlation of the value of κ derived with a variation of the normalisation parameter is quite large. For the $\Lambda_s = \Lambda_t$ fit, as we move along the 95 % confidence level contour to the point where the normalisation has decreased by 5% we get κ changing from a value of 34×10^{-6} to a value of 120×10^{-6} $(\text{Gev}^2)^{-1}$. This correspond to Λ values going from 108 and 241 Gev^2 to 74 and 129 Gev^2 respectively.

If we fit Λ_s and Λ_t seperately we get values of:

$$\kappa_s = (28 \pm 64) \times 10^{-6} \ (\text{Gev}^2)^{-1}$$

$$\kappa_t = (-88 \pm 225) \times 10^{-6} \ (\text{Gev}^2)^{-1}$$

with N= 1.046 and 95% confidence level errors.

This leads to 95% confidence level values of

$$\Lambda_{s,+} = 104 \text{ Gev} \quad , \quad \Lambda_{s,-} = 166 \text{ Gev}$$
$$\Lambda_{t,+} = 85 \text{ Gev} \quad , \quad \Lambda_{t,-} = 56 \text{ Gev}$$

If we use 100 Gev as a conservative lower limit on the value of a typical Λ parameter, then as $\hbar c$ = 197 Mev fermi, we can derive a limit of 2×10^{-3}fermi or 2×10^{-18}m for the limiting distance to which QED is a point like theory.

5.12.3 Glashow-Weinberg-Salam (GWS) Electroweak Theory

The measured cross section was fitted to the angular cross section of equation (1.20), setting g_v and g_a to the values of equations (1.16) and (1.17), to derive a value for $\sin^2(\theta_w)$. This resulted in a limit for the value of $\sin^2(\theta_w)$ of

$$\sin^2(\theta_w) < 0.65$$

For this particular fit the variation of the χ^2 with $\sin^2(\theta_w)$ was non parabolic.

5.12.4 g_v - g_a fit

The value of g_a^2 is poorly determined by fitting the Bhabha cross section alone. However, in electroweak theories an angular asymmetry in the production cross section for muon pairs is expected. This asymmetry depends chiefly on the value of g_a^2 and should be measureable at PETRA energies. TASSO have measured

$$A_{\mu\mu} = \frac{n_+ - n_-}{n_+ + n_-}$$

$$= - \frac{3\sqrt{2}\, G_F\, g_a^2\, s}{8\, e^2}$$

where n_+ (n_-) is the number of muon pair events with $\cos(\theta) > 0$ (< 0). To increase the sensitivity of the Bhabha fit the measured value of the asymmetry has been included in a simultaneous fit with the angular Bhabha cross section. The measured value of $A_{\mu\mu}$ was 0.06 ± 0.09. The result of the fit was:

$g_v^2 = -0.15 \pm 0.65$ and $g_a^2 = 0.33 \pm 0.88$ (95% confidence limit)

The values predicted by GWS theory are

$g_v^2 = 0.0016$ and $g_a^2 = 0.25$

Figure 5.15 shows the regions allowed in the g_v^2-g_a^2 plane at the 1 and 2 standard deviation points. Also shown are determinations of these parameters by neutrino scattering and electron scattering experiments. Using only the neutrino data and a model independent analysis of the electroweak interaction 2 regions are equally allowed for g_v^2 and g_a^2. The data of this thesis marginally favours the region defined by the Weinberg Salam model.

If the normalisation parameter of the data moves to a value 5% lower than the best fitted value, then g_v^2 will move to approximately -0.85. The value of g_a^2 is uncorrelated with the normalisation parameter as it is determined by the asymmetry measurement.

5.12.5 Multi boson theories

The general parameter C of equation (1.21) can be incorporated into the cross section formula of equation (1.20) by the transformation $g_v^2 \rightarrow g_v^2 + 4C$ and $g_a^2 \rightarrow g_a^2$. This modified cross section was fitted to the experimental data and a value for C of -0.03 was found. Using the 2 standard deviation upper limit value of $C < 0.08$, equations (1.22) and (1.23) were used to impose limits on the masses of the 2 bosons of the extended electroweak theories of Barger et al and De Groot at al. Figure 5.16 shows that large areas of the M_{z1} M_{z2} plane are excluded by this measurement.

The value of C is positively correlated with the value of the normalisation and therefore if the normalisation decreases by about 5%, which is the value preferred by the data, then the value of C will decrease and the limits on the boson masses will become more stringent.

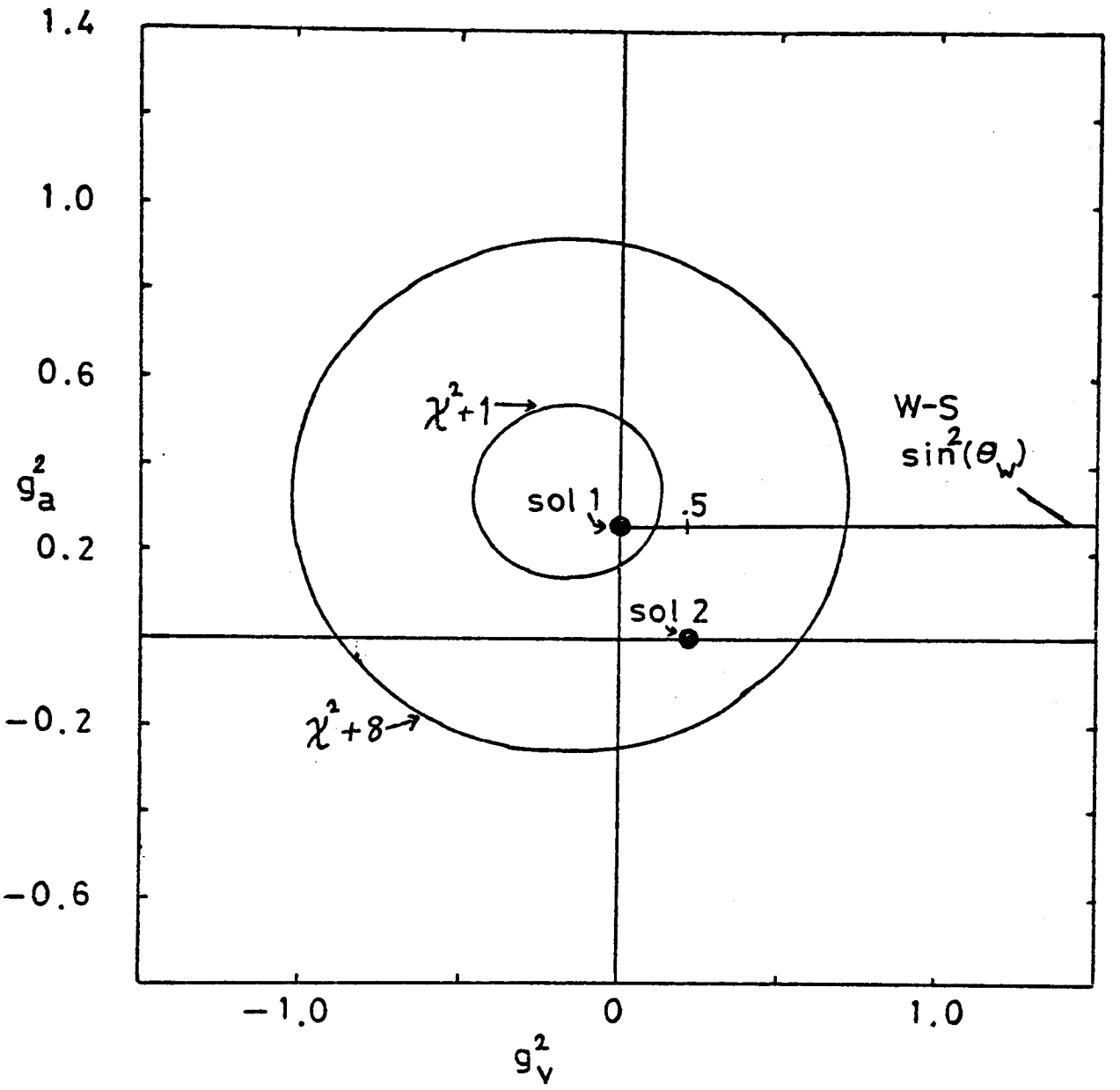

Figure 5.15 Result of $g_V^2 - g_a^2$ fit.

The 2 indicated regions are the ambiguous solutions determined from neutrino and electron scattering experiments.

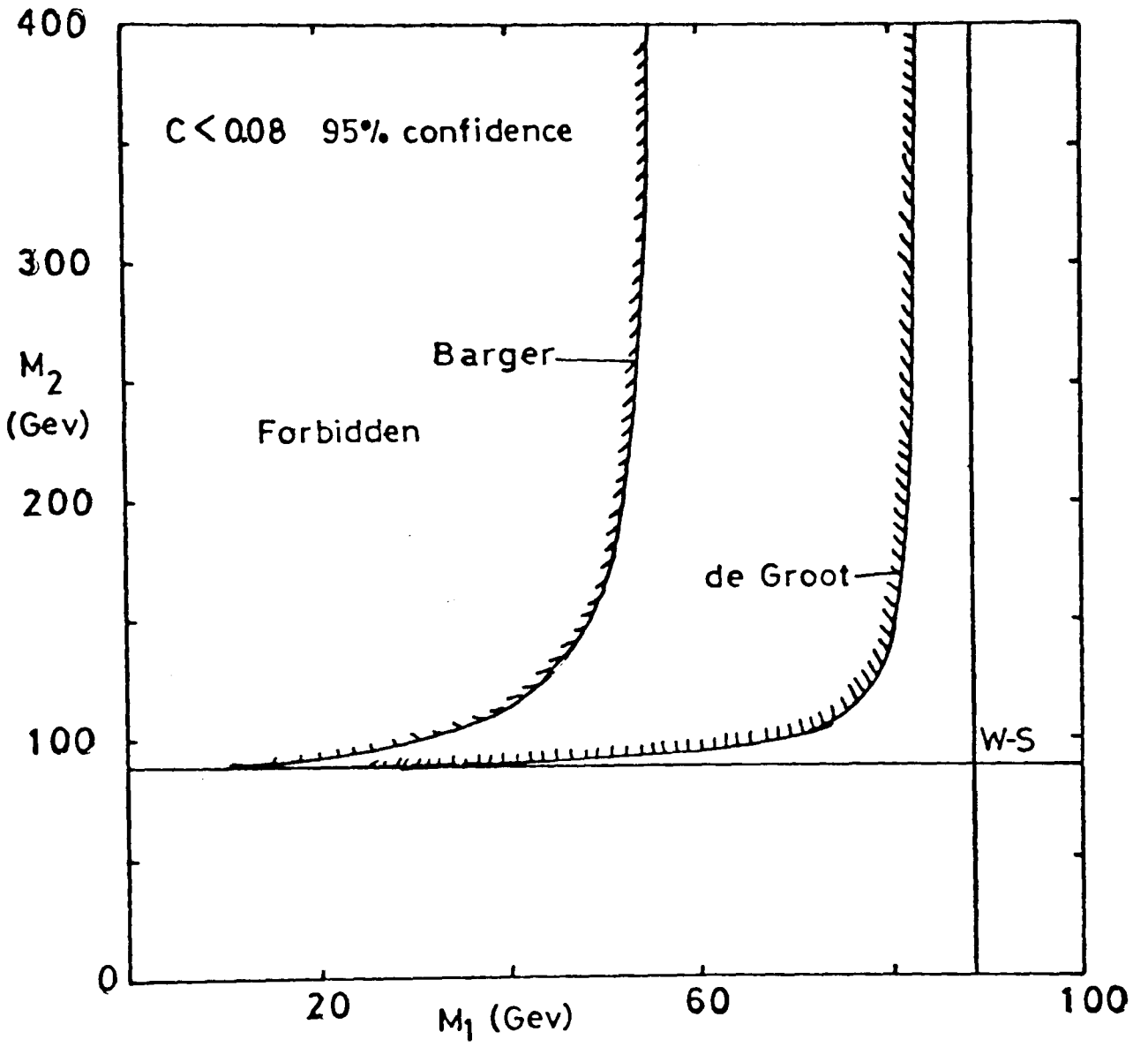

Figure 5.16 Limits on the masses of bosons in alternative electroweak theories.

5.13 Recent TASSO results on the Bhabha cross section

Since 1980 TASSO has collected much more data and has made a new determination of the Bhabha cross section. Much larger data samples have been possible because of the installation of mini-beta quadrapole magnets which focus the beams more strongly at the intersection region. This has caused a 5 fold increase in the luminosity routinely acheived.

The data samples at mean beam energies of 7, 11, and 17 Gev now comprise 10662, 7126, and 49908 events respectively. The experimental selection procedures are similar to those of the analysis described in this Chapter but the experimental conditions were slightly different. During 1981 and 1982 no synchrotron radiation shield was present. The measured trigger and reconstruction efficiencies were higher and more stable. This was greatly helped by the high data rates which allowed more frequent and accurate efficiency determinations to be made. The new quadropole magnets made it necessary to install a less sophisticated luminosity monitor.

Reference (59) shows that the present Bhabha cross section value agrees, with small statistical errors, well with the zeroth order QED cross section. However the systematic errors have not been radically improved. A value of 3.5% is quoted for the systematic error in determining the Bhabha detection efficiency (trigger, reconstruction..etc) and the error on the Forward Detector luminosity is estimated as 4.5%.

Fits to the latest Bhabha differential angular cross section give Λ values of the order of 200 Gev. The values of the parameters of the electroweak theory of Glashow-Weinberg-Salam have been significantly improved by combining the Bhabha data with muon pair results. The number of muon pairs detected has increased from approximately 150 in the pre 1980 data to 2411 in the data collected up to the end of 1982. This is partially a result of an increased muon pair acceptance as a result of using Liquid Argon counter data to identify muons. The latest values of

the electroweak parameters are

$$\sin^2(\theta_w) = 0.27 \pm 0.065 \quad \text{(World average = 0.229 ± 0.01)}$$

$$g_v^2 = -0.04 \pm 0.06 \quad \text{(predicted value = 0.0016)}$$

$$g_a^2 = 0.35 \pm 0.09 \quad \text{(predicted value = 0.25)}$$

The parameter C, which measures the contribution of extra gauge bosons is now constrained to be < 0.02.

Comaparable results are available from studies of Bhabha scattering by other PETRA groups and by experiments at the new PEP storage ring at SLAC[60].

CHAPTER 6

Analysis of the $e^+ e^- \to e^+ e^- \gamma$ final state

6.1 Introduction

This chapter presents a determination of the cross section for the process

$$e^+ e^- \to e^+ e^- \gamma$$

in which the photon is energetic and isolated from the charged electrons. The process is detected by looking for two charged tracks in the TASSO central Drift Chamber and a high energy photon in the Hadron Arm electromagnetic shower counters, HASC. Identification of the charged tracks as electrons was not required as the acceptance for all particles to enter shower detectors was small. The results of using the Liquid Argon shower counters for this analysis are not presented as their operation for the data period of interest was not reliably understood.

The two possible processes considered for the production of an $e^+ e^- \gamma$ final state are:

a) radiative corrections to Bhabha scattering.

These processes are expected to account for a few percent of the total Bhabha cross section. The effects of bremsstrahlung can be seen in the acollinearity distribution of Bhabha events, see Figure 5.5. The effects of bremsstrahlung have been calculated using the Bhabha Monte

Carlo generator which was introduced in Chapter 5.

b) <u>The production and decay of an excited electron state, e^*</u>

This reaction procedes via

$$e^+ e^- \rightarrow e^* e$$

followed by

$$e^* \rightarrow e + \gamma$$

The e^* can be produced with either sign of electric charge. The cross sections for the production and decay processes are calculable using standard techniques of QED with a magnetic coupling term. Two parameters are introduced into the cross section formula, the mass of the e^* state and its coupling strength, λ, to other charged particles. The coupling strength of the normal electron is 1 and this is the simplest assumption for the e^*. If the coupling strength of the e^* is very small then it will have no observable effects even if it has a small mass. The e^* production cross section is given in Chapter 1 and has been implemented by the author into a Monte Carlo generator which is discussed in Appendix 3. The size of the production cross section for an e^* and its relation to the integrated Bhabha cross section is illustrated in Figure 6.1. Both the Bhabha and the differential e^* cross section formula are integrated over the range $|\cos(\theta)| > 0.87$. The Monte Carlo generator produces both positive and negative e^* states and therefore uses a cross section estimate which is twice that shown in Figure 6.1.

The Monte Carlo generators are used in conjunction with the SIMPLE Monte Carlo detector model to compare with the results of the data analysis.

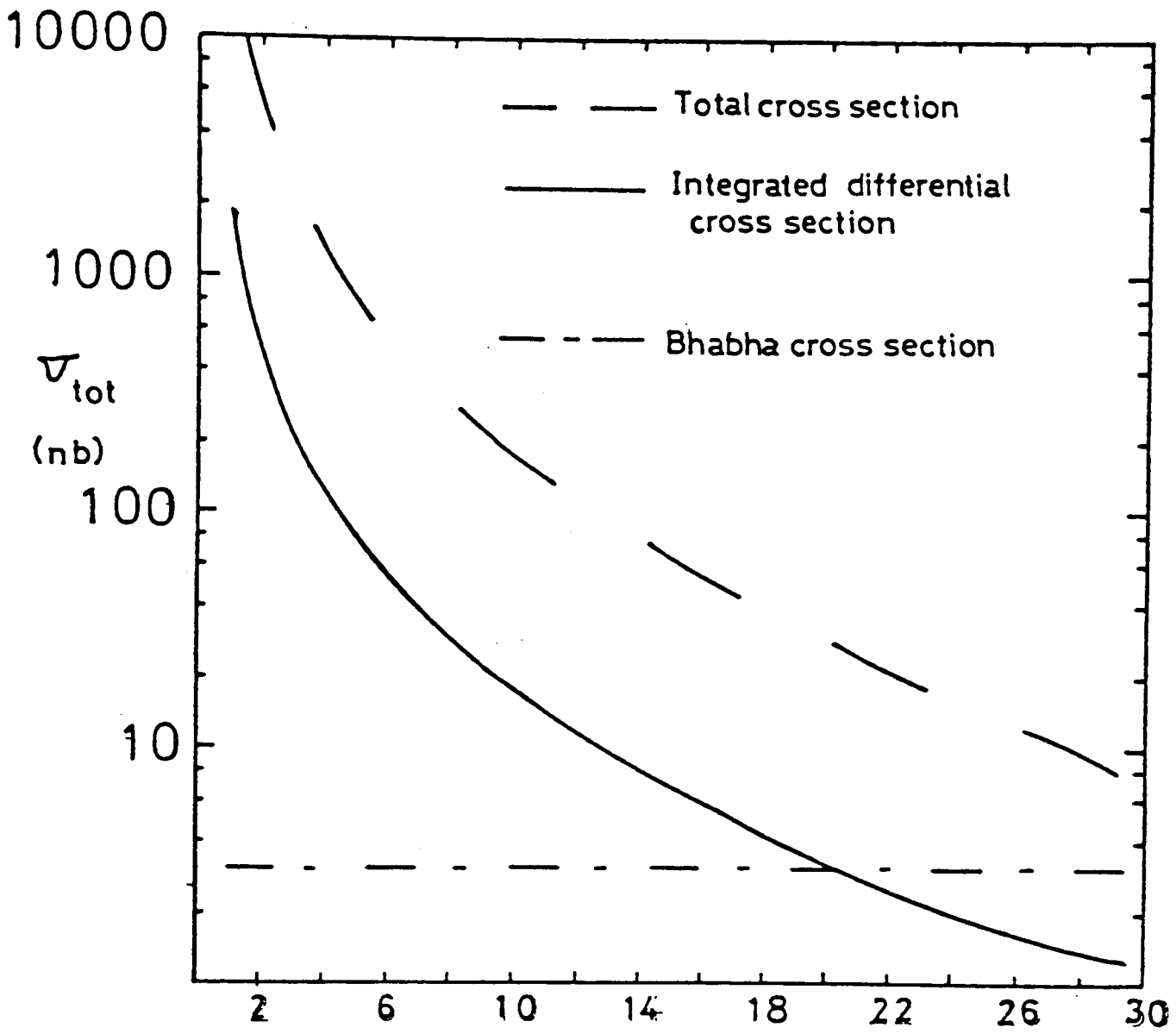

Figure 6.1 Total cross section for excited electron state production as a function of the mass of the state. The solid curve is a numerical integration of the differential cross section formula of Terazawa for a production angle whose cosine value is less than 0.87 in absolute value. The dashed line is the total cross section value formula quoted by Terazawa for all production angles. The dot-dashed line is the total lowest order Bhabha cross section integrated over the same angular range as the solid curve.

6.2 Data Samples

The data sample used for this chapter is the same as that of the previous chapter i.e. the 2 prong datasets. These are datasets of low multiplicity and low acollinearity events selected from triggers which utilised charged particle information only. Details of the exact cuts are to be found in section 4.6.5. The use of events which were triggered by the HASC triggers would have allowed larger acollinearity events to be studied but was not attempted because of the great data reduction effort required and because of uncertainties in the efficiency of the HASC triggers.

6.3 Event Selection

6.3.1 Preliminary Selection

The following cuts were applied to the data from the 2 prong tapes in order to select a sample of e e γ candidates:

1) 2 and only 2 tracks reconstructed in r-θ-ϕ

2) 1 and only 1 electromagnetic shower cluster which satisfied

a) $E_{clust} > 1.0$ Gev where E_{clust} is the energy of the shower cluster. The cluster energy was calculated by adding together the energy of a high energy counter and its 8 closest neighbours. This simple algorithm was adequate as the counter size was large in comparison with the lateral dimension of an electromagnetic shower and because all 3 tracks were required to be isolated from one another. The analysis was insensitive to this clustering procedure.

b) $\theta_{clust} > 20^0$ where θ_{clust} is the smallest angle between the photon cluster and any of the 2 charged tracks.

These cuts resulted from considering the angular extent of the HASC and from Monte Carlo studies of the candidate processes and their interaction with the detector.

These cuts produced a dataset of 89 candidate events which was then visually scanned. The dataset was found to contain background events from the coincidence of cosmic rays passing through the Drift Chamber and a spurious signal in the HASC. Such spurious counter pulses could be caused by the leakage of external light into the counters, spurious electrical pickup signals or incorrect pedestal value subtractions for certain runs.

6.3.2 Kinematic Fitting of events

The final events were selected by passing all the candidate events through a kinematic fitting routine which fitted them to a $e^+ e^- \gamma$ hypothesis and required both energy and momentum conservation. The momentum and energy equations provide 4 constraint equations and as the momenta of all the particles is measured, the number of degrees of freedom of the fit is 4. (number of degrees of freedom = number of constraint equations - number of unknowns)

Two different minimisation routines were tried. The first was a general N-body kinematical fitting routine, KINFIT. This was written by Koch at DESY[61]. The second routine utilised the CERN program library routine, MINUIT[62], as a minimiser. The results from both routines were consistent even on an event by event basis.

The errors assigned to the measured quantities for the purposes of the fit were:

Drift Chamber tracks

$$\frac{dp_t}{p_t} = 0.02\ p_t$$

$$d\theta = 5 \text{ mrad} \qquad \text{and} \qquad d\phi = 2 \text{ mrad}$$

HASC

$$\frac{dE}{E} = 0.20 \qquad \text{for} \qquad E > 4 \text{ Gev}$$

$$\frac{dE}{E} = \frac{0.40}{\sqrt{E}} \qquad \text{for} \qquad E < 4 \text{ Gev}$$

$$d\theta = 0.1 \text{ rad} \qquad \text{and} \qquad d\phi = 0.1 \text{ rad}$$

The resolution of the HASC for low energy electromagnetic showers was determined from Monte Carlo simulations using the EGS shower development program.

Events were accepted as good e e γ events if the probability derived from the χ^2 of their measured and fitted parameters was greater than 5%. Because the energy resolution of the apparatus was a strong function of the particle momenta the errors used in the calculation of the χ^2 of the fit were those appropriate to the fitted values of the particle momenta. 21 events were selected from the sample of 89 candidates. These 21 events were visually checked to eliminate events which might have been due to spurious signals. Events in adjacent time periods were checked to determine that the shower counter under study was not giving anomolously high or frequent signals. All 21 events passed these checks. Figures 6.2 and 6.3 show two of the events which were finally selected. (The isolated photon in Figure 6.3 is the energy of the rightmost cluster in the lower HASC of the Central Detector)

6.4 Monte Carlo simulation of acceptances

Event generators and the SIMPLE detector simulation were used to estimate the acceptance of the TASSO detector for $e^+ e^- \gamma$ events. Real data was used to determine the efficiencies used in the SIMPLE simulation. The simulation was done on a run by run basis. The expected number of

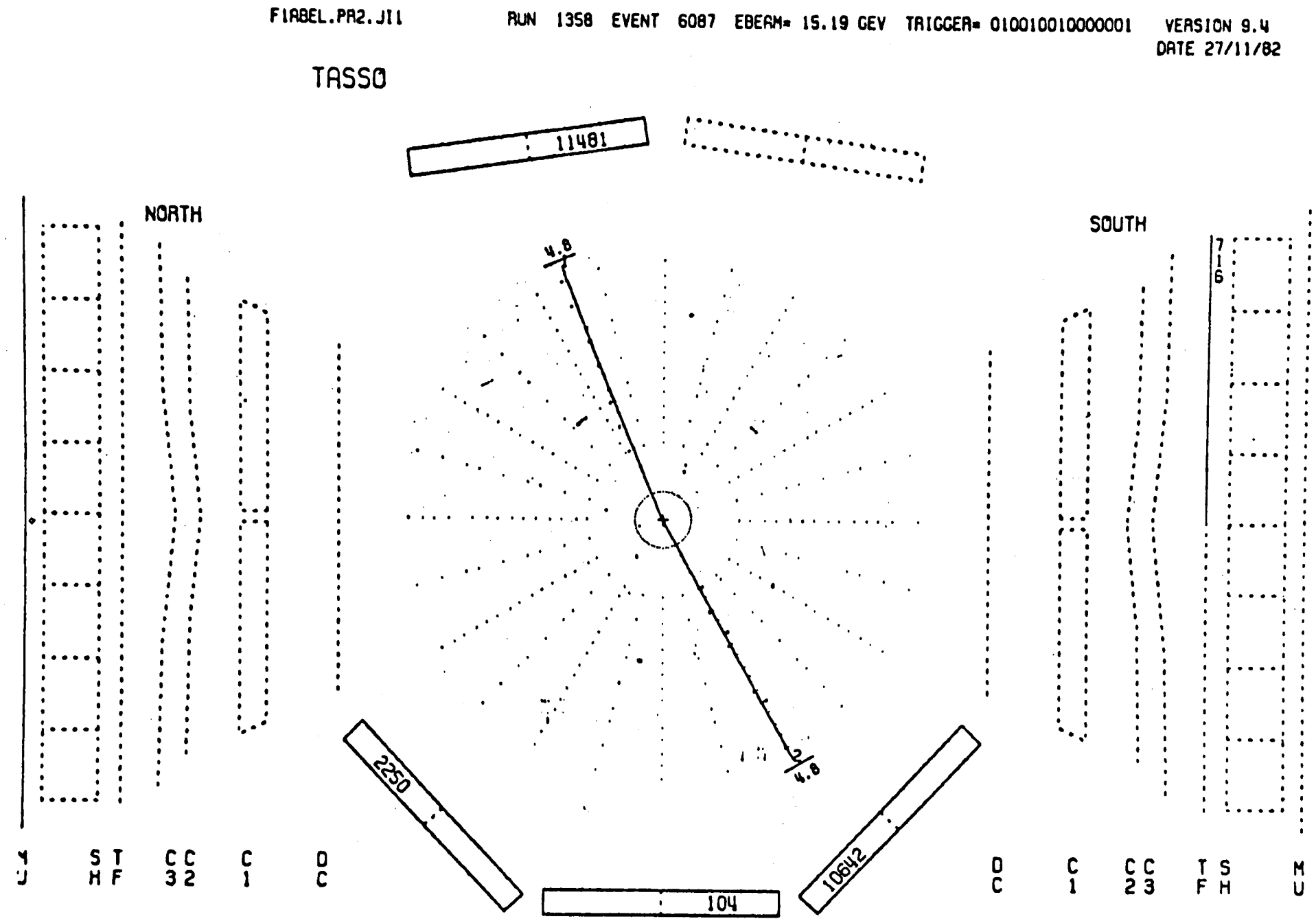

Figure 6.2 An eeγ event from the 1979 data.

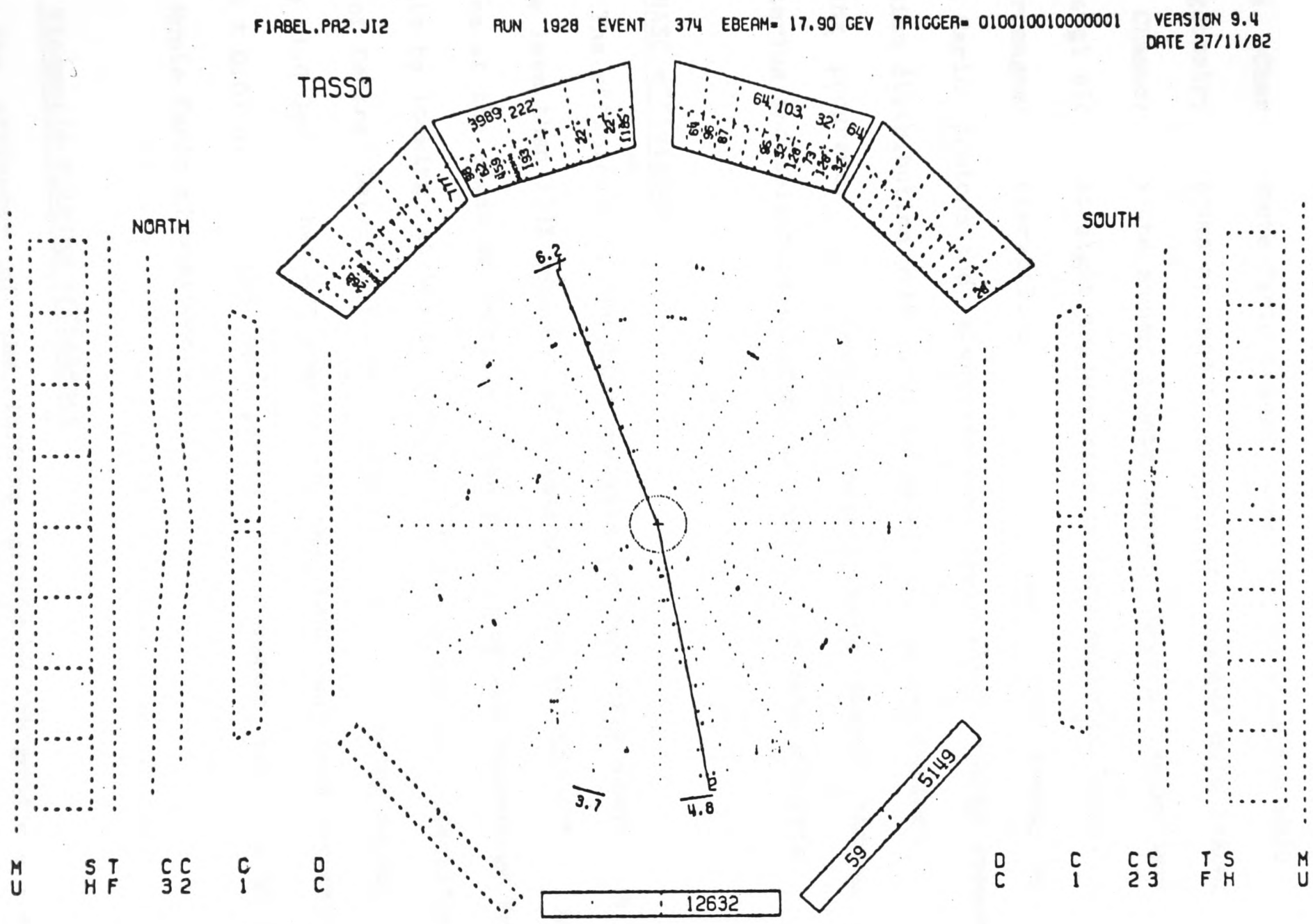

Figure 6.3 An eeγ event from the 1980 data.

data events for each data run was calculated from the beam energy, the luminosity of the run and the cross section of the process. The number of Monte Carlo events generated corresponded to about 10 times the luminosity content of the data sample. The statistical error of the predicted numbers is therefore of the order of 3 times less than the real data sample. Charged Monte Carlo tracks were tracked into the HASC using the same geometry programs as used to extrapolate charged data tracks from the Drift Chamber into the shower counter array. Neutral tracks were allowed to travel along straight trajectories in the magnetic field, undergoing electromagnetic interactions along their path. The energy deposited by Monte Carlo photons and electrons was their total energy smeared by a Gaussian distribution with a width equal to the resolutions used in the fitting programs. The modelled events were passed through the same clustering and selection programs as used in the data analysis.

6.5 HASC efficiency

The efficiency of the HASC analysis for real data events was expected to be less than 100% because of tracking errors and the effect of energy losses at the edges of counters. The efficiency was determined from data events by looking at the proportion of Bhabha events, identified by the use of Central Detector information, which had an energy deposit greater than 1.0 Gev. The efficiency of the HASC was thus determined to be 0.85 ± 0.01 over all the data period. This number was used as input to the Monte Carlo simulations.

6.6 Kinematic Fitting efficiency

The efficency of the fitting procedure on good e e γ events was determined by fitting Monte Carlo events which passed all other selection criteria. The fitting program found all e e γ events from the event generators but after passing these same events through the SIMPLE detector simulation the efficiency was found to be only 0.48 ± 0.05. The principal

cause of this low efficiency was the effect of particles electromagnetically showering in the material of the inner detector. It is shown in Chapter 5 that the measured momenta of high energy Bhabha electrons is on the average as much as 15% less than the beam energy. The fitting efficiency for fitting $\mu^+\mu^-\gamma$ events which do not undergo electromagnetic showering, was 100%. A further check was to repeat the Monte Carlo simulation without the routines which simulated pair conversion and bremsstrahlung. The fitting efficiency for these eeγ events was near 100%. The parameterisations of electromagnetic interactions are based on the formulae presented in Appendix 2 and were expected to be accurate for electrons and photons of energies greater than a few hundred Mev. Some confidence in their reasonableness can be gained by noting that in the study of Bhahba scattering it was found that the SIMPLE Monte Carlo yielded similar efficiency results and similar data distributions as the more sophisticated EGS Monte Carlo simulation of electromagnetic interactions. The SIMPLE Monte Carlo has also been independently used by S. Yarker for the study of the reaction ee $\rightarrow \gamma\gamma$ where both γ are real. He has found the simulation reproduces well the features of this reaction (energy distributions, particle multiplicity etc).

6.7 Results of the QED Monte Carlo

For the estimation of the number of events from the Bhabha process the parameters of the Bhabha generator were chosen to generate all photons with energies between 0.01 and 0.95 of the beam energy. The photon spectrum above the upper limit is not well understood by theory and although it is large it does not contribute a large number of events to the seen cross section as most events with such a high energy photon contain a charged particle which is close to the beam axis and therefore undetected. The expected number of radiating Bhabha events was determined to be 17.7 $\pm$1.3 $\pm$ 2 events for a luminosity of 7088 nb^{-1}. The first error

is statistical and the second is a systematic error estimate. The systematic error reflects the approximate 10% uncertainty in the treatment of interactions and their subsequent influence on the fitting procedure used to identify the eeγ events.

6.8 Background sources

6.8.1 Physics Sources

Several physics processes could produce a contribution to the 2 charged track and 1 isolated photon signature. The possibilities considered were radiative muon or tau pair production, hadronic tau pair decays which produce neutral pions, and 2 photon processes. Monte Carlo simulation showed that only the radiative muon pair process produced a significant signal. The cross section for the radiative muon pair process is always much less than that of the radiative Bhabha process but the efficiency for detecting $\mu\mu\gamma$ events is higher because they suffer few detector interactions. A Monte Carlo study indicated that we should see 3.6 ± 0.4 events from this source. The error reflects an approximate 10% systematic uncertainty in the calculation.

6.8.2 Random fits

The effect of passing random events through the fitting program was studied to determine how many events might be random associations of tracks (i.e. cosmic rays) rather than true physics events. The random events were produced by taking the candidate events after the initial cuts and replacing the photon in the current event by the photon seen in a previous event. The events were then passed through the same selection cuts and if they survived they were processed by the fitting programs. Both Monte Carlo and real data events were processed by this method and both sets of data gave a 4 ± 1% probability for fitting an event which passed the initial selection cuts. Thus from 89 candidate events we expect 3.5 ± 0.9 events to be pure random associations.

6.9 Conclusions of comparison with QED

The data contains 21±4.6 events which pass the selection procedure for e e γ events. Monte Carlo and data calculations indicate that we expect to see 25±2.6 (errors summed in quadrature) events from standard QED sources or random artifacts of the selection procedure. These numbers are in good agreement. Figure 6.4 shows the energy spectrum of the photons in the 21 selected events. Figure 6.5 shows the invariant mass spectrum of the 2 possible charged track and 1 photon combinations for the same events. Both Figures contain the prediction of the QED Monte Carlo (absolute normalisation) for the eeγ process. The distributions are in very good agreement although the meagre statistics precludes any detailed comparison.

6.10 e^* Prediction

The agreement of the QED predictions and the observed number of eeγ events means that the contribution of events from an excited electron state must be small. Figure 6.6 shows the number of events expected from single e^* production and decay as a function of the e^* mass (assuming that the coupling $\lambda = 1$). These numbers were derived using the e^* event generator and the same procedures as for the QED predictions of the previous section. The experimental acceptance, at a fixed value of the beam energy, was found to be fairly constant for e^* masses above 20 Gev. The acceptance finally began to drop sharply as the e^* mass approached the beam energy and the momentum of one of the tracks was always small. Events then failed to have 2 tracks reconstructed in 3 dimensions. The curve of the expected number of events has a pronounced drop at 30 Gev because a large portion of the data was taken with a beam energy of 15 Gev and e^* particles with a mass of greater than twice the beam energy cannot be produced in these lower energy runs.

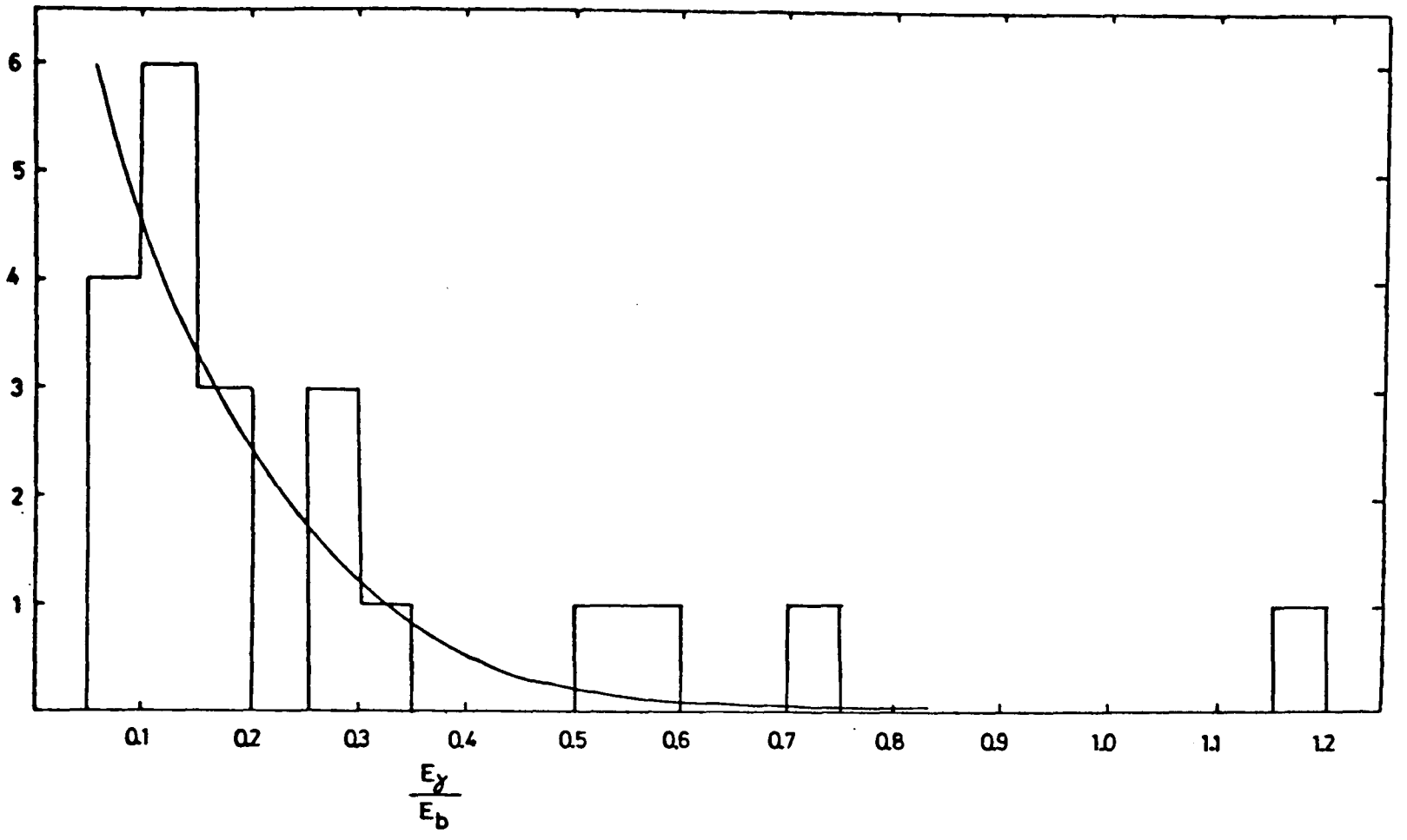

Figure 6.4 Energy of photon in final eeγ events. (The curve is a QED Bhabha Monte Carlo result)

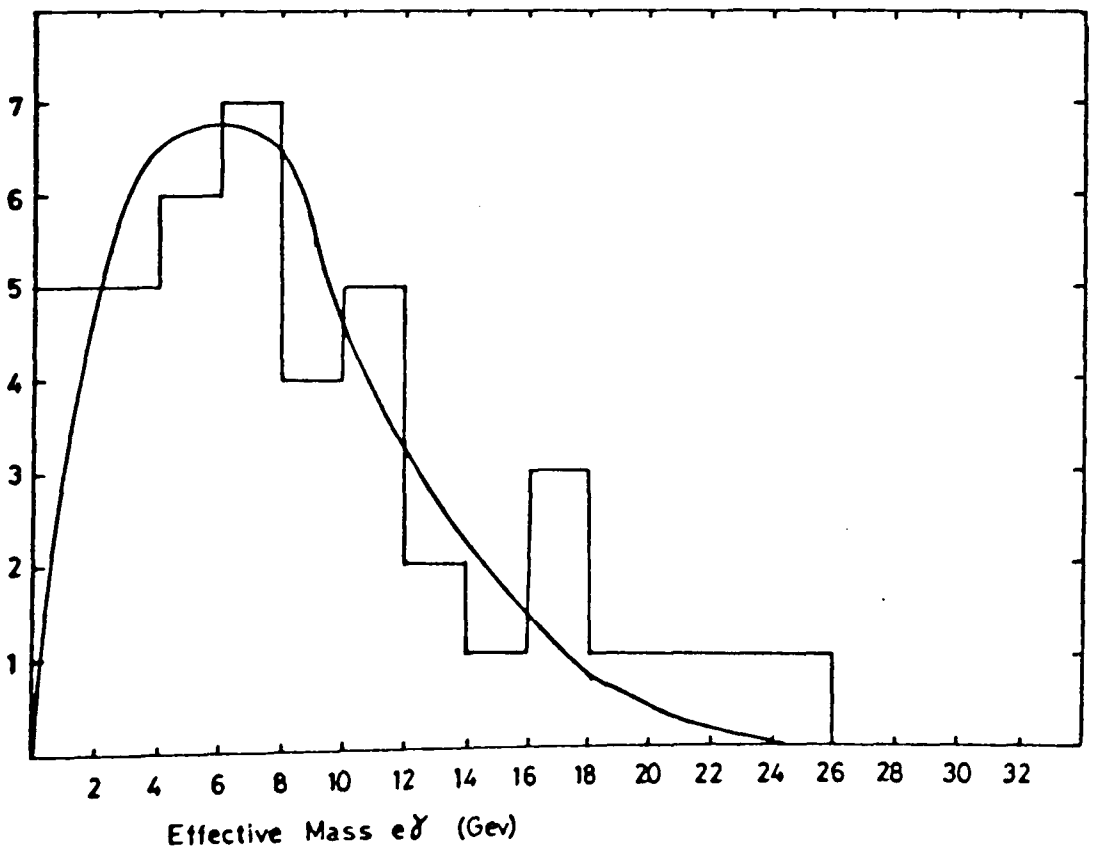

Figure 6.5 Invariant mass distribution of the photon and a charged track for final eeγ sample. (Curve is Bhabha QED result)

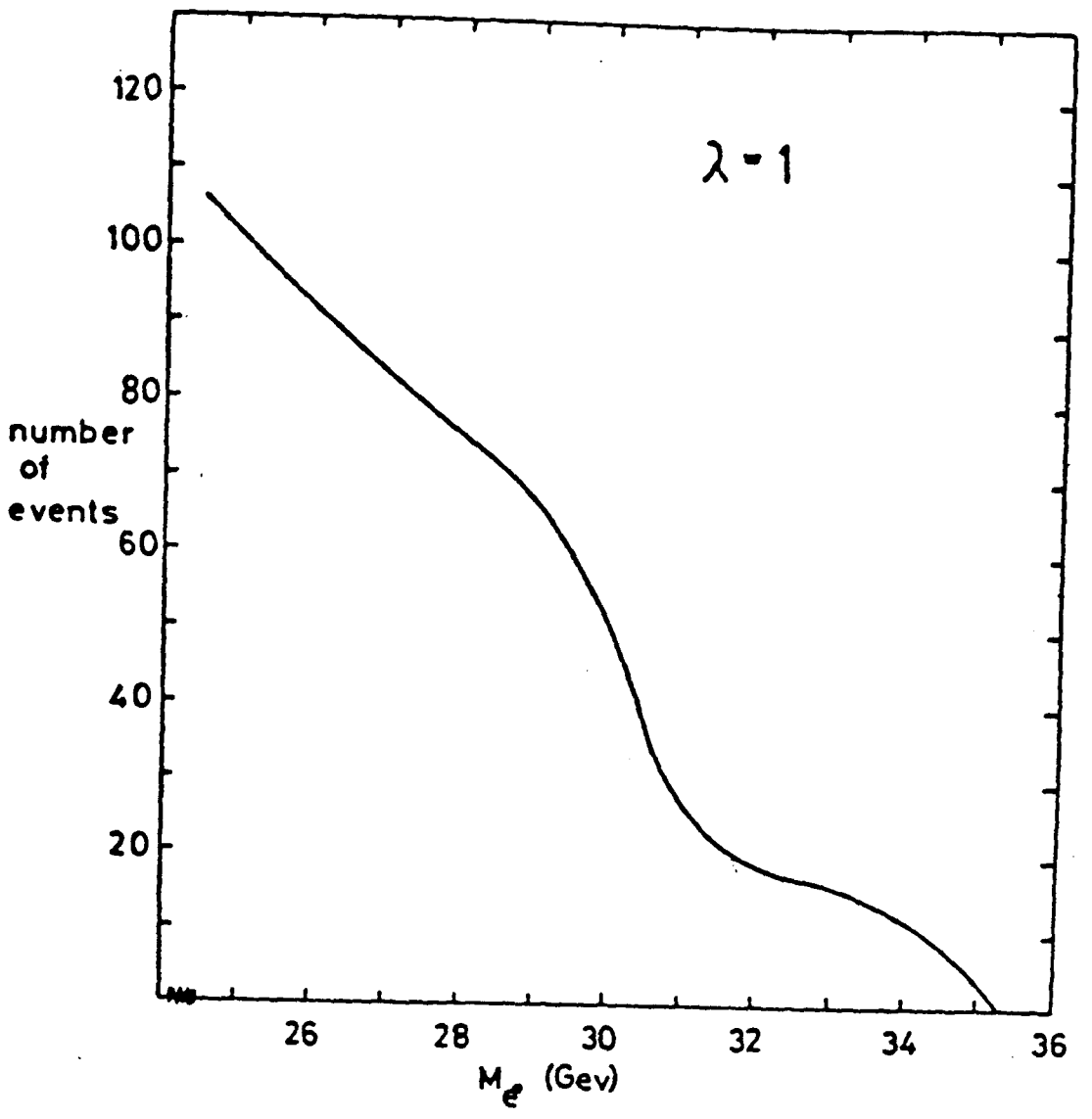

Figure 6.6 Number of eeγ events expected from an excited electron state as a function of the mass of the state, for the data period of this thesis.

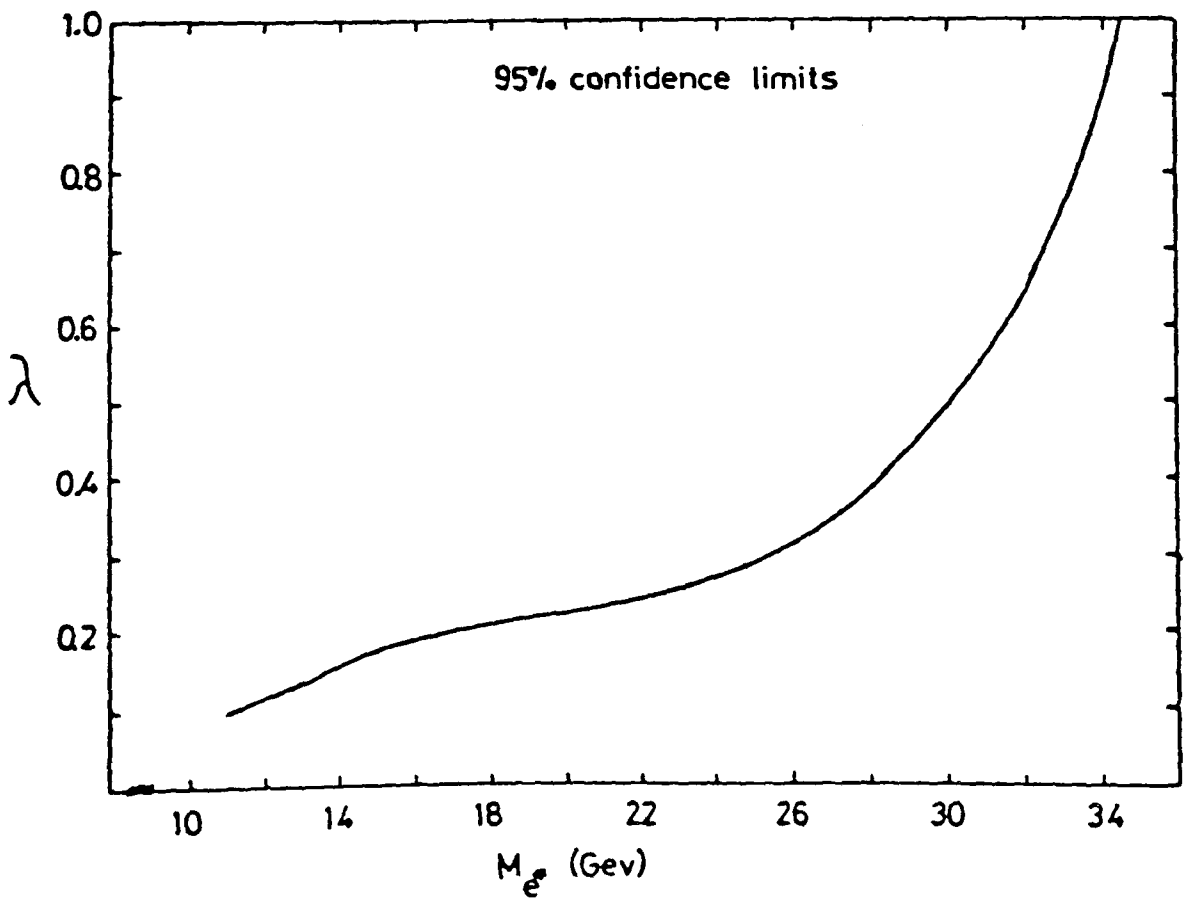

Figure 6.7 Variation of mass limit of an excited electron state as a function of the states coupling strength, λ.

A numerical limit was placed on the mass of a possible e^* by using the Normal test statistic, Δ, defined by

$$\Delta = \frac{N_d - N_p}{\sqrt{(Var(N_d - N_p))}}$$

where N_d is the number of eeγ events found in the data and N_p is the number of events predicted. N_p is the sum of events from standard QED sources, N_{QED}(= 25), and the number of events predicted from e^* events, N_e. $Var(N_d-N_p)$ is the variance of the difference of predicted and seen event numbers. It is the sum of the variances of the individual terms, $Var(N_d)=N_d$ and $Var(N_{QED})=2.6^2$. Assuming only statistical errors for the e^* prediction ($Var(N_e)=N_e$), we can derive the value of N_e for which $\Delta = 2$ i.e. a two standard deviation or 95% confidence level deviation between the observed and expected event numbers. This yields a value of $N_e = 7.9$ events. Comparing this with Figure 6.6 leads to the conclusion that any e^* state must have a mass in excess of 34.0 Gev (95% confidence level and $\lambda = 1$).

The photon energy spectrum of eeγ events can be used to reinforce this conclusion. For high e^* masses all the eeγ events from e^* production contain a photon with energy above the beam energy. From the data distribution we can see that only 1 event has an energy greater than the beam energy and that the QED Monte Carlo predicts 0 events with this high an energy. The number of randomly fitted events is also 0 in this kinematic region. Therefore using the same formalism as above the number N_e is calculated to be approximately 6.5 events. This corresponds to a mass limit of greater than 34.5 Gev for the e^* mass.

Figure 6.7 illustrates how the 95% confidence limit on the mass of an e^* particle varies if we assume values of λ different from the normal QED coupling constant value of 1.

Yarker[63] has recently used TASSO data collected during 1980 to place a limit on an e^* mass by fitting the angular cross section for $e^+ e \pm \gamma\gamma$ with both photons being real. From a data sample of 105 identified events he places the mass of an excited electron state with coupling $\lambda = 1$ as in excess of 44 Gev.

APPENDIX 1.

Members of the TASSO Collaboration during 1980

R. Brandelik, W. Braunschweig, K. Gather, V. Kadansky, F.J. Kirschfink, K. Lübelsmeyer, H.-U. Martyn, G. Peise, J. Rimkus, H.G. Sander, D. Schmitz, A. Schultz von Dratzig, D. Trines, W. Wallraff,

I. Physikalisches Institut der RWTH Aachen, Germany[§]

H. Boerner, H.M. Fischer, H. Hartmann, E. Hilger, W. Hillen, G. Knop, L. Koepke, H. Kolanoski, P. Leu, B. Löhr[†], R. Wedemeyer, N. Wermes, M. Wollstadt,

Physikalisches Institut der Universität Bonn, Germany[§]

H. Burkhardt, D.G. Cassel[*], D. Heyland, H. Hultschig, P. Joos, W. Koch, P. Koehler[**], U. Kötz, H. Kowalski, A. Ladage, D. Lüke, H.L. Lynch, P. Mättig, G. Mikenberg[***], D. Notz, J. Pyrlik, R. Riethmüller, M. Schliwa[††], P. Söding, B.H. Wiik, G. Wolf,

Deutsches Elektronen-Synchrotron DESY, Hamburg, Germany

R. Fohrmann, M. Holder, G. Poelz, O. Römer, R. Rüsch, P. Schmüser,

II. Institut für Experimentalphysik der Universität Hamburg, Germany[§]

I. Al-Agil, D.M. Binnie, P.J. Dornan , N.A. Downie, D.A. Garbutt, W.G. Jones, S.L. Lloyd, D. Pandoulas, J. Sedgbeer, R.A. Stern, S. Yarker, C. Youngman,

Department of Physics, Imperial College,London, England[§§]

R.J. Barlow, I.C. Brock, R.J. Cashmore, R. Devenish, P. Grossmann, J. Illingworth, M. Ogg, B. Roe[****], G.L. Salmon, T.R. Wyatt,

Department of Nuclear Physics, Oxford University, England[§§]

K.W. Bell, B. Foster, J.C. Hart, J. Proudfoot, D.R. Quarrie, D.H. Saxon, P.L. Woodworth,

Rutherford Laboratory, Chilton, England[§§]

E. Duchovni, Y. Eisenberg, U. Karshon, D. Revel, E. Ronat, A. Shapira,

Weizman Institute, Rehovot, Israel[§§§]

T. Barklow, J. Freeman, P. Lecomte, T. Meyer, G. Rudolph, E. Wicklund, Sau Lan Wu, G. Zobernig,

Department of Physics, University of Wisconsin, Madison, Wisconsin, USA[§§§§]

---

* On leave from Cornell University, Ithaca, NY, USA
** On leave from FNAL, Batavia, IL, USA
*** On leave from Weizman Institute, Rehovot, Israel
**** On leave from the University of Michigan, Ann Arbor, MI, USA

† Now at SLAC, Stanford, CA, USA
†† Now at mbp Bremen, Germany

§ Supported by the Deutsches Bundesministerium für Forschung und Technologie
§§ Supported by the UK Science Research Council
§§§ Supported by the Minerva Gesellschaft für die Forschung mbH, München
§§§§ Supported in part by the US Department of Energy contract WY-76-C-02-0881

APPENDIX 2

Interactions of photons and electrons with matter

The material presented here follows closely the treatment of Perkins[64] and is principally intended to illustrate some of the formulae appropriate to the description of the interactions of high energy electrons and photons (energies greater than a few hundred Mev). Tsai[54] or the EGS Manual are recommended for the fuller discussion of effects at lower energies.

Electron interactions

The principal processes responsible for energy loss when electrons traverse a dense medium are ionisation losses due to collisions with atomic electrons and the radiation or bremsstrahlung losses caused by the deceleration of electrons in the electric field of nucleii.

In general the mean rate of ionisation loss, $\frac{dE}{dx}$, of a charged particle is given by the famous Bethe-Bloch formula :

$$\frac{dE}{dx} = \frac{4\pi N_0 z^2 e^4 Z}{mv^2 A} \left(\ln\left(\frac{2mv^2}{I(1-\beta^2)}\right) - \beta^2 \right) \qquad \text{(A2.1)}$$

where m is the electron mass, z and v are the charge and velocity of the particle, $\beta = \frac{v}{c}$, N_0 is Avogadro's number and Z and A are the atomic and mass numbers of the atoms of the target medium. I is the ionisation

potential of the material traversed and has the approximate value of 10Z eV. x is the path length traversed in the medium. Figure A2.1 shows the variation of ionisation loss as a function of the kinetic energy of protons which are incident on beryllium or lead targets. The mass of the incident particle, M, does not enter the formula. The ionisation loss is inversely proportional to mass of the target, A, and therefore the energy losses from Coulomb scattering of electrons off nucleii are generally negligibly small in comparison with that from scattering off atomic electrons. However the Coulomb scattering from nucleii can cause appreciable angles of scattering of the incident particle. The differential cross section for a deflection of angle θ is given, approximately, by the Rutherford scattering formula :

$$\frac{d\sigma(\theta)}{d\Omega} = \frac{1}{4}\left(\frac{Zze^2}{pv}\right)^2 \frac{1}{\sin^4(\theta/2)} \qquad \text{(A2.2)}$$

where p is the momentum of the incident particle. This formula predicts lots of small angle scatters which can eventually combine to produce an appreciable deflection of charged particles.

The bremsstrahlung of electrons in the field of nucleii is described by the Bethe Heitler formula. The cross section per nucleus for an electron of energy E to radiate a photon of energy k is:

$$\frac{d\sigma(E,k)}{dk} = \frac{4Z^2\alpha r_e^2}{k} \ln(183\ Z^{-1/3})\ g(k/E) \qquad \text{(A2.3)}$$

where $r_e = 2.8\times10^{-13}$cm is the classical radius of the electron. The function g describes the screening of the nuclear charge by the atomic electrons. For high energy electrons the screening is complete and a calculation, from the above formula, of the average radiation energy loss in traversing dx gcm^{-2} of a medium yields the result :

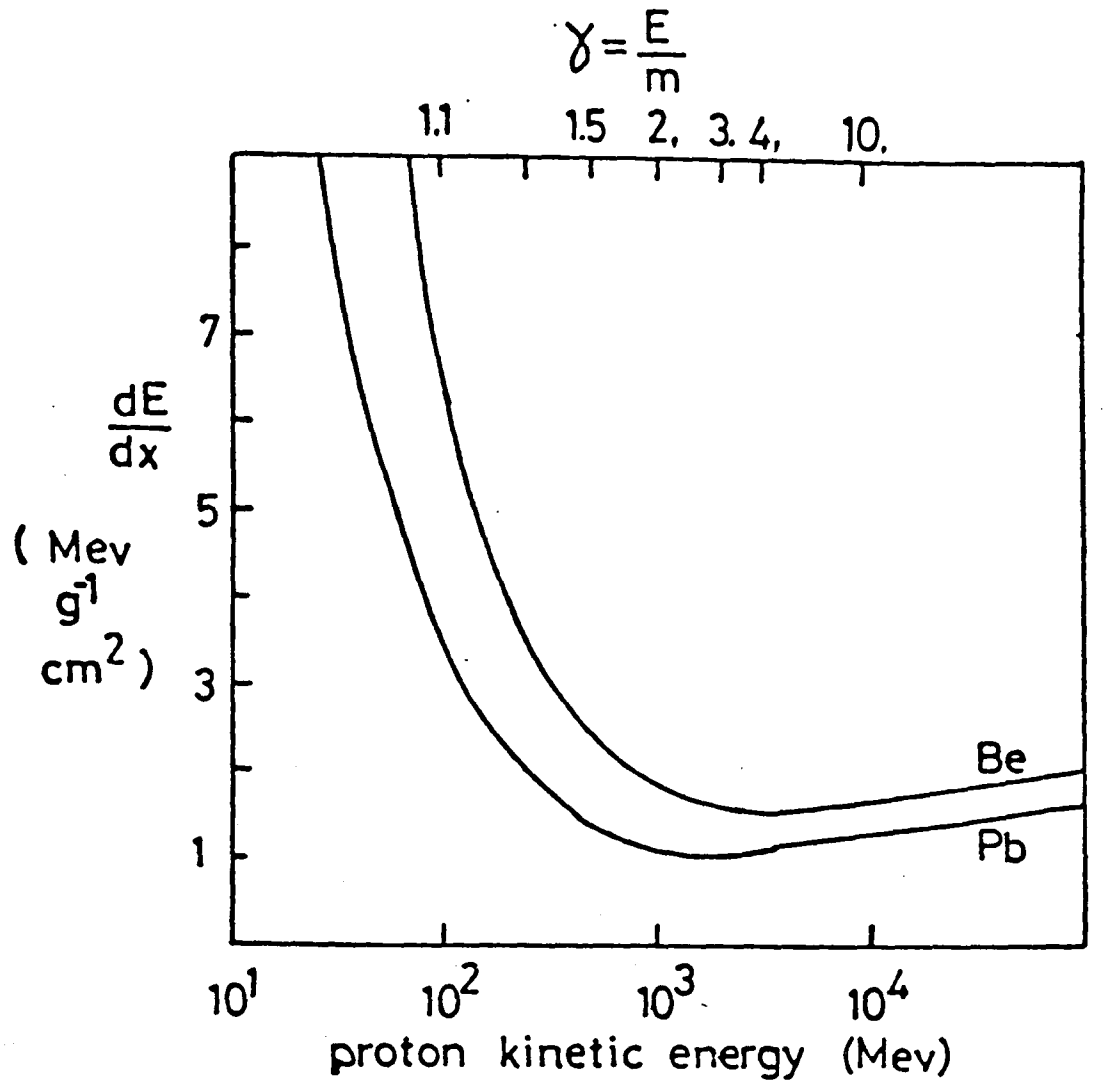

Figure A2.1 Ionisation energy loss for protons on Be or Pb targets.

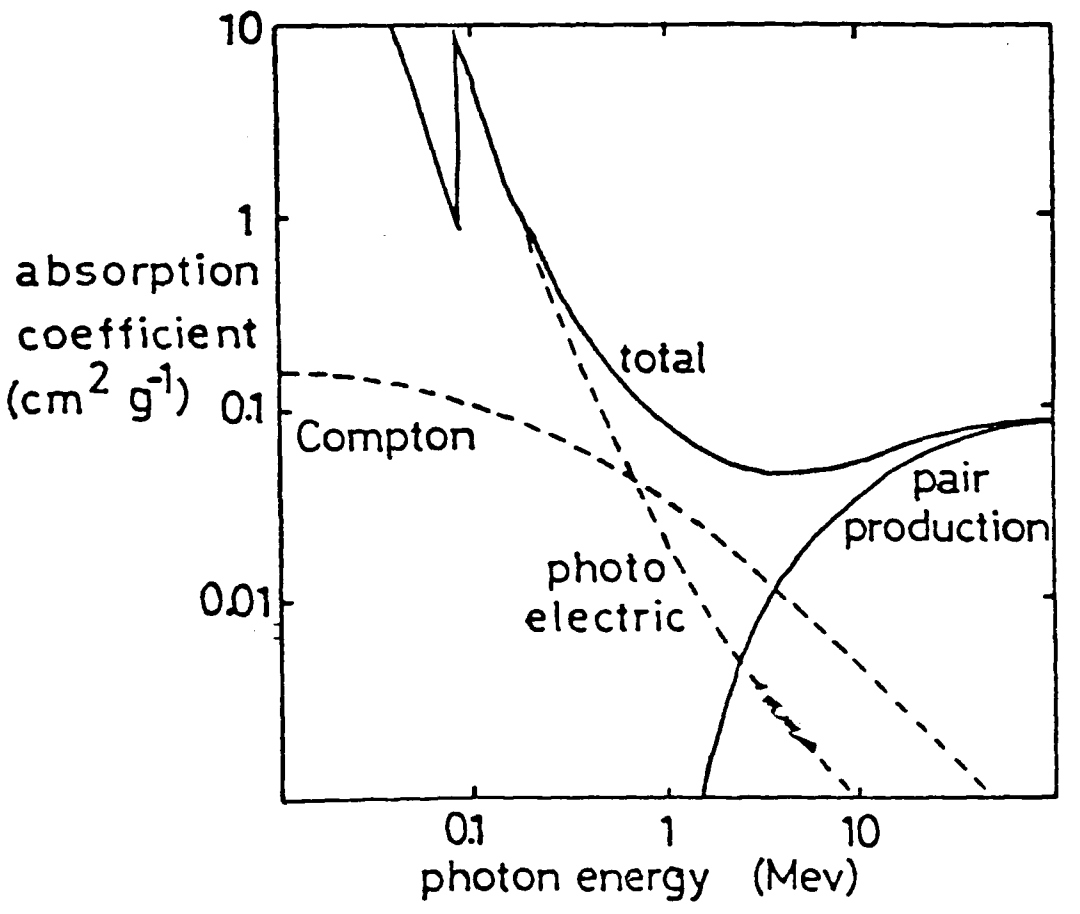

Figure A2.2 Absorption coefficient for photons in a lead target.

$$\frac{1}{E}\frac{dE}{dx} = \frac{4NZ^2 r_e^2}{137A}\left(\ln(183\ Z^{-1/3}) + \frac{1}{18} \right) \qquad (A2.4)$$

where N is the number of nucleii per gram of the medium. If we neglect the final term of the above formula (a contribution of about 1%) then we can obtain,

$$\frac{dE}{E} = -\frac{dx}{X_0} \qquad (A2.5)$$

where $\frac{1}{X_0} = \frac{4N\alpha Z^2 r_e^2}{A}\left(\ln(183\ Z^{-1/3}) \right)$.

For fast electrons the ionisation energy is approximately constant while the radiation losses increase linearly with energy. The critical energy, E_c, at which they are equal is roughly $\frac{600}{Z}$ Mev. A more detailed calculation shows that even for hydrogen E_c is as low as 320 Mev. Therefore in the energy range above a few tens of Mev the mean energy loss of an electron of initial energy E_0 after having traversed a thickness x gcm^{-2} is approximately

$$< E > = E_0 \exp^{-x/X_0} \qquad (A2.6)$$

This can be used to define the radiation length, X_0, of a material.

Photon Interactions

Figure A2.2 shows the relative effects of the photoelectric effect, Compton scattering and pair production of electrons on the attenuation of photons as they pass through matter. The photoelectric cross section varies with photon energy k as $\frac{1}{k^3}$. The Compton cross section falls as $\frac{1}{k}$. For photon energies above 10 Mev the dominant process is pair production which has a cross section which is largely independent of k. Pair

production is closely related to the bremsstrahlung of fast electrons and the cross section for it differs from the bremsstrahlung formula only by kinematic factors. The total probablity of pair production per nucleii can be evaluated as approximately:

$$\sigma_{pair} = 4Z^2\alpha r_e^2\left(\frac{7}{9}\ln(183\ Z^{-1/3}) - \frac{1}{54}\right) \qquad (A2.7)$$

(if Z^2 is changed to Z^2+Z then this, and the bremsstrahlung formula, will approximately account for the field effects of atomic electrons.) The mean free path for pair production is therefore approximately equal to $\frac{7}{9}X_0$, with this asymptotic limit being realised for photon energies of the order of 1 Gev.

APPENDIX 3

A Monte Carlo event generator for an excited electron state

A Monte Carlo generator for the production and subsequent decay of an excited electron state, e^*, was written by the author using the lowest order production cross section formula of Terazawa [20]. This formula was independentally checked by Cashmore, Ogg and Wheater[65]. The calculation of the radiative decay width of an excited lepton state using the same interaction as for the production has been given by Ogg[35] as

$$\Gamma(e^* \rightarrow e\gamma) = \alpha\lambda^2\frac{M}{2}\left(1 - \frac{m^2}{M^2}\right)^3 \qquad (A3.1)$$

where λ is the coupling strength , m is the mass of the lower lepton state and M is the mass of the excited lepton state. For an electron we can set $m = 0$ and this yields a decay width for the radiative decay of 73 Mev for $M = 20$ Gev and $\lambda = 1$. This corresponds to a lifetime estimate of less than 10^{-23} seconds. For higher mass states the lifetime will be shorter.

Consideration of the simple kinematics of the production and decay processes permits most of the feature of the topology of the eeγ final state to be understood. During the production process the e and e^* must emerge in opposite directions with momenta ,p, given by

$$p^2 = E_B^2 - \frac{(M^2 + m^2)}{2} + (\frac{M^2 - m^2}{4E_B})^2 \qquad (A3.2)$$

If the small mass of the e is neglected

$$p = E_B - \frac{M^2}{4E_B} \qquad (A3.3)$$

The energies of the products of the e^* decay can be shown to be

$$E_\gamma = \frac{M}{2}(1 - \frac{m^2}{M^2}) \qquad (A3.4)$$

and

$$E_e = \frac{M}{2}(1 + \frac{m^2}{M^2}) \qquad (A3.5)$$

For high mass excited states both decay products carry off energy and momentum equal to half the mass of the excited state. The essentially massless products of the decay emerge back to back in the centre of mass frame of the decay but on boosting to the laboratory frame the angle between them assumes a range of values depending on the relation of the angle of decay and the boost direction. It can be shown using Lorentz relativistic equations that, for a given e^* mass and energy, there is a minimum angle between the decay photon and electron. This angle always occurs when the 2 massless products emerge at right angles to the direction of the motion of the centre of mass frame.

It is helpful to consider 2 extreme cases

a/ The e^* mass is small

In this case the e^* and e emerge back to back with energies equal to the beam energy. The products from the isotropic decay of the e^* will have little energy or momentum in the centre of mass frame of the decay and will therfore be strongly boosted along the e^* production direction. The energy in the laboratory frame of the decay photon or electron will have a fairly flat distribution as it will be determined by the decay

angle relative to the direction of the e^* boost.

b)The e^* mass is near the centre of mass energy

In this case the produced stable electron has almost zero energy and the decay of the e^* occurs in a frame which is at rest in the laboratory frame. The photon of the decay will have a well defined energy equal to that of the beam energy. This photon will occur directly opposite to an electron of energy equal to the beam energy. The orientation of the low energy electron from the production process will be random relative to both these particles.

The 2 cases described above are illustrated by the distributions shown in Figures A3.1 to A3.3.

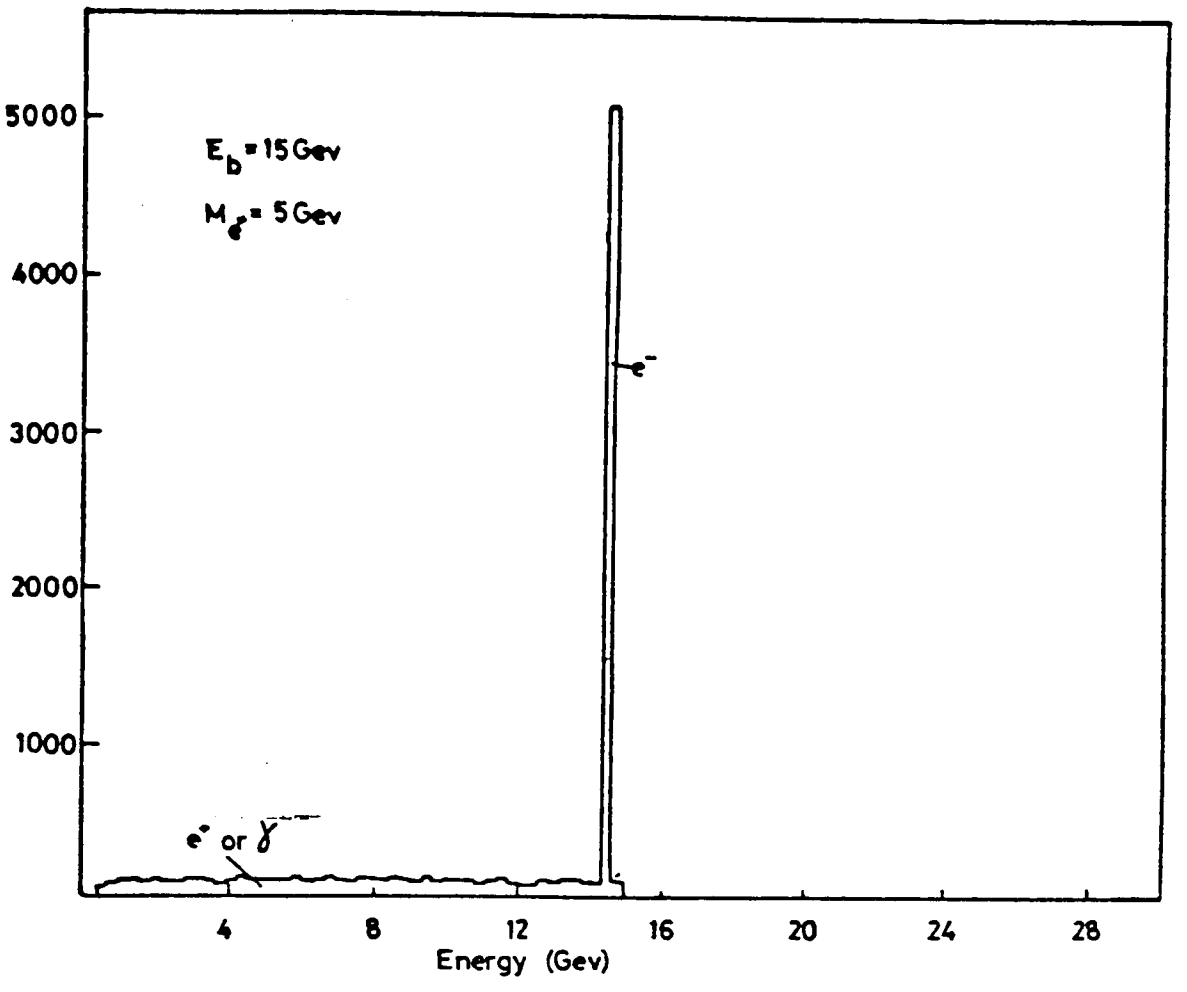

Figure A3.1 Energy of final state particles from excited electron state generator.

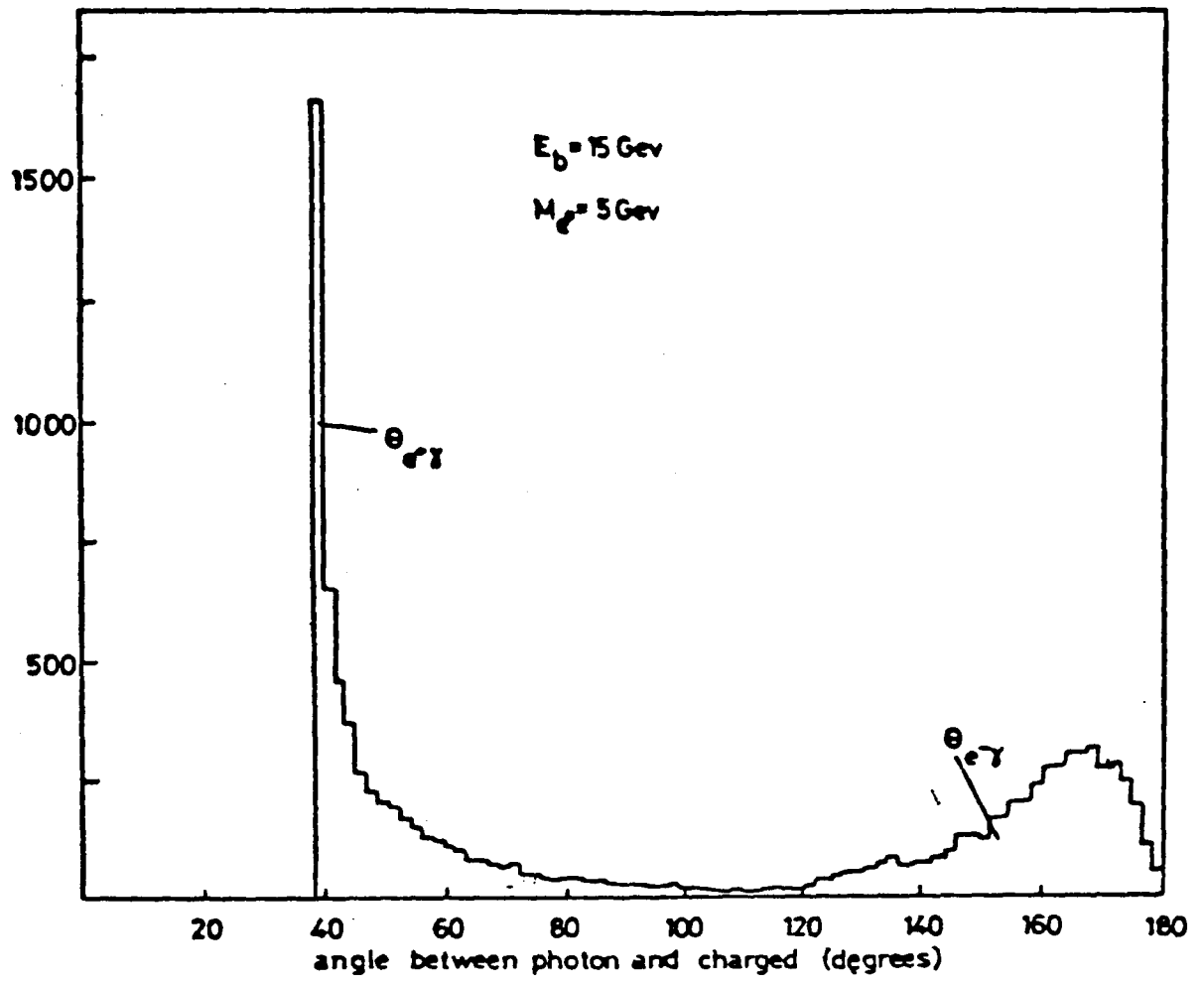

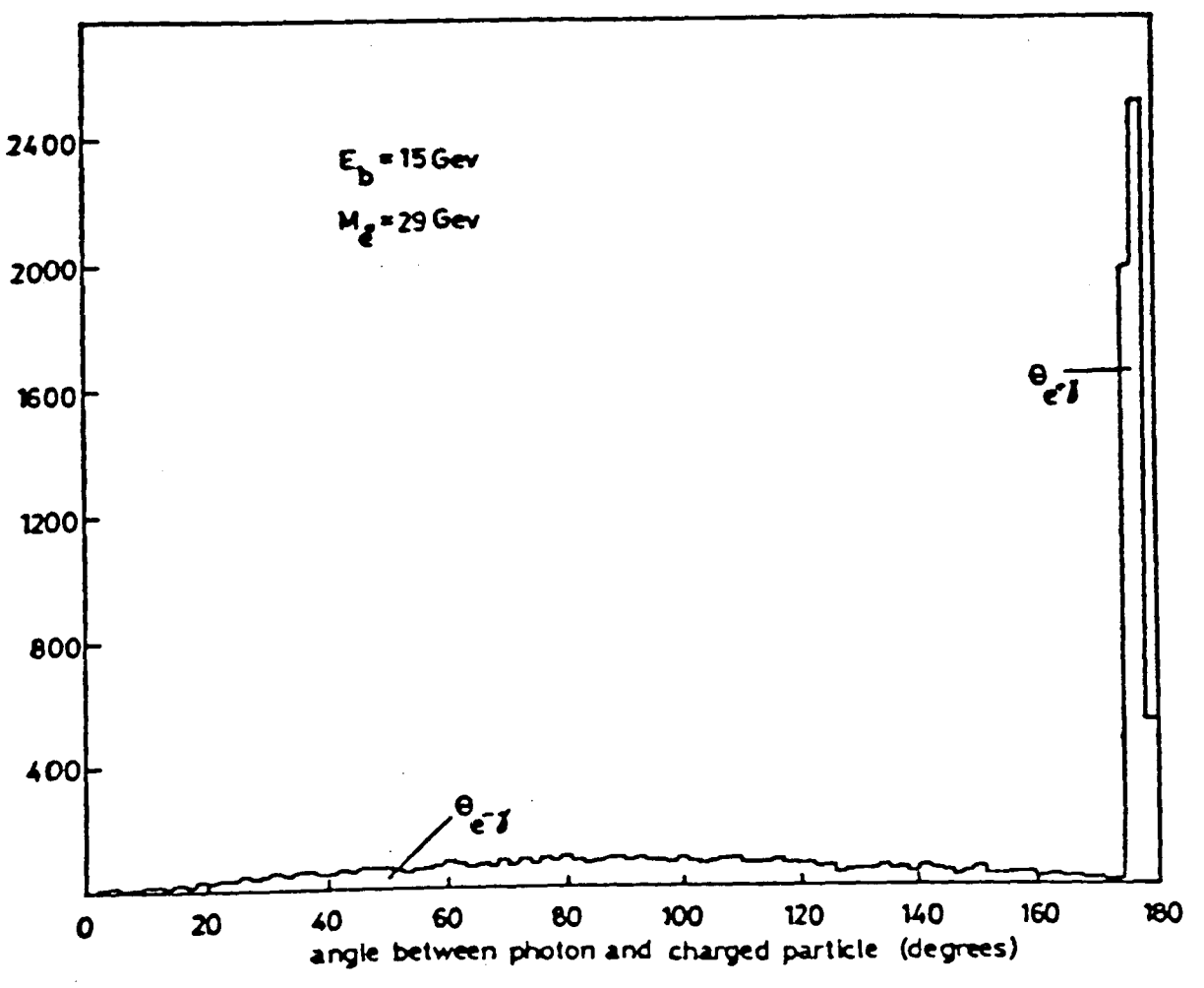

Figure A3.2 Angle between photon and charged particle in excited electron state generator.

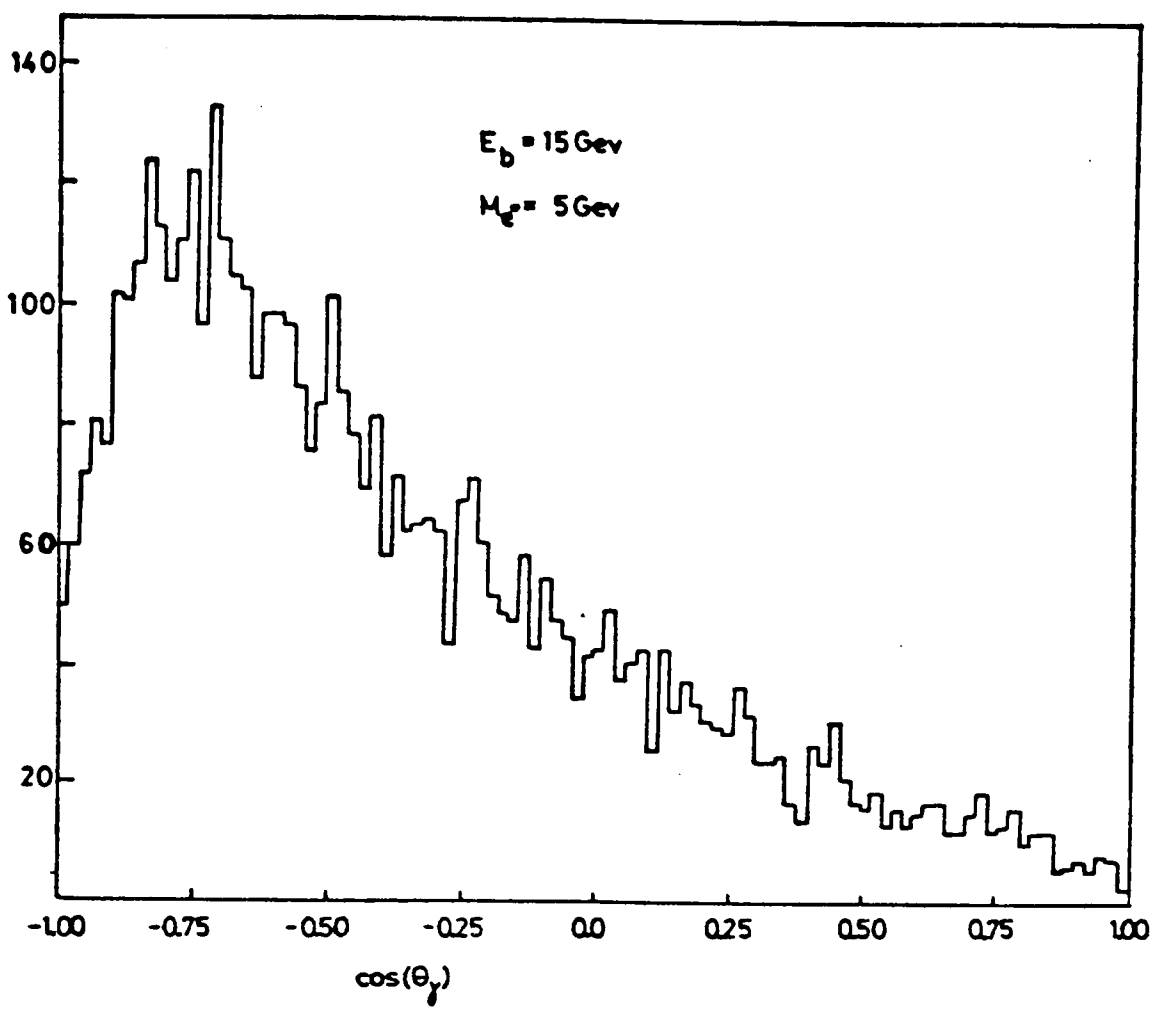

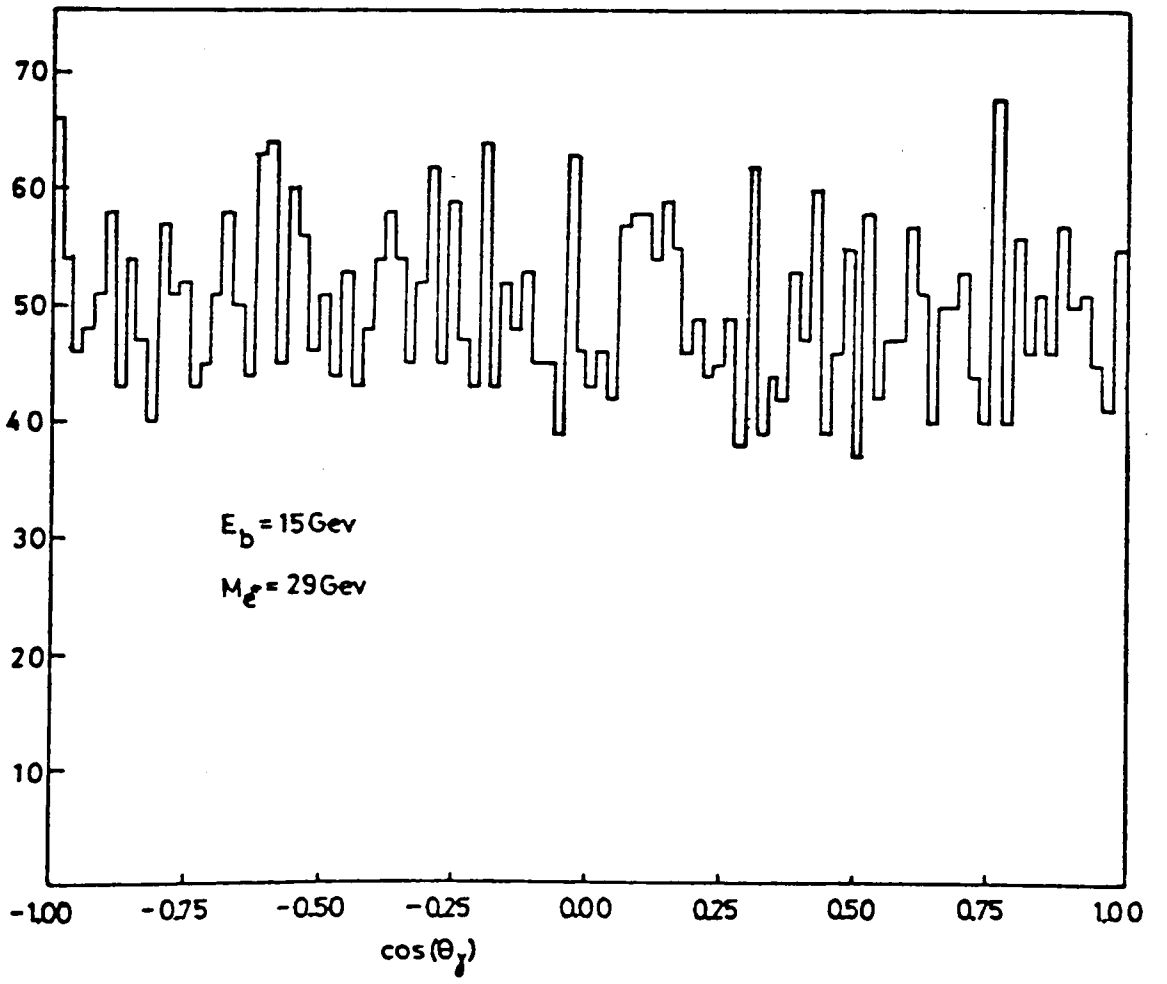

Figure A3.3 Theta angle of final state photon in excited electron state generator.

REFERENCES

(1) Bjorken and Drell, Relativistic Quantum Mechanics,
McGraw-Hill Book Company.

(2) Berends and Gastman, from 'Electromagnetic interactions of Hadrons',
Vol 12 (Edited by Donnachie and Shaw) Plenum 1978

(3) Drell, Ann. Phys.,4 (1958) 75

(4) T.D. Lee and G.C. Wick, Nucl. Phys. B9 (1969) 427

(5) Yanagisawa, UTLICEPP-81-02, April 1981. (Thesis)
T.D. Lee, Topical Conf. on Weak Interactions, CERN 69-7 (1969) 427

(6) R. Marshall, RL-80-029 and Proc. Recontre de Moriand (1980)

(7) S. Weinberg, Phys. Rev. Lett., 19 (1967) 1264
A. Salam in Elementary Particle Theory (N. Svartholm Ed) ,
Almquist and Wiksell, Stockholm, (1968) 367

(8) R. Bundy, Phys. Lett., 45B, (1973) 340
or R. Bundy, Phys. Lett., 55B, (1975) 227

(9) D. Schildknecht, BI-TP 81/12 (Univ. of Bielfeld, West Germany)
or Proc. Inter. School of Subnuclear Physics (Erice, Sicily) (1980)

(10) Kim , Langacker , Levine and Williams, UPR-158T (Univ. of Pennsylvania)
(submitted to Rev. of Modern Physics)

(11) De Groot, Gounaris and Schildknecht, Zeit. fur Phys. C Vol 5 (1980)

(12) Barger et al, Phys. Rev. Lett. 18 (1980) 1165
or Barger et al, Phys. Rev, 22d (1980) 727

(13) Berends, Gaemers and Gastmans, 'Hard photon corrections for photon
scattering', Nucl. Phys. B68 (1974) 541-550

(14) Tsai, 'Copious Production of hard photons in e^+e^- colliding
experiments', SLAC-Pub-2741 (Submitted to Phys. Rev. D)

(15) Swanson, 'Relativistic positron-electron bremsstrahlung at wide angles: a
numerical calculation', Phys. Rev. 154 (1967) 1601

(16) Altarelli et al, Neuvo Cimento 34 (1964) 1337

(17) Berends , Gastmans and Wu, 'Symmetric treatment of ultrarelativistic e^+e^- scattering', KUL-TF-79/022
or 1979 International Symposium on Lepton-Photon Interactions, Aug 23-29,1979, Fermilab
or Gastmans, 'Radiative corrections in gauge theories', KUL-TF-81/4,
or Lectures Karpacz Winter School of Theor. Phys, Feb 1981, Poland

(18) Berends and Kleiss, 'Distributions in the process $e^+e^-\rightarrow\mu^+\mu^-\gamma$', DESY preprint 80/66
and Berends and Kleiss, 'Initial state radiation for e^+e^- annihilation into jets', DESY preprint 80/73

(19) M. Perl, 'Status of Heavy Lepton Searches', SLAC-Pub-2752 (1981)
or Proc. of Physics in Collision Conf., Virginia, May 1981

(20) H. Terazawa et al, Phys. Lett. 112B (1982) 387

(21) Dittman and Hepp, 'Test of Electroweak Theories at PETRA', Desy preprint 81/030

(22) F. M. Renard, Phys. Lett. 116b No 4 (1982) 264

(23) H. Goldberg, Phys. Rev. D 23 (1981) 1991

(24) Kovesi-Domokos and Domokos, Phys. Rev D 24 (1981) 2866

(25) PETRA proposal, DESY, Hamburg (November 1974)
and PETRA proposal (updated version) , DESY, Hamburg (February 1976)

(26) G.A. Voss IEEE Trans. on Nucl. Sci. NS26 (1979) 2970

(27) Wolf, 'Topics in e^+e^- physics', DESY preprint 80/13

(28) TASSO proposal DESY PRC-76/128 (1976)

(29) Fischer and Wermes, BONN-IR-80-22 (1980)

(30) C. Youngman, Ph. D. Thesis, Univ. of London (1980) , RL-HEP/T/82

(31) H. Boerner et al, Nucl. Instrum. Methods 1316 (1980) 151
and H. Boerner, Ph.D. Thesis, Univ. of Bonn (1981) , BONN-IR-81-27

(32) D. Heyland, Ph.D. Thesis, Univ. of Hamburg (1981) ,
and DESY (Internal report) F1-81/01

(33) K.W. Bell et al, Nucl. Instrum. Methods 1733 (13381) 27

(34) Addendum to TASSO proposal, TASSO Internal Note 8 (1977)

(35) M. Ogg, D.Phil. Thesis, Univ. of Oxford (1981) , RL-HEP/T/89

(36) W. Hillen, Ph.D. Thesis, Univ. of Bonn (1981) , BONN-IR-81-7

(37) J.F. Crawford et al, Nucl. Instrum. Methods 127 (1975) 173

(38) E. Hilger, TASSO Internal Note (118)

(39) G. Mickenberg, TASSO Internal note 17

(40) G. Keil, 'Design principles of flouresence radiation converters', Nucl. Instrum. Methods 87 (1970) III-123

(41) B. Barish, 'Large area scintillation counters for hadron calorimetry', IEEE Trans. Nucl. Sci. Vol NS-25 (1978)

(42) Manufactured by Rohm and Haas Gmbh, West Germany.

(43) Manufactured by Polivar Spa, 72 V. Naro, 00040 Pomezia (ROME)

(44) Fujikura Densen Co. Limited, TOKYO, Japan

(45) E.G.G. Type FX 210U

(46) Jade Collaboration - private communication

(47) E.G.S. Code System. Ford and Nelson SLAC-Pub-210 (1978)

(48) Messel and Crawford, 'Electron Photon Shower Distributions for Lead, Copper and Air Absorbers', Pergamon (1970)

(49) T.R. Wyatt, Private communication, TASSO experiment

(50) S. Jarowslavski, Nucl. Instrum. Methods 176 (1980) 263 or N. Downie, Ph.D. Thesis, Univ. of London (1980)

(51) D. Quarrie, RL-81-048 (1981)

(52) BOS Manual, V. Blobel, DESY Computing Centre, Hamburg

(53) D.G. Cassel and H. Kowalski, DESY 80/107 (1980)

(54) Tsai, 'Pair production and bremsstrahlung of charged leptons', Rev Mod Phys., Vol 46,4,(1974)

(55) TASSO collaboration, Phys. Rev. Lett. 100B,(1982) 173

(56) J.A.M. Vermaseren, Talk at International Workshop on $\gamma\gamma$ collisions, (AMIENS) , Lecture Notes in Physics, Vol 134, (Springer 1980)

(57) Meyer, DESY preprint 81-046 (1981)

(58) F. James, 'Interpretation of the errors on parameters as given by MINUIT', CERN Computer Centre Program Library writeup. (D506,D516)

(59) TASSO Collaboration, DESY preprint 82-084 (1982)

(60) Boehm A., DESY preprint 82-084 (Dec 1982)

(61) Koch, DESY Computing Library Writeup.

(62) CERN Computing Library D506.

(63) Yarker S, Ph.D. Thesis, Univ. of London, (1983)

(64) Perkins D, 'Introduction to High Energy Physics', Addison Wesley Publishing Company.

(65) Private Communications.